UNIVERSITY OF CALIFORNIA, SAN DIEGO

Expanding marine biogeochemical observations utilizing ISFET pH sensing technology and autonomous platforms

A dissertation submitted in partial satisfaction of the requirements for the degree
Doctor of Philosophy

in

Oceanography

by

Ellen M. Briggs

Committee in charge:

Todd Martz, Chair
Andrew Dickson
Sarah Gille
Andrew Kummel
Matthew Mazloff
Lynne Talley

2017

The Dissertation of Ellen M. Briggs, is approved, and it is acceptable in quality and form for publication on microfilm and electronically:

Chair

University of California, San Diego

2017

EPIGRAPH

"The ocean holds me in an enduring spell. Part of the spell comes from mystery – the fourfold mystery of the shoreline, the surface, the horizon and the timeless motion of the sea."

-Roger Revelle

TABLE OF CONTENTS

LIST OF FIGURES

LIST OF TABLES

ACKNOWLEDGEMENTS

Over the five years I spent at Scripps Institution of Oceanography I have faced numerous obstacles and challenges in both my professional life and personal. For those that have stood with me and supported me through this journey I am eternally grateful.

Chapter 1, in full, is currently being prepared for submission for publication of the material. Ellen M. Briggs, Sergio Sandoval, Ahmet Erten, Yuichiro Takeshita, Andrew C. Kummel, Todd R. Martz. The dissertation author was the primary investigator and author of this material.

Chapter 3, in full, is currently being prepared for submission for publication of the material. Ellen M. Briggs, Todd R. Martz, Lynne Talley, Matthew Mazloff, Kenneth S. Johnson. The dissertation author was the primary investigator and author of this material.

Chapter 4, in full, is currently being prepared for publication of the material. Ellen M. Briggs, Todd R. Martz, Stephen V. Smith. The dissertation author was the primary investigator and author of this material.

VITA

2011 Bachelor of Science, University of Illinois, Urbana-Champaign

2014 Master of Science, University of California, San Diego

2017 Doctor of Philosophy, University of California, San Diego

PUBLICATIONS

Briggs, E. M., T. R. Martz, L. Talley, M. Mazloff, K. Johnson (In Revision), Physical and Biological drivers of biogeochemical tracers within the seasonal ice zone of the Southern Ocean from profiling floats, *Journal of Geophysical Research: Oceans*.

Briggs, E. M., S. Sandoval, A. Erten, Y. Takeshita, A. Kummel, T. R. Martz (Submitted), A solid state sensor for simultaneous measurement of total alkalinity and pH of seawater, *American Chemical Society: Sensors*.

Takeshita, Y., W. McGillis, **E. M. Briggs**, A. L. Carter, E. M. Donham, T. R. Martz, N. N. Price, and J. E. Smith (2016), Assessment of net community production and calcification of a coral reef using a boundary layer approach, *Journal of Geophysical Research: Oceans*, *121*(8), 5655-5671, doi:10.1002/2016JC011886.

Anderson, C. A., Jones, A. R., **Briggs, E. M.**, Novitsky, E. J., Kuykendall, D. W., Sottos, N. R., & Zimmerman, S. C. (2013). High-affinity DNA base analogs as supramolecular, nanoscale promoters of macroscopic adhesion. *Journal of the American Chemical Society*, *135*(19), 7288-7295.

ABSTRACT OF THE DISSERTATION

Expanding marine biogeochemical observations utilizing ISFET pH sensing technology and autonomous platforms

by

Ellen M. Briggs

Doctor of Philosophy in Oceanography

University of California, San Diego 2017

Professor Todd Martz, Chair

The ocean plays an integral role in the global carbon cycle and serves as the largest planetary reservoir for carbon. As more anthropogenic CO_2 is released to the atmosphere it is essential to understand and quantify the impact of elevated pCO_2 on the ocean's role in the uptake, transfer, and transformation of carbon as well as cascading effects on biogeochemical processes. Direct observations are limited in space and time due to shortage of autonomous technology available to effectively

monitor the aqueous carbon dioxide system at seasonal, interannual, and longer timescales. This dissertation describes novel sensors that are being developed and implemented to expand available marine biogeochemical observations.

The first two chapters describe the development of a solid state sensor capable of rapid and simultaneous measurement of pH and Total Alkalinity of seawater for monitoring the aqueous carbon dioxide system. This novel sensor requires no external reagents, has low power consumption, and meets the rugged demands required for integration with autonomous platforms. Chapter 1 focuses on the development and analytical assessment of the working sensor. Chapter 2 provides a more detailed description of all the processes and methods that were explored in reaching the working sensor described in Chapter 1.

Chapters 3 and 4 both use profiling floats equipped with existing biogeochemical sensing technology deployed through the Southern Ocean Carbon and Climate Observations and Modeling project to look at biogeochemical processes in the Southern Ocean. SOCCOM is a pilot program that will hopefully lead to global scale array of biogeochemical sensors on profiling floats. In Chapter 3, the influence of sea ice on the relative role of physical versus biological components of the pH and O_2 signal is explored. While Chapter 3 primarily focuses on organic biogeochemical processes, Chapter 4 focuses on the role of $CaCO_3$ reactions in the Southern Ocean carbon budget.

INTRODUCTION

Marine carbon cycle

Increased release of anthropogenic CO_2 will have profound impacts on climate with cascading effects on global- to regional-scale biogeochemical processes [*Feely et al.*, 2004; *Field et al.*, 2014; *Gruber et al.*, 2009]. The oceans serve as a carbon sink and have the capacity to absorb 70-80% of the projected CO_2 emissions over geologic timescales of hundreds of thousands years [*Sabine and Tanhua*, 2010]. On much shorter timescales, however, the rate of CO_2 uptake by the oceans is not keeping pace with the rate at which CO_2 is being emitted to the atmosphere [*Takahashi et al.*, 2009] as shown by open ocean observations of pCO_2 at Hawaii Ocean Time-series (HOT) [*Dore et al.*, 2009] and Bermuda Atlantic Time-series Study (BATS) stations [*Bates et al.*, 2012].

Solubility and biological carbon pumps regulate the exchange of carbon between the ocean interior and atmosphere [*Volk and Hoffert*, 1985]. With the sudden upward trend in atmospheric CO_2 resultant changes in seawater chemistry will impact the balance and interactions between biological and calcium carbonate cycles [*Feely et al.*, 2004; *Sabine and Tanhua*, 2010]. Complex feedback loops between these ecosystem-level biogeochemical cycles under a changing climate will influence the short term efficiency of the carbon pumps [*Joos et al.*, 1999; *Riebesell et al.*, 2007; *Sarmiento et al.*, 1998]. Thus, the ocean's key role in carbon uptake demands accurate constraint of the ocean carbon cycle in order to make assessments of future climate projections and the confounding impacts on marine ecosystems.

Observation of marine aqueous carbon dioxide system

Traditionally ship-based platforms have been used for open-ocean monitoring of the carbon cycle resulting in large gaps of observations in space and time. Discrete sampling is often insufficient for resolving many important features of marine biogeochemical cycles and subsequent feedbacks that occur at much shorter time scales [*Daly et al.*, 2004; *Prien*, 2007]. Even at longer timescales, observing the influence of the uptake of anthropogenic CO_2 on the natural multi-year variability and fluctuations of the open ocean carbon cycle will require widespread deployment of low-cost, high endurance sensors and platforms to expand the spatial and temporal range of observations [*Johnson et al.*, 2009]. It is necessary to reinforce that repeat hydrography will still remain a necessary and integral tool for long term ocean monitoring and autonomous sensor validation.

Direct, in situ measurements of ocean inorganic carbon chemistry including pH, total dissolved inorganic carbon (C_T), pCO_2, and Total Alkalinity (A_T) are desirable, but advancement in chemical sensor technology is still premature in terms of meeting the low power, robust design, accuracy, and stability requirements for use on autonomous platforms [*Johnson et al.*, 2009; *Martz et al.*, 2015; *Moore et al.*, 2009]. Combinations of either pH or pCO_2 with A_T or C_T are preferred for constraining carbonate speciation based on propagation of error of the best available analytical techniques [*Dickson and Riley*, 1978; *Millero*, 2007]. However, A_T and C_T analytical techniques are the most difficult to transfer to the in situ domain, and no carbon variable can be calculated more accurately than the combined parameters can be

measured [*Dickson and Riley*, 1978]. Thus, there is great need to develop new methods compatible with in situ technologies for measuring A_T and C_T autonomously with accuracy and precision comparable to the best analytical methods.

Total alkalinity is defined in the most general sense as the amount of strong acid required to reach an equivalence point corresponding to a specified acid-base equilibrium condition. Historically, seawater A_T was measured by titrating to the equivalence point of carbonic acid and bicarbonate. Though carbonate and bicarbonate typically account for 95% of seawater A_T, minor species including borate, phosphate, and other acid-base systems in seawater interact with protons during a titration [*Dickson*, 1981]. An exact definition of A_T that accounts for all of the significant seawater acid-base equilibria sets a mass balance relationship, referred to as a proton condition, that designates each species as proton acceptor (acid dissociation constant, $K_a < 10\text{-}4.5$) or proton donor ($K_a > 10\text{-}4.5$). Seawater A_T is then the excess of the proton acceptors over proton donors:

$$A_T = [HCO_3^-] + 2[CO_3^{2-}] + [B(OH)_4^-] + [OH^-] + [HPO_4^{2-}] +$$

$$2[PO_4^{3-}] + [SiO(OH)_3^-] + [NH_3] + [HS^-] + [B] \ldots \text{(proton acceptors)}$$

$$- [H^+] - [HSO_4^-] - [HF] - [H_3PO_4] - [HA] \ldots \text{(proton donors)}$$

where [HA] and [B] represent minor or unidentified species.

The standard procedure for measuring A_T uses a potentiometric titration monitored by a glass electrode [*Dickson et al.*, 2003]. A_T is calculated from titrant volume and electromotive force (emf) data using either modified Gran functions or a non-linear least squares approach. Other approaches have been developed using

chronopotentiometry [*Afshar et al.*, 2014] as well as spectrophotometry for single-point [*Li et al.*, 2013] and tracer monitored titrations [*Martz et al.*, 2006; *Spaulding et al.*, 2014]; however, few have reached the certainty and level of long-term accuracy and precision of the standard benchtop titration. Many of these techniques are limited to benchtop measurements due to instrument complexity, inability to miniaturize, power consumption, and excess reagents.

Robust chemical sensor technology presently exists for measuring the other two carbon variables, pH and pCO_2, as well as other biogeochemical tracers such as O_2 and nitrate autonomously in the ocean [*DeGrandpre*, 1993; *Johnson et al.*, 2013; *Körtzinger et al.*, 2005; *Martz et al.*, 2008]. However, combinations of these parameters are not always ideal for studying some important biogeochemical processes. For example, calcification and production have a highly collinear effect on pH and pCO_2 making this pair undesirable for distinguishing these processes [*Emerson et al.*, 2011; *Gray et al.*, 2011; *Millero*, 2007]. Decoupling between carbon and oxygen in the upper ocean, where the seasonal variability of near surface concentrations of O_2 is a reflection of rapid air-sea equilibrium and solubility effects rather than biological activity, inhibits the utility of the pH-O_2 pair for studying upper ocean biogeochemistry [*Keeling et al.*, 1993].

Despite some of these drawbacks, there is significant information that can be gained from autonomous pH, O_2, and other biogeochemical data as they are available over a much more sizable spatiotemporal domain. Much effort has been devoted to developing robust algorithms for estimating A_T which can be coupled with

autonomous pH measurements to derive the full aqueous carbon dioxide system at much greater spatiotemporal resolution than ship based measurements [*Carter et al.*, 2016; *Williams et al.*, 2017].

Biogeochemical sensors on profiling floats

Substantial advancement has been made in the physical oceanographic community due to the advent of Argo profiling floats in the late 90's [*Roemmich et al.*, 2009]. The global array of floats has reached a steady state of over 3000 floats corresponding to over 100,000 profiles a year of salinity, temperature, and pressure down to 2000 m. Significant progress has more recently been made to equip these Argo-type profiling floats with biogeochemical sensors in order to expand biogeochemical observations [*Bishop,* 2009; *Boss et al.,* 2008; *Gould et al.,* 2004; *Johnson et al.,* 2009; *Johnson and Coletti,* 2002; *Körtzinger et al.,* 2005; *Roemmich et al.,* 2009].

Through the Southern Ocean Carbon and Climate Observations and Modeling (SOCCOM) project, approximately 200 profiling floats equipped with temperature, salinity, pressure, O_2, pH, nitrate, and bio-optical sensors will be deployed in the Southern Ocean from 2014-2019. Multi-year surface and subsurface biogeochemical observations over complete annual cycles in regions that were previously inaccessible, such as under ice [*Wong and Riser,* 2013] and during austral winter are now realizable [*Roemmich et al.,* 2009].

The Southern Ocean plays a critical role in biogeochemical cycling and will be greatly impacted by changing climate and uptake of anthropogenic CO_2. Physical

dynamics of the Southern Ocean are the principal driving force of meridional overturning circulation and provide the primary window by which intermediate, deep, and bottom waters reach the surface and interact with the atmosphere [*Marshall and Speer*, 2012]. It is estimated that the Southern Ocean south of 44°S accounts for 25-30% of the annual oceanic uptake of anthropogenic CO_2 [*Mikaloff Fletcher et al.*, 2006] and supplies nutrients for up to 75% of the biological production that occurs north of 30°S [*Sarmiento et al.*, 2004]. However, compared to other ocean basins, observations in the Southern Ocean are extremely sparse and biased to the austral summer due to the remoteness and difficulty in making year-round measurements.

At the present, much of what we know about Southern Ocean biogeochemical dynamics has been derived from models, inversions, and very limited observations that often considerably disagree [*Majkut et al.*, 2014]. In addition to using these observations directly, these data will be used to analyze and improve earth system models for creating better projections of future climate. Specifically, these data will be assimilated into a biogeochemical Southern Ocean State Estimate (SOSE-BGC), an ocean general circulation model, to facilitate construction of a more robust and realistic biogeochemical-physical coupled estimate of the ocean state [*Galbraith et al.*, 2009; *Mazloff et al.*, 2010].

Dissertation Outline

Chapters 1 and 2 of this dissertation focus on the design and development of a solid state sensor for simultaneous measurement of A_T and pH of seawater utilizing ion selective field effect transistor (ISFET) pH-sensing technology. This dual carbon

parameter sensor will provide a rapid means (< 40 s) of measuring the aqueous carbon dioxide system. Without the requirement of external reagents, this low power, solid state sensor is ideal for in situ, autonomous platforms. With an initial precision of 0.5% A_T and 0.1% pH, this sensor has the potential to greatly expand our understanding of biogeochemical dynamics in a number of marine ecosystems by substantially increasing direct observations. Chapter 1 (submitted to ACS Sensors) describes the development and analytical assessment of the working sensor. Chapter 2 goes into greater detail into all the processes that were attempted to modify an ISFET that led to a working sensor.

In Chapters 3 (in revision, JGR Oceans) and 4 (in prep), biogeochemical sensor data from profiling floats deployed in the Southern Ocean as part of the SOCCOM project are used to investigate biogeochemical processes within the Southern Ocean. In Chapter 3, the influence of ice is explored on the relative role of physical versus biological drivers of pH and O_2 in the seasonal ice zone. Sea ice offers a unique condition where air-sea gas exchange is inhibited allowing the biological component of the chemical signal to dominate. As sea ice melts, ideal conditions are set up to facilitate an ice edge phytoplankton bloom. Rates of net community production and the role of the soft biological pump are explored within the seasonal ice zone.

The role of the $CaCO_3$ pump in the carbon cycle of the Southern Ocean is investigated in Chapter 4. There is evidence for large coccolithophore blooms that span the entire Southern Ocean accounting for up to 26% of the global pelagic

production of $CaCO_3$ yet there is very limited understanding of the complexity of the role of $CaCO_3$ reactions in coordination with the soft biological pump in exchanging CO_2 with the atmosphere. With more autonomous sensors being developed and deployed globally, our biogeochemical observations will be expanded greatly and the natural variability of the marine aqueous carbon dioxide system as well as the magnitude of the human footprint on the global carbon cycle can be better constrained.

References

Afshar, M. G., G. A. Crespo, X. Xie, and E. Bakker (2014), Direct alkalinity detection with ion-selective chronopotentiometry, *Analytical chemistry*, *86*(13), 6461-6470, doi:10.1021/ac500968c.

Bates, N. R., M. H. P. Best, K. Neely, R. Garley, A. G. Dickson, and R. J. Johnson (2012), Detecting anthropogenic carbon dioxide uptake and ocean acidification in the North Atlantic Ocean, *Biogeosciences*, *9*(7), 2509-2522, doi:10.5194/bg-9-2509-2012.

Bishop, J. (2009), Autonomous Observations of the Ocean Biological Carbon Pump, *Oceanography*, *22*(2), 182-193, doi:10.5670/oceanog.2009.48.

Boss, E., D. Swift, L. Taylor, P. Brickley, R. Zaneveld, S. Riser, M. J. Perry, and P. G. Strutton (2008), Observations of pigment and particle distributions in the western North Atlantic from an autonomous float and ocean color satellite, *Limnology and Oceanography*, *53*(5part2), 2112-2122, doi:10.4319/lo.2008.53.5_part_2.2112.

Carter, B. R., N. L. Williams, A. R. Gray, and R. A. Feely (2016), Locally interpolated alkalinity regression for global alkalinity estimation, *Limnology and Oceanography: Methods*, *14*(4), 268-277, doi:10.1002/lom3.10087.

Daly, K. L., R. H. Byrne, A. G. Dickson, S. M. Gallager, M. J. Perry, and M. K. Tivey (2004), Chemical and Biological Sensors for Time-Series Research: Current Status and New Directions, *Marine Technology Society Journal*, *38*(2), 121-143, doi:10.4031/002533204787522767.

DeGrandpre, M. D. (1993), Measurement of seawater pCO2 using a renewable-reagent fiber optic sensor with colorimetric detection, *Analytical chemistry*, *65*(4), 331-337, doi:10.1021/ac00052a005.

Dickson, A. G. (1981), An exact definition of total alkalinity and a procedure for the estimation of alkalinity and total inorganic carbon from titration data, *Deep Sea Research Part A. Oceanographic Research Papers*, *28*(6), 609-623, doi:http://dx.doi.org/10.1016/0198-0149(81)90121-7.

Dickson, A. G., J. D. Afghan, and G. C. Anderson (2003), Reference materials for oceanic CO2 analysis: a method for the certification of total alkalinity, *Marine Chemistry*, *80*(2–3), 185-197, doi:http://dx.doi.org/10.1016/S0304-4203(02)00133-0.

Dickson, A. G., and J. P. Riley (1978), The effect of analytical error on the evaluation of the components of the aquatic carbon-dioxide system, *Marine Chemistry*, *6*(1), 77-85, doi:http://dx.doi.org/10.1016/0304-4203(78)90008-7.

Dore, J. E., R. Lukas, D. W. Sadler, M. J. Church, and D. M. Karl (2009), Physical and biogeochemical modulation of ocean acidification in the central North Pacific, *Proceedings of the National Academy of Sciences of the United States of America*, *106*(30), 12235-12240, doi:10.1073/pnas.0906044106.

Emerson, S., C. Sabine, M. F. Cronin, R. Feely, S. E. Cullison Gray, and M. DeGrandpre (2011), Quantifying the flux of CaCO3and organic carbon from the surface ocean using in situ measurements of O2, N2, pCO2, and pH, *Global Biogeochemical Cycles*, *25*(3), n/a-n/a, doi:10.1029/2010gb003924.

Feely, R. A., C. L. Sabine, K. Lee, W. Berelson, J. Kleypas, V. J. Fabry, and F. J. Millero (2004), Impact of anthropogenic CO2 on the CaCO3 system in the oceans, *Science*, *305*(5682), 362-366, doi:10.1126/science.1097329.

Field, C. B., V. R. Barros, K. J. Mach, M. D. Mastrandrea, M. van Aalst, W. N. Adger, D. J. Arent, J. Barnett, R. Betts, T. E. Bilir, J. Birkmann, J. Carmin, D. D. Chadee, A. J. Challinor, M. Chatterjee, W. Cramer, D. J. Davidson, Y. O. Estrada, J. P. Gattuso, Y. Hijioka, O. Hoegh-Guldberg, H. Q. Huang, G. E. Insarov, R. N. Jones, R. S. Kovats, P. R. Lankao, J. N. Larsen, I. J. Losada, J. A. Marengo, R. F. McLean, L. O. Mearns, R. Mechler, J. F. Morton, I. Niang, T. Oki, J. M. Olwoch, M. Opondo, E. S. Poloczanska, H. O. Pörtner, M. H. Redsteer, A. Reisinger, A. Revi, D. N. Schmidt, M. R. Shaw, W. Solecki, D. A. Stone, J. M. R. Stone, K. M. Strzepek, A. G. Suarez, P. Tschakert, R. Valentini, S. Vicuña, A. Villamizar, K. E. Vincent, R. Warren, L. L. White, T. J. Wilbanks, P. P. Wong, and G. W. Yohe (2014), Technical Summary, in *Climate Change 2014: Impacts, Adaptation, and Vulnerability. Part A: Global and Sectoral Aspects. Contribution of Working Group II to the Fifth Assessment Report of the Intergovernmental Panel on Climate Change*, edited by C. B. Field, et al., pp. 35-94, Cambridge University Press, Cambridge, United Kingdom and New York, NY, USA.

Galbraith, E. D., A. Gnanadesikan, J. P. Dunne, and M. R. Hiscock (2009), Regional impacts of iron-light colimitation in a global biogeochemical model, *Biogeosciences Discuss.*, *6*(4), 7517-7564, doi:10.5194/bgd-6-7517-2009.

Gould, J., D. Roemmich, S. Wijffels, H. Freeland, M. Ignaszewsky, X. Jianping, S. Pouliquen, Y. Desaubies, U. Send, and K. Radhakrishnan (2004), Argo profiling floats bring new era of in situ ocean observations, *Eos, Transactions American Geophysical Union*, *85*(19), 185-191, doi:10.1029/2004EO190002.

Gray, S. E. C., M. D. DeGrandpre, T. S. Moore, T. R. Martz, G. E. Friederich, and K. S. Johnson (2011), Applications of in situ pH measurements for inorganic carbon calculations, *Marine Chemistry*, *125*(1), 82-90, doi:http://dx.doi.org/10.1016/j.marchem.2011.02.005.

Gruber, N., M. Gloor, S. E. Mikaloff Fletcher, S. C. Doney, S. Dutkiewicz, M. J. Follows, M. Gerber, A. R. Jcobson, F. Joos, K. Lindsay, D. Menemenlis, A. Mouchet, S. A. Müller, J. L. Sarmiento, and T. Takahashi (2009), Oceanic sources, sinks, and transport of atmospheric CO2, *Global Biogeochemical Cycles*, *23*(1), doi:10.1029/2008gb003349.

Johnson, K. S., W. Berelson, E. Boss, Z. Chase, H. Claustre, S. Emerson, N. Gruber, A. Körtzinger, M. J. Perry, and S. Riser (2009), Observing Biogeochemical Cycles at Global Scales with Profiling Floats and Gliders: Prospects for a Global Array, *Oceanography*, *22*(3), 216-225, doi:10.5670/oceanog.2009.81.

Johnson, K. S., and L. J. Coletti (2002), In situ Ultraviolet spectrophotometry for high resolution and long-term monitoring of nitrate, bromide and bisulfide in the ocean, *Deep Sea Research Part I: Oceanographic Research Papers*, *49*, 1291-1305, doi:http://dx.doi.org/10.1016/S0967-0637(02)00020-1.

Johnson, K. S., L. J. Coletti, H. W. Jannasch, C. M. Sakamoto, D. D. Swift, and S. C. Riser (2013), Long-Term Nitrate Measurements in the Ocean Using the in situ Ultraviolet Spectrophotometer: Sensor Integration into the APEX Profiling Float, *Journal of Atmospheric and Oceanic Technology*, *30*(8), 1854-1866, doi:10.1175/jtech-d-12-00221.1.

Joos, F., G.-K. Plattner, T. F. Stocker, O. Marchal, and A. Schmittner (1999), Global Warming and Marine Carbon Cycle Feedbacks on Future Atmospheric CO2, *Science, 284*(5413), 464-467, doi:10.1126/science.284.5413.464.

Keeling, R. F., R. P. Najjar, M. L. Bender, and P. P. Tans (1993), What atmospheric oxygen measurements can tell us about the global carbon cycle, *Global Biogeochemical Cycles*, *7*(1), 37-67.

Körtzinger, A., J. Schimanski, and U. Send (2005), High quality oxygen measurements from profiling floats: A promising new technique, *Journal of Atmospheric and Oceanic Technology*, *22*(3), 302-308, doi:http://dx.doi.org/10.1175/JTECH1701.1.

Li, Q., F. Wang, Z. A. Wang, D. Yuan, M. Dai, J. Chen, J. Dai, and K. A. Hoering (2013), Automated Spectrophotometric Analyzer for Rapid Single-Point Titration of Seawater Total Alkalinity, *Environmental science & technology*, *47*(19), 11139-11146, doi:10.1021/es402421a.

Majkut, J. D., B. R. Carter, T. L. Frolicher, C. O. Dufour, K. B. Rodgers, and J. L. Sarmiento (2014), An observing system simulation for Southern Ocean carbon dioxide uptake, *Philosophical transactions. Series A, Mathematical, physical, and engineering sciences*, *372*(2019), 20130046, doi:10.1098/rsta.2013.0046.

Marshall, J., and K. Speer (2012), Closure of the meridional overturning circulation through Southern Ocean upwelling, *Nature Geoscience*, *5*(3), 171-180, doi:10.1038/ngeo1391.

Martz, T. R., K. Daly, R. Byrne, J. Stillman, and D. Turk (2015), Technology for Ocean Acidification Research: Needs and Availability, *Oceanography*, *25*(2), 40-47, doi:10.5670/oceanog.2015.30.

Martz, T. R., A. G. Dickson, and M. D. DeGrandpre (2006), Tracer Monitored Titrations: Measurement of Total Alkalinity, *Analytical chemistry*, *78*(1817-1826), doi:10.1021/ac0516133.

Martz, T. R., K. S. Johnson, and S. C. Riser (2008), Ocean metabolism observed with oxygen sensors on profiling floats in the South Pacific, *Limnology and Oceanography*, *53*(5part2), 2094-2111, doi:10.4319/lo.2008.53.5_part_2.2094.

Mazloff, M. R., P. Heimbach, and C. Wunsch (2010), An Eddy-Permitting Southern Ocean State Estimate, *Journal of Physical Oceanography*, *40*(5), 880-899, doi:10.1175/2009jpo4236.1.

Mikaloff Fletcher, S. E., N. Gruber, A. R. Jacobson, S. C. Doney, S. Dutkiewicz, M. Gerber, M. Follows, F. Joos, K. Lindsay, and D. Menemenlis (2006), Inverse estimates of anthropogenic CO2 uptake, transport, and storage by the ocean, *Global Biogeochemical Cycles*, *20*(2), doi:10.1029/2005GB002530.

Millero, F. J. (2007), The Marine Inorganic Carbon Cycle, *Chemical Reviews*, *107*, 308-341, doi:10.1021/cr0503557.

Moore, T. S., K. M. Mullaugh, R. R. Holyoke, A. S. Madison, M. Yücel, and G. W. Luther (2009), Marine Chemical Technology and Sensors for Marine Waters:

Potentials and Limits, *Annual review of marine science*, *1*(1), 91-115, doi:doi:10.1146/annurev.marine.010908.163817.

Prien, R. D. (2007), The future of chemical in situ sensors, *Marine Chemistry*, *107*(3), 422-432, doi:http://dx.doi.org/10.1016/j.marchem.2007.01.014.

Riebesell, U., K. G. Schulz, R. G. J. Bellerby, M. Botros, P. Fritsche, M. Meyerhofer, C. Neill, G. Nondal, A. Oschilies, J. Wohlers, and E. Zollner (2007), Enhanced biological carbon consumption in a high CO2 ocean, *Nature*, *450*(7169), 545-548, doi:http://www.nature.com/nature/journal/v450/n7169/suppinfo/nature06267_S1.html.

Roemmich, D., G. Johnson, S. Riser, R. Davis, J. Gilson, W. B. Owens, S. Garzoli, C. Schmid, and M. Ignaszewski (2009), The Argo Program: Observing the Global Oceans with Profiling Floats, *Oceanography*, *22*(2), 34-43, doi:10.5670/oceanog.2009.36.

Sabine, C. L., and T. Tanhua (2010), Estimation of anthropogenic CO2 inventories in the ocean, *Annual review of marine science*, *2*, 175-198, doi:10.1146/annurev-marine-120308-080947.

Sarmiento, J. L., N. Gruber, M. A. Brzezinski, and J. P. Dunne (2004), High-latitude controls of thermocline nutrients and low latitude biological productivity, *Nature*, *427*(6969), 56-60, doi:10.1038/nature02127.

Sarmiento, J. L., T. M. Hughes, R. J. Stouffer, and S. Manabe (1998), Simulated response of the ocean carbon cycle to anthropogenic climate warming, *Nature*, *393*(6682), 245-249, doi:10.1038/30455.

Spaulding, R. S., M. D. DeGrandpre, J. C. Beck, R. D. Hart, B. Peterson, E. H. De Carlo, P. S. Drupp, and T. R. Hammar (2014), Autonomous in situ measurements of seawater alkalinity, *Environmental science & technology*, doi:10.1021/es501615x.

Takahashi, T., S. C. Sutherland, R. Wanninkhof, C. Sweeney, R. A. Feely, D. W. Chipman, B. Hales, G. Friederich, F. Chavez, C. Sabine, A. Watson, D. C. E. Bakker, U. Schuster, N. Metzl, H. Yoshikawa-Inoue, M. Ishii, T. Midorikawa, Y. Nojiri, A. Körtzinger, T. Steinhoff, M. Hoppema, J. Olafsson, T. S. Arnarson, B. Tilbrook, T. Johannessen, A. Olsen, R. Bellerby, C. S. Wong, B. Delille, N. R. Bates, and H. J. W. de Baar (2009), Climatological mean and decadal change in surface ocean pCO2, and net sea–air CO2 flux over the global oceans, *Deep Sea Research Part II: Topical Studies in Oceanography*, *56*(8-10), 554-577, doi:10.1016/j.dsr2.2008.12.009.

Volk, T., and M. I. Hoffert (1985), Ocean carbon pumps: Analysis of relative strengths and efficiencies in ocean-driven atmospheric CO2 changes, *The Carbon Cycle and Atmospheric CO2: Natural Variations Archean to Present*, 99-110, doi:10.1029/GM032p0099.

Williams, N. L., L. W. Juranek, R. A. Feely, K. S. Johnson, J. L. Sarmiento, L. D. Talley, A. G. Dickson, A. R. Gray, R. Wanninkhof, J. L. Russell, S. C. Riser, and Y. Takeshita (2017), Calculating surface ocean pCO2 from biogeochemical Argo floats equipped with pH: An uncertainty analysis, *Global Biogeochemical Cycles*, 591-604, doi:10.1002/2016GB005541.

Wong, A. P. S., and S. C. Riser (2013), Modified shelf water on the continental slope north of Mac Robertson Land, East Antarctica, *Geophysical Research Letters*, *40*(23), 6186-6190, doi:10.1002/2013gl058125.

CHAPTER 1: A SOLID STATE SENSOR FOR SIMULTANEOUS MEASUREMENT OF TOTAL ALKALINITY AND PH OF SEAWATER

Abstract

A novel design is demonstrated for a solid state, reagent-less sensor capable of rapid and simultaneous measurement of pH and Total Alkalinity (A_T) using ion sensitive field effect transistor (ISFET) technology to provide a simplified means of characterization of the aqueous carbon dioxide system through measurement of two "master variables": pH and A_T. ISFET-based pH sensors that achieve 0.001 precision are widely used in various oceanographic applications. A modified ISFET is demonstrated to perform a nL-scale acid-base titration of A_T in under 40 s. This method of measuring A_T, a Coulometric Diffusion Titration, involves electrolytic generation of titrant, H^+, through the electrolysis of water on the surface of the chip via a microfabricated electrode eliminating the requirement of external reagents. Characterization has been performed in seawater as well as titrating individual components (i.e. OH^-, HCO_3^-, CO_3^{2-}, $B(OH)_4^-$, PO_4^{3-}) of seawater A_T. The seawater measurements are consistent with the design in reaching the benchmark goal of 0.5% precision in A_T over the range of seawater A_T of ~2200-2500 μmol kg^{-1}.

1 Introduction

Ship-based platforms have traditionally been used for open-ocean monitoring of the carbon cycle resulting in large gaps of observations in space and time. Discrete sampling is often insufficient for resolving many important features of marine

biogeochemical cycles and subsequent feedbacks that occur at much shorter time scales [*Daly et al.*, 2004; *Prien*, 2007]. Direct, in situ measurements of ocean inorganic carbon chemistry including pH, total dissolved inorganic carbon (C_T), partial pressure of CO_2 (pCO_2), and Total Alkalinity (A_T) are desirable, but current chemical sensor technology does not fulfill the low power, robust design, accuracy, and stability requirements for use on autonomous platforms [*Johnson et al.*, 2009; *Martz et al.*, 2015; *Moore et al.*, 2009]. Combinations of either pH or pCO_2 with A_T or C_T are preferred for constraining carbonate speciation based on propagation of error of the best available analytical techniques [*Dickson and Riley*, 1978; *Millero*, 2007]. However, A_T and C_T analytical techniques are the most difficult to measure in situ, and no carbon variable can be calculated more accurately than the combined parameters can be measured [*Dickson and Riley*, 1978]. Commercially available autonomous sensors for pH and pCO_2 are not capable of simultaneous measurements, and these variables are the least desirable carbon pair for differentiating some key biogeochemical processes such as production and calcification [*Millero*, 2007]. Therefore, there is great need to develop new methods compatible with in situ technologies for measuring A_T and C_T autonomously with accuracy and precision comparable to the best analytical methods.

Globally, seawater A_T spans a relatively narrow range from ~2200-2500 [*Key et al.*, 2004]. In the open surface ocean, A_T is dominantly controlled by simple physical processes (e.g. precipitation, evaporation) and can often be estimated accurately from measurements of temperature and salinity [*Carter et al.*, 2014; *Lee et*

al., 2006; *Millero et al.*, 1998]. However, such empirical relationships for A_T are not as well-developed beneath the surface and become invalid in many dynamic environments at depth and at the ocean surface where processes such as freshwater input and calcium carbonate formation lead to non-conservative behavior in A_T [*Bates et al.*, 1996; *Cross et al.*, 2013; *Millero et al.*, 1998]. Coccolithophore blooms, sediment porewaters, coral reefs, river mouths, and coastal shelves are general examples where non-conservative behavior is known, however these regions play a significant role in biogeochemical processes and conservative relationships cannot be applied.

The standard procedure for measuring seawater A_T uses a potentiometric titration monitored by a glass electrode [*Dickson et al.*, 2003]. A_T is calculated from titrant volume and electromotive force (emf) data using either modified Gran functions or a non-linear least squares approach. Other approaches have been developed using chronopotentiometry [*Afshar et al.*, 2014] as well as spectrophotometry for single-point [*Li et al.*, 2013] and tracer monitored titrations [*Martz et al.*, 2006; *Spaulding et al.*, 2014]; however, many of these techniques are limited to benchtop measurements due to instrument complexity, inability to miniaturize, power consumption, and excess reagents. Furthermore, few alternative techniques capable of autonomous measurements have reached the certainty and level of long term accuracy and precision of the standard benchtop titration.

Ion sensitive field effect transistor (ISFET) technology is becoming increasingly popular in pH sensing devices [*Bergveld*, 2003]. For instance, Honeywell

has commercialized the DuraFET which is a pH sensing ISFET-based combination electrode currently used in industrial as well as oceanographic applications [*Bresnahan et al.*, 2014; *Johnson et al.*, 2016; *Martz et al.*, 2010; *Sandifer and Voycheck*, 1999]. As solid state pH sensors, ISFETs offer advantages relative to glass electrodes including reduced drift as well as the ruggedness required for in situ, autonomous use. Notably, glass electrodes suffer from notoriously high impedance (up to giga ohms) whereas ISFETs-based pH sensors are inherently low impedance (tens to hundreds of ohms) leading to significantly improved stability over time.

An ISFET is analogous to the better known metal oxide semiconductor field effect transistor (MOSFET) with the metal oxide gate replaced by a conventional reference electrode. As described by *Johnson et al.* [2016], the Honeywell Durafet ISFET consists of an N doped silicon substrate which includes two P doped regions which are referred to as the source and drain. Between these two regions is a conduction region referred to as the channel. On top of this channel is an insulator (from here on referred to as the gate) which might be a deposited metal oxide or a non-oxide insulator such as silicon nitride [*Bergveld*, 2003]. This channel insulator will exchange hydrogen ion and develop a potential at the insulator solution interface. The resultant interfacial potential controls the shape of the conductance channel of the FET and thus the flow of current between the source and drain (Figure 1.1). Outside this channel region is a deposited field insulator (identified in Figure 1.1 as “Insulator”). This field insulator may or may not employ the same material as the channel insulator.

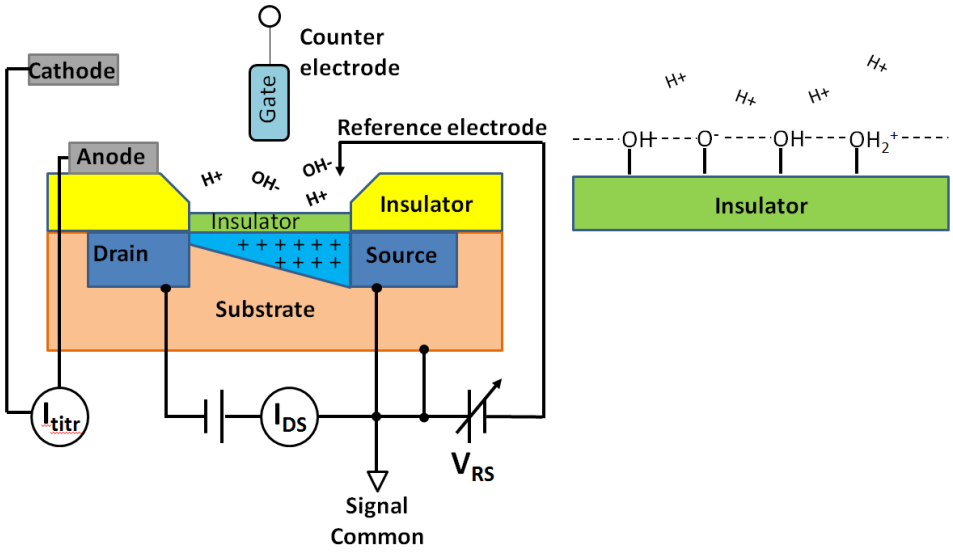

Figure 1.1. Schematic of operating principle of ISFET.

Here ISFET technology is modified to design and test a solid state, reagentless sensor capable of rapid and simultaneous measurement of A_T and pH. By integrating a coulometric actuator device with an ISFET, a nL-scale acid-base titration can be simultaneously executed and measured on a single ISFET chip. Microfabrication enables the actuator to be placed within microns of the gate thereby reducing the sample volume to nanoliters and decreasing the response time to 40 s. The sensor is optimized for and evaluated over a narrow range of A_T, ~2200-2500 μmol kg^{-1}, representative of seawater. This dual pH-A_T sensor provides a means of continuous, direct measurement of aqueous carbon dioxide chemistry.

2 Methods

2.1 Theory

A MOSFET employs a metal oxide channel insulator on top of which a metal is deposited. This metal is referred to as the gate. ISFETs remove this gate electrode and expose the underlying channel insulator to the sample solution [*Baxter et al.*, 1995; *Connery and Shaffer*, 1989]. This now removed gate, or substitute metal conductor, remains in solution and is referred to as the counter electrode. This counter electrode can be thought of a wetted gate electrode. The function of this counter is the same as the analogous counter electrode employed in analytical voltammetry or amperometry. The counter is a low impedance electrode which is used for ISFET control. It controls drain voltage and drain current and its EMF is neither defined nor important for proper function of the ISFET. Because the counter electrode EMF is a suitable metal such as the removed gate electrode, it is of low impedance, and allows a pathway for parasitic leakage currents.

In typical ISFET operation, a constant drain to source voltage (V_{DS}) is applied, and a feedback circuit is used to maintain a constant drain to source current (I_{DS}). The resultant source to reference electrode voltage (V_{RS}) is proportional to pH as described by the Nernst equation (Equation 1) where R is the universal gas constant (8.3146 J K^{-1} mol^{-1}), T is temperature in Kelvin, F is the Faraday constant (96,485 Coulomb mol^{-1}), and a_H and a_{Cl} are the activity coefficients of hydrogen and chloride ions [*Bergveld*, 2003; *Takeshita et al.*, 2014]. Refer to Table 1.1 for a summary of the abbreviations that will be used in the remainder of the text.

$$V_{RS} \propto \frac{RTln(10)}{F} log(a_H a_{Cl}) \quad (1)$$

Table 1.1. List of variables corresponding to ISFET and pH-A_T operation.

Variable	Description	Optimal Value
$\mathbf{I_{DS}}$	Drain to source current	188 μA
$\mathbf{V_{DS}}$	Drain to source voltage	1.25 V
$\mathbf{V_{RS}}$	Source to reference electrode voltage proportional to pH	~-1-1 V
$\mathbf{I_A}$	Anodic current for generating titrant	0-40 μA
$\mathbf{V_A}$	Voltage required to maintain anodic constant current	≤2 V
$\mathbf{I_{L1}}$	Substrate leakage current	<20 nA
$\mathbf{I_{L2}}$	Counter leakage current	<10 nA

By integrating a coulometric actuator device with an ISFET, a nL-scale acid-base titration can be simultaneously executed and measured on a single ISFET chip [*Olthuis and Bergveld*, 1995; *Olthuis et al.*, 1990b; *Olthuis et al.*, 1989; *Van der Schoot and Bergveld*, 1985]. Titrant, H^+, is generated through the electrolysis of water by applying an anodic current pulse (I_A) to an actuator electrode with respect to a counter electrode in an analyte solution:

$$\text{Anode: } 2H_2O \rightarrow 4H^+ + 4e^- + O_2$$

$$\text{Cathode: } 2H_2O + 2e^- \rightarrow 2OH^- + H_2$$

By placing the actuator electrode on the surface of the ISFET near the gate, the pH can be rapidly measured as the analyte solution is titrated with the electrolytically generated H^+ as shown in Figure 1.2.

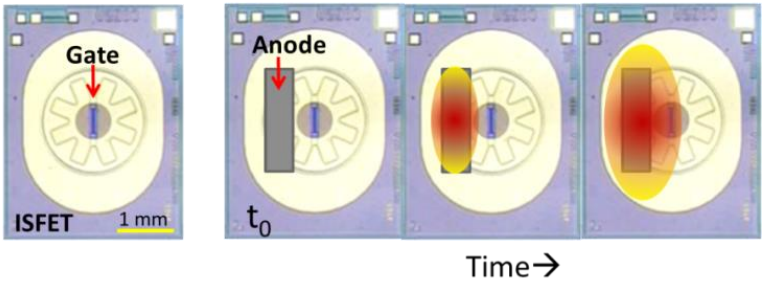

Figure 1.2. Non-modified ISFET (left) and conceptual schematic of diffusion of the 'titrated zone' (orange) across the gate upon generation of titrant.

This "coulometric sensor-actuator system" as it was originally referred to by its inventors, [*Olthuis and Bergveld*, 1995; *Olthuis et al.*, 1990a; *Van der Schoot and Bergveld*, 1985] was later named a "Flash Titration" when commercialized by Orion in the early 2000's [*Van der Schoot et al.*, 2005]. Later, Bakker's group adopted the term Flash Titration to refer to a different method utilizing ion selective membrane chronopotentiometry [*Gemene and Bakker*, 2008]. Unfortunately, the commercialized product was not successful primarily due to short lifetime and lack of universality demanded by industry. With the significant advances made in ISFET technology by Honeywell, field tested by the oceanographic community, coupled with the narrow range of seawater A_T, it is expected that the coulometric sensor-actuator system method can be successfully integrated with the Honeywell ISFET to produce a dual pH-A_T sensor fine-tuned for seawater. Because the Orion Flash Titration system is no longer a product and in order to avoid confusion with the field of ion selective membrane chronopotentiometry, we have chosen to refer to the technique used in the ISFET-based coulometric sensor-actuator system as a coulometric diffusion titration (CDT).

CDT can be described by a one-dimensional diffusive mass transport model [*Olthuis et al.*, 1990a]. Referring to Figure 1.4, the topside of the ISFET is viewed on the x-plane and the actuator electrode can be thought of as a semi-infinite plane positioned at x = 0 μm parallel to the gate at x = x_g μm. At time t_0, the concentration of a basic analyte is defined as $C_{B,\,bulk}$ at both the actuator electrode and ISFET gate. At t_1, an anodic current pulse is applied to the actuator electrode to generate H^+. At t_2 (blue curve), the proton acceptors are depleted at the anode such that $C_B = 0$ at x = 0. This condition is expressed by the Sand equation, t_{Sand}:

$$t_{Sand} = \left[\frac{C_{B,Bulk} F \sqrt{\pi D_B}}{2 j_c}\right]^2$$

where D_i is the diffusion coefficient of species i, F is the Faraday constant, and j_c is the current density at the actuator electrode. The reaction horizon moves across the x-plane t_3 (red curve) to t_4 (green curve). The equivalence point is reached at t_{end} when $C_B(x_g, t_4) = 0$ which is the sum of t_{Sand} and t_{delay}, the time it takes for the reaction plane to reach the ISFET gate. Thus, C_B, (or A_T) is linearly proportional to $(t_{end})^{1/2}$. A CDT can be completed within 1-60 s depending on the bulk concentration, operating current, and distance between the actuator electrode and gate, x_g. The ISFET response time is on the order of milliseconds and is sufficient to detect the endpoint of the titration with high accuracy.

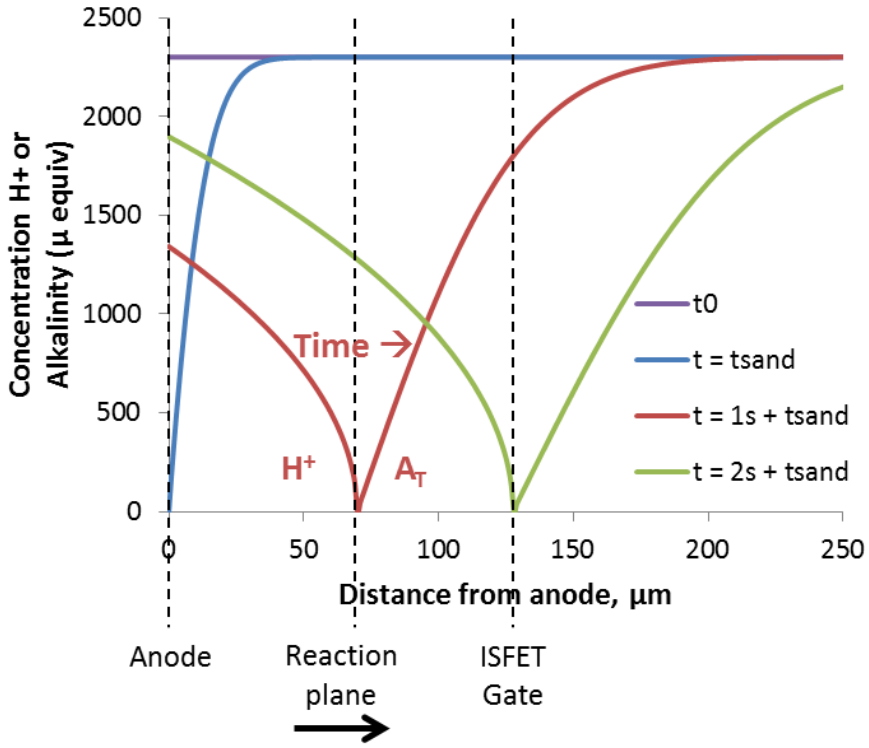

Figure 1.3. CDT model for seawater showing the time evolution of the concentration profiles of excess titrant (H^+) and analyte (A_T) and their position relative to the anode and ISFET gate. The endpoint is reached when the zero-point of the concentration profile reaches the ISFET gate (green curve).

2.2 Sensor Design

The ISFET die, acquired from Honeywell, was modified by adding an electrode to the topside of the chip proximal to the gate using backend processing techniques. The ISFET chips were assembled into a mechanical mask device as shown in Figure 1.5 and precisely positioned to expose an area 100-150 µm from the gate of the chip.

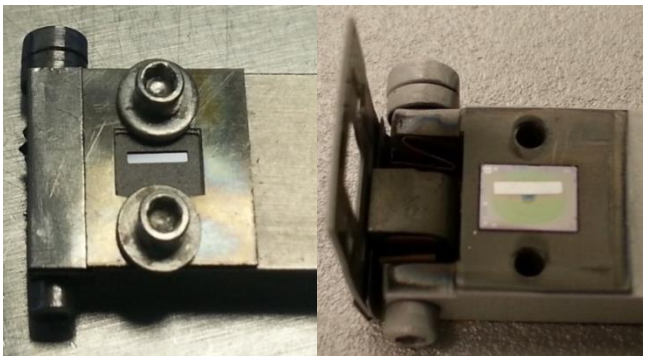

Figure 1.4. Mechanical mask used to pattern an actuator electrode on the surface of the ISFET. The ISFET was placed in the holder and the electrode was then deposited onto the exposed region of the ISFET precisely aligned within 100-150 μm of the gate.

The exposed ISFET surface was cleaned using an O_2 plasma followed by deposition of a 2.5 μm electrically insulating layer of SiO_2 by plasma enhanced chemical vapor deposition (PECVD) at 350° C. 50 nm of Ti was deposited and exposed to atmosphere to form an insulating layer of TiO_2. Then 200 nm of Ti was deposited as an adhesion layer followed by deposition of 500 nm of Pt by argon sputtering. The modified ISFETs were removed from the mechanical mask and then annealed at 350° C for 3 minutes. The multistep insulator deposition was performed with a single shadow mask so that all the materials are self-aligned and ensures a resistance of greater than 100 giga ohms to minimize leakage of current on the actuator electrode into the ISFET.

Modified ISFETs (Figure 1.5) were assembled into specialized housing using gold wirebonding to make electrical contact to the source, drain, and substrate on the backside of the ISFET. Encapsulation was achieved by a mechanical means using a series of o-rings. Electrical contact was made to the actuator electrode (anode) on the

topside of the ISFET by threading a gold wire bonded to the electrode through the series of o-rings to the inside of the housing. The Nernstian response of the modified ISFETs was assessed in NIST buffers with pH ranging from 4-11. The sensor system was comprised of the modified ISFET with actuator anode, Ag/AgCl reference electrode, titanium counter electrode, and platinum cathode.

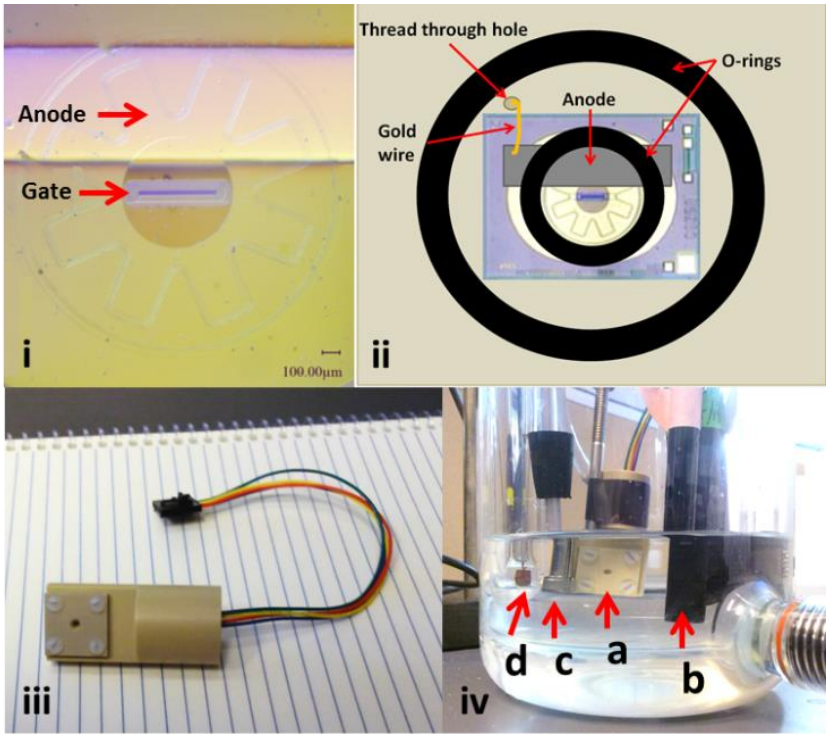

Figure 1.5. Modified ISFET (i) showing the Pt anode positioned approximately 100 µm from the gate. Electrical contact between the anode is made by threading a gold wire bonded to the topside of the ISFET through two o-rings to the interior of the housing (ii). The fully assembled housing is shown in panel iii. In the bottom right panel (iv) the modified ISFET (a) is positioned in the jacketed beaker with a reference electrode (b), counter electrode (c), and the cathode (d).

The proprietary Honeywell electronics for operating the ISFET required modification to increase the I_{DS} feedback speed and to measure diagnostic variables

including leakage currents (I_{L1} and I_{L2}) as well as drain to source voltage and current (V_{DS} and I_{DS}). Simultaneous measurements of V_{RS}, leakage currents, I_A, and V_A as well as programmable control over I_A served as critical diagnostic and development tools. Standalone electronics and embedded software were developed to provide the groundwork for enabling field deployment and integration with autonomous platforms. A custom ARM microcontroller (TI Cortex TM4C123G) was utilized to provide a programmable actuator with output I_A and V_A monitoring circuitry as well as the modified Honeywell circuitry for operating the ISFET and for monitoring system integrity. Software was developed using Code Composer Studio integrated development environment in C/C++ for basic operation of the pH-A_T sensor.

2.3 Analytical Assessment

Initial sensor performance was tested on benchtop in NaOH and other A_T components (results not shown), standard solutions of HCO_3^- and CO_3^{2-} in a NaCl background, and seawater with initial A_T ranging from 2250-2600 μmol kg^{-1}. The operating current for proton generation was set to a constant value ranging from 10-40 μA. Standard dilutions were performed by adding 10 aliquots of deionized water with NaCl background to dilute solutions through the range of oceanic A_T. In tests, 20 titration curves were recorded at each sample concentration and a simple pump was run for 15 s to flush the surface of the ISFET followed by a 5 s hold to allow the solution to settle between titrations. All analyses were performed in a jacketed beaker to maintain sample temperature near ambient at 22.5 ˚C. The sampling rate was set to 20 Hz for V_{RS} and 2k Hz for diagnostic measurements (I_{L1}, I_{L2}, I_A, V_A, V_{DS}). Signal

processing of raw data collected from the ARM board was carried out in Matlab. At each concentration, the titration curves were smoothed and the last 15 endpoints, corresponding to the final inflection point of the titration, were averaged.

3 Results

Titration curves produced in standard solutions of HCO_3^- and CO_3^{2-} in 0.5 M NaCl background are shown in Figure 1.6. The first inflection point corresponds to t_{end} for CO_3^{2-} and the final inflection point corresponds to t_{end} for A_T.

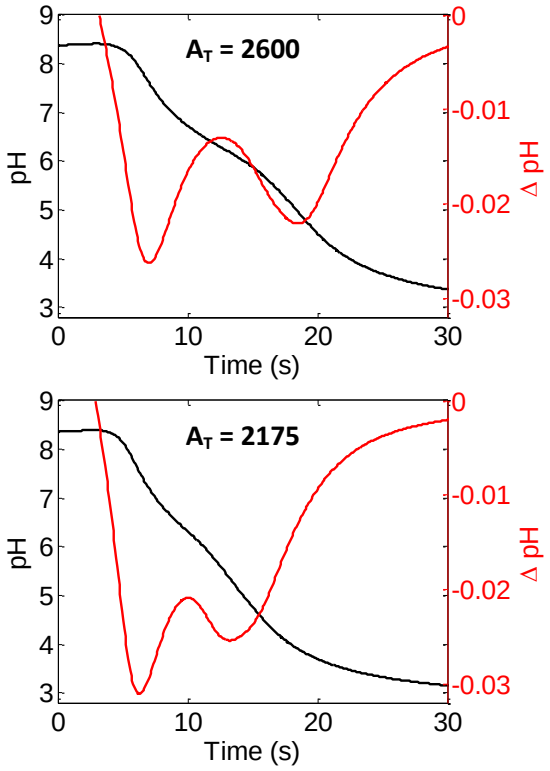

Figure 1.6. Titration curve (black) and first derivative (red) for standard solutions of HCO_3^- and CO_3^{2-} in 0.5 M NaCl background with A_T of 2600 (top) and 2175 (bottom) µmol kg^{-1}. The first inflection point corresponds to CO_3^{2-} endpoint and the second inflection point corresponds to the A_T. The time required to reach the A_T endpoint decreased from ~18 s for the solution with greater A_T to ~13 s for the solution with reduced A_T as anticipated.

Standard dilutions of the prepared solution of HCO_3^- and CO_3^{2-} in 0.5 M NaCl background with starting A_T of 2600 µmol kg^{-1} down to ~2100 µmol kg^{-1} are shown in Figure 1.7. The error analysis in Figure 1.7 was performed by repeating the measurement 15 times in one solution and the error bars represent one standard deviation from the mean at each concentration. Excellent linearity between the A_T and $(t_{end})^{1/2}$ was observed over the range of seawater A_T with an R^2 of 0.999 and mean standard deviation of ±7.6 µmol kg^{-1}. Standard dilutions were repeated in seawater with a starting A_T of 2450 µmol kg^{-1} yielded a similar result as shown in Figure 1.8 with an R^2 of 0.998 and mean standard deviation of ±11 µmol kg^{-1}. Distance of the actuator electrode from the ISFET gate as well as current density was not identical between the modified ISFETs used to produce Figures 1.7 and 1.8 resulting in slight differences in the time required to reach t_{end} and slope over the range of A_T.

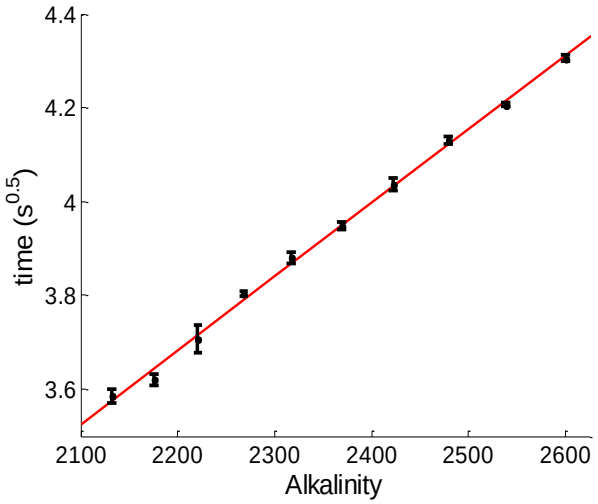

Figure 1.7. Standard dilution of a prepared solution of HCO_3^- and CO_3^{2-} in 0.5 M NaCl background with a starting A_T of 2600 µmol kg^{-1}. Excellent linearity is observed over the range of seawater A_T (~2200-2500 µmol kg^{-1}) with an R^2 of 0.999 and mean standard deviation of ±7.6 µmol kg^{-1}.

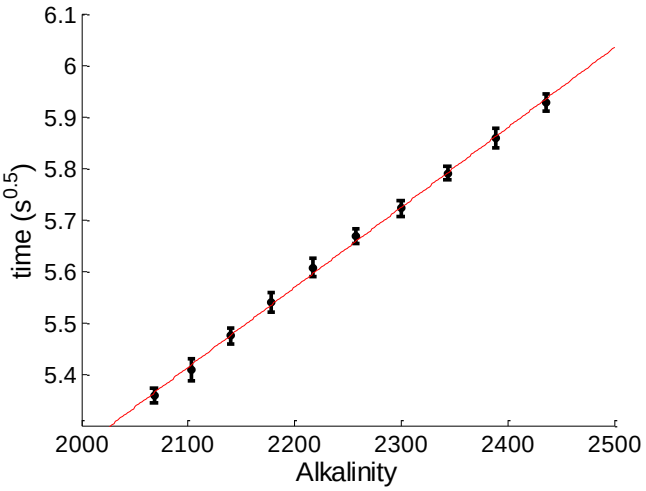

Figure 1.8. A_T as a function of time (s $^{0.5}$) for the standard dilution of seawater collected in the North Indian Ocean with a starting A_T of 2450 µmol kg^{-1}. Excellent linear relationship is observed over the range of seater A_T with an R^2 of 0.998 and mean standard deviation of ±11 µmol kg^{-1}.

An example of output diagnostic measurements is shown in Figure 1.9. Optimal values for I_{L1} and I_{L2} are less than 20 and 10 nA respectively. Values much greater than this are indicative of inferior ISFET performance and interference of the actuator electrode. I_A and corresponding V_A on the anode were monitored to verify the current was constant and reached the input set point during the titration. It was determined that an operating current between 10-15 µA was required to fully resolve the two endpoints (Figure 1.6) over the range of seawater A_T for sensors with the actuator electrode positioned between 100-150 µm from the gate of the ISFET. This corresponds to reaching the endpoint of the titration in ~25-40 s.

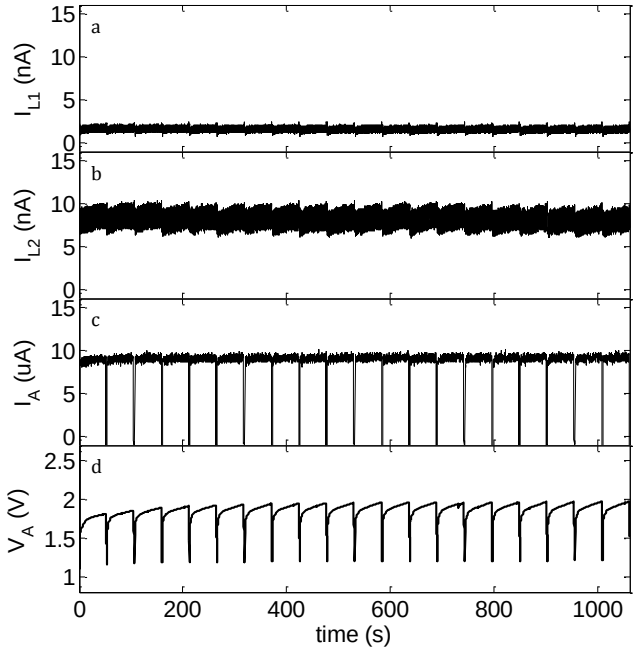

Figure 1.9. Diagnostic measurements I_{L1} (a), I_{L2} (b), I_A (c), and V_A (d) recorded during 20 titrations in seawater. Each titration was run for approximately 50 s.

4 Discussion

Modification of the fully processed ISFET chips was limited to backend processing techniques; typical processing procedures could not be used without damaging the integrity of the fully processed ISFET chip. This resulted in using nonstandard procedures for depositing an electrode onto the surface of the chip. Typically, photolithography would be used to deposit an electrode on the surface of a chip to achieve maximum control over dimension and precise alignment, however, the high temperatures required to deposit a highly insulating SiO_2 film restricted the use of photoresist and necessitated development of a mechanical, non-polymer, means of patterning the chip. Iterations of shadow mask design and refinement of the alignment of the ISFET in the mask were required to reduce “creep” of deposited material

underneath the mask and to more precisely position the electrode within 100-150 μm from the gate.

The actuator electrode could not be deposited directly onto the surface of the ISFET because pathways opened up for current through the chip, detected by disruption in leakage currents. Methods were explored to increase the resistivity between the actuator electrode and the substrate of the chip. Typically highly insulating SiO_2 is thermally deposited at 1000 ˚C which is far too high for a fully processed ISFET. Depositing a thick layer of SiO_2 through PECVD became the best option for attaining a highly insulating layer while remaining below the upper limit of temperature exposure for the fully processed ISFET. Other lower temperature methods were tested including argon RF sputtered SiO_2 which allowed use of photolithographic patterning, however the insulating properties of the films were insufficient.

The voltage required to drive the electrolysis of seawater for generating protons, the proton evolution efficiency, and the stability of proton evolution are a factor of electrode material choice and deposition technique. The proton evolution efficiency need not be 100% but the short term stability between titrations is imperative and this long term stability of proton evolution will determine the frequency of calibration required. Electrode choice became a critical component of sensor success; it was realized that gold, even though considered ideally inert, could not be used for the electrode material in seawater. Gold is susceptible to dissolution when current is applied in the presence of complexing ions, such as Cl^-, CN^-, and Br^- [*Cherevko et al.*, 2013], and the gold anode visually disappeared in a matter of minutes

when current was applied to the anode in seawater or NaCl electrolyte background. Platinum is now used in place of gold as the electrode material for both the anode and cathode.

There appears to be a warmup or conditioning of the Pt actuating electrode required to reach a stable measurement. When first powered, running higher current (~40 μA) for approximately 20 minutes through the anode is required to achieve stable electrochemical generation of titrant. With short duration pauses (>3 minutes), there is an upward drift in the time required to reach the endpoint in the first few titration curves. Therefore, the first 5 measurements were removed in a set of 20 titrations during the standard dilutions. This drift is not observed in continuous measurement mode when the current is turned off for only ~20 s between titrations when the pump is running to refresh the surface of the chip.

Additional increases in stability and sensitivity can be achieved by optimizing the sensor, including: location of the actuator electrode with respect to the gate, current density, and electrode material. In addition, robust ISFET encapsulation is not trivial and presents a major challenge in terms of both experimental reproducibility and production scalability [*Oelßner et al.,* 2005]. New methods are being explored to integrate the actuator electrode into the sensor housing rather than physically depositing the electrode on the surface of the ISFET which would remove the direct modification of the ISFET and simplify sensor assembly. Field testing of the current sensor configuration will be achievable after further assessment of sensor calibration and proton generation efficiency over a range of temperature and pressure.

5 Conclusions

A microscale, highly insulating coulometric actuator device was integrated with an ISFET, enabling a nL-scale acid-base titration on a single ISFET chip. By placing the actuator electrode on the surface of the ISFET near the gate, the pH can be rapidly measured as the analyte solution is titrated with the electrolytically generated H^+. This sensor is capable of direct, on the fly measurement of the aqueous carbon dioxide system. A single A_T titration can be completed in less than 40 s, no external reagents are required, and there are no complex moving parts making this sensor ideal for autonomous, in situ application. An initial approximate precision of 0.5% A_T was achieved by performing a series of standard dilutions in seawater and in a prepared solution of HCO_3^- and CO_3^{2-}. The estimated resolution of this dual pH-A_T sensor translates to approximately 0.5 and 0.7% error in Total Dissolved Inorganic Carbon (C_T) and pCO_2 respectively and would enable quantification of biogeochemical processes where strong gradients exist over short distances and in rapidly changing environments.

Acknowledgements

This work was supported by grant NSF OCE Award 1155122. This material is also based upon work supported by the National Science Foundation Graduate Research Fellowship under Grant No. DGE-1144086. I would like to acknowledge Bob Carlson and Jim Connery from Honeywell for their expertise during the development of this sensor. I would also like to thank crew and scientists on GO-SHIP cruise I09N for assisting with collecting seawater for preliminary sensor assessment.

Chapter 1, in full, is currently being prepared for submission for publication of the material. Ellen M. Briggs, Sergio Sandoval, Ahmet Erten, Yuichiro Takeshita, Andrew C. Kummel, Todd R. Martz. The dissertation author was the primary investigator and author of this material.

References

Afshar, M. G., G. A. Crespo, X. Xie, and E. Bakker (2014), Direct alkalinity detection with ion-selective chronopotentiometry, *Analytical chemistry*, *86*(13), 6461-6470, doi:10.1021/ac500968c.

Bates, N. R., A. F. Michaels, and A. H. Knap (1996), Alkalinity changes in the Sargasso Sea: geochemical evidence of calcification?, *Marine Chemistry*, *51*(4), 347-358, doi:http://dx.doi.org/10.1016/0304-4203(95)00068-2.

Baxter, R., J. Connery, J. Fogel, and S. Silverthorne (1995), ESD Protection of ISFET sensors, in *US Patent 5,407,854*, edited, General Signal Corp.

Bergveld, P. (2003), Thirty years of ISFETOLOGY: What happened in the past 30 years and what may happen in the next 30 years, *Sensors and Actuators B: Chemical*, *88*(1), 1-20, doi:http://dx.doi.org/10.1016/S0925-4005(02)00301-5.

Bresnahan, P. J., T. R. Martz, Y. Takeshita, K. S. Johnson, and M. LaShomb (2014), Best practices for autonomous measurement of seawater pH with the Honeywell Durafet, *Methods in Oceanography*, *9*(0), 44-60, doi:http://dx.doi.org/10.1016/j.mio.2014.08.003.

Carter, B. R., J. R. Toggweiler, R. M. Key, and J. L. Sarmiento (2014), Processes determining the marine alkalinity and calcium carbonate saturation state distributions, *Biogeosciences*, *11*(24), 7349-7362, doi:10.5194/bg-11-7349-2014.

Cherevko, S., A. A. Topalov, A. R. Zeradjanin, I. Katsounaros, and K. J. J. Mayrhofer (2013), Gold dissolution: towards understanding of noble metal corrosion, *RSC Advances*, *3*(37), 16516, doi:10.1039/c3ra42684j.

Connery, J. G., and E. W. Shaffer, Jr. (1989), Instrument for potentiometric electrochemical measurements in earth grounded solutions avoiding parasitic current problems, edited, p. 6 pp, General Signal Corp., USA

Cross, J. N., J. T. Mathis, N. R. Bates, and R. H. Byrne (2013), Conservative and non-conservative variations of total alkalinity on the southeastern Bering Sea shelf, *Marine Chemistry*, *154*, 100-112, doi:10.1016/j.marchem.2013.05.012.

Daly, K. L., R. H. Byrne, A. G. Dickson, S. M. Gallager, M. J. Perry, and M. K. Tivey (2004), Chemical and Biological Sensors for Time-Series Research: Current Status and New Directions, *Marine Technology Society Journal*, *38*(2), 121-143, doi:10.4031/002533204787522767.

Dickson, A. G., J. D. Afghan, and G. C. Anderson (2003), Reference materials for oceanic CO2 analysis: a method for the certification of total alkalinity, *Marine Chemistry*, *80*(2–3), 185-197, doi:http://dx.doi.org/10.1016/S0304-4203(02)00133-0.

Dickson, A. G., and J. P. Riley (1978), The effect of analytical error on the evaluation of the components of the aquatic carbon-dioxide system, *Marine Chemistry*, *6*(1), 77-85, doi:http://dx.doi.org/10.1016/0304-4203(78)90008-7.

Gemene, K. L., and E. Bakker (2008), Direct Sensing of Total Acidity by Chronopotentiometric Flash Titrations at Polymer Membrane Ion-Selective Electrodes, *Analytical chemistry*, *80*(10), 3743-3750, doi:10.1021/ac701983x.

Johnson, K. S., W. Berelson, E. Boss, Z. Chase, H. Claustre, S. Emerson, N. Gruber, A. Körtzinger, M. J. Perry, and S. Riser (2009), Observing Biogeochemical Cycles at Global Scales with Profiling Floats and Gliders: Prospects for a Global Array, *Oceanography*, *22*(3), 216-225, doi:10.5670/oceanog.2009.81.

Johnson, K. S., H. W. Jannasch, L. J. Coletti, V. A. Elrod, T. R. Martz, Y. Takeshita, R. J. Carlson, and J. G. Connery (2016), Deep-Sea DuraFET: A Pressure Tolerant pH Sensor Designed for Global Sensor Networks, *Analytical chemistry*, *88*(6), 3249-3256, doi:10.1021/acs.analchem.5b04653.

Key, R. M., A. Kozyr, C. L. Sabine, K. Lee, R. Wanninkhof, J. L. Bullister, R. A. Feely, F. J. Millero, C. Mordy, and T. H. Peng (2004), A global ocean carbon climatology: Results from Global Data Analysis Project (GLODAP), *Global Biogeochemical Cycles*, *18*(4), n/a-n/a, doi:10.1029/2004gb002247.

Lee, K., L. T. Tong, F. J. Millero, C. L. Sabine, A. G. Dickson, C. Goyet, G.-H. Park, R. Wanninkhof, R. A. Feely, and R. M. Key (2006), Global relationships of total alkalinity with salinity and temperature in surface waters of the world's oceans, *Geophysical Research Letters*, *33*(19), doi:10.1029/2006gl027207.

Li, Q., F. Wang, Z. A. Wang, D. Yuan, M. Dai, J. Chen, J. Dai, and K. A. Hoering (2013), Automated Spectrophotometric Analyzer for Rapid Single-Point

Titration of Seawater Total Alkalinity, *Environmental science & technology*, *47*(19), 11139-11146, doi:10.1021/es402421a.

Martz, T. R., K. Daly, R. Byrne, J. Stillman, and D. Turk (2015), Technology for Ocean Acidification Research: Needs and Availability, *Oceanography*, *25*(2), 40-47, doi:10.5670/oceanog.2015.30.

Martz, T. R., J. G. Connery, and K. S. Johnson (2010), Testing the Honeywell Durafet for seawater pH applications, *Limnology and Oceanography: Methods*, *8*, 172-184, doi:10.4319/lom.2010.8.172.

Martz, T. R., A. G. Dickson, and M. D. DeGrandpre (2006), Tracer Monitored Titrations: Measurement of Total Alkalinity, *Analytical chemistry*, *78*(1817-1826), doi:10.1021/ac0516133.

Millero, F. J. (2007), The Marine Inorganic Carbon Cycle, *Chemical Reviews*, *107*, 308-341, doi:10.1021/cr0503557.

Millero, F. J., K. Lee, and M. Roche (1998), Distribution of alkalinity in the surface waters of the major oceans, *Marine Chemistry*, *60*(1–2), 111-130, doi:http://dx.doi.org/10.1016/S0304-4203(97)00084-4.

Moore, T. S., K. M. Mullaugh, R. R. Holyoke, A. S. Madison, M. Yücel, and G. W. Luther (2009), Marine Chemical Technology and Sensors for Marine Waters: Potentials and Limits, *Annual review of marine science*, *1*(1), 91-115, doi:doi:10.1146/annurev.marine.010908.163817.

Oelßner, W., J. Zosel, U. Guth, T. Pechstein, W. Babel, J. G. Connery, C. Demuth, M. Grote Gansey, and J. B. Verburg (2005), Encapsulation of ISFET sensor chips, *Sensors and Actuators B: Chemical*, *105*(1), 104-117, doi:10.1016/j.snb.2004.05.009.

Olthuis, W., and P. Bergveld (1995), Integrated coulometric sensor-actuator devices, *Mikrochimica Acta*, *121*(1-4), 191-223, doi:10.1007/BF01248251.

Olthuis, W., J. Luo, B. H. Van der Schoot, P. Bergveld, M. Bos, and W. E. Van der Linden (1990a), Modelling of non-steady-state concentration profiles at ISFET-based coulometric sensor—actuator systems, *Analytica Chimica Acta*, *229*(0), 71-81, doi:http://dx.doi.org/10.1016/S0003-2670(00)85111-9.

Olthuis, W., J. Luo, B. H. van der Schoot, J. G. Bomer, and P. Bergveld (1990b), Dynamic behaviour of ISFET-based sensor-actuator systems, *Sensors and Actuators B: Chemical*, *1*(1–6), 416-420, doi:http://dx.doi.org/10.1016/0925-4005(90)80241-Q.

Olthuis, W., B. H. Van Der Schoot, F. Chavez, and P. Bergveld (1989), A dipstick sensor for coulometric acid-base titrations, *Sensors and Actuators*, *17*(1–2), 279-283, doi:http://dx.doi.org/10.1016/0250-6874(89)80092-7.

Prien, R. D. (2007), The future of chemical in situ sensors, *Marine Chemistry*, *107*(3), 422-432, doi:http://dx.doi.org/10.1016/j.marchem.2007.01.014.

Sandifer, J. R., and J. J. Voycheck (1999), A review of biosensor and industrial applications of pH-ISFETs and an evaluation of Honeywell's "DuraFET", *Microchimica Acta*, *131*(1-2), 91-98, doi:10.1007/PL00021393.

Spaulding, R. S., M. D. DeGrandpre, J. C. Beck, R. D. Hart, B. Peterson, E. H. De Carlo, P. S. Drupp, and T. R. Hammar (2014), Autonomous in situ measurements of seawater alkalinity, *Environmental science & technology*, doi:10.1021/es501615x.

Takeshita, Y., T. R. Martz, K. S. Johnson, and A. G. Dickson (2014), Characterization of an Ion Sensitive Field Effect Transistor and Chloride Ion Selective Electrodes for pH Measurements in Seawater, *Analytical chemistry*, *86*(22), 11189-11195, doi:10.1021/ac502631z.

Van der Schoot, B., and P. Bergveld (1985), An ISFET-based microlitre titrator: integration of a chemical sensor—actuator system, *Sensors and Actuators*, *8*(1), 11-22, doi:http://dx.doi.org/10.1016/0250-6874(85)80020-2.

Van der Schoot, B., P. Van der Wal, N. de Rooij, and S. West (2005), Titration-on-a-chip, chemical sensor–actuator systems from idea to commercial product, *Sensors and Actuators B: Chemical*, *105*(1), 88-95, doi:http://dx.doi.org/10.1016/j.snb.2004.02.058.

CHAPTER 2: ENGINEERING METHODS AND DESIGN FOR THE DEVELOPMENT OF THE DUAL TOTAL ALKALINITY AND PH SENSOR FOR SEAWATER

1 Introduction

The goal of this Chapter is to provide a detailed description of all the methods that were explored in developing the dual pH-A_T sensor described in Chapter 1. As outlined in Chapter 1, an ion sensitive field effect transistor (ISFET) was modified to perform a nano-liter titration in less than 40 s by the method of coulometric diffusion titration (CDT) [*Bergveld*, 2003; *Olthuis et al.*, 1990; *Van der Schoot et al.*, 2005]. A CDT could be performed on the surface of the ISFET by depositing an actuator electrode within 100-150 μm from the gate. Multiple approaches were attempted to modify and encapsulate the ISFET leading to a successful sensor design.

The un-modified Honeywell ISFET chip has three electrical contacts on the backside, corresponding to the source, drain, and substrate of the FET (Figure 2.1). The purpose of backside contacts is isolation of the electrical drive circuit while the pH-sensitive gate is exposed to the test solution. In previous designs, contact was made to the source, drain, and substrate on the topside of the ISFET and encapsulation was achieved using resin coatings to isolate the electrodes from the test solution [*Baxter*, 1985; *Oelßner et al.*, 2005]. This form of encapsulation is in part responsible for the reduced lifetime of the early ISFETs. The Honeywell ISFETs utilize a through-chip or vertical interconnect access (via) between the top and back sides of the chip in order to facilitate more robust encapsulation using a mechanical seal. In terms of

oceanographic application, further encapsulation design has been developed to reach pressure capability of 2000 dbar on Argo type profiling floats [*Johnson et al.*, 2016]. By adding an actuator electrode to the topside of the ISFET, once again electrical contact needs to be made to the topside of the chip. This has led to the development and testing of multiple approaches to modify and encapsulate ISFETs.

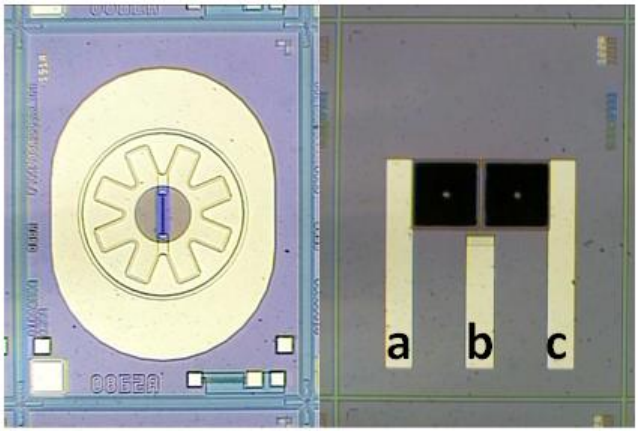

Figure 2.1. Topside (left) and backside (right) of non-modified ISFET. The source (a or c), substrate (b), and drain (a or c) are located on the backside of the ISFET.

2 ISFET Modification

2.1 Through-Hole Processing (THP) approach for electrode contacts

2.1.1 Introduction: The first approach to modify the ISFET, through-hole processing approach (THP), involved mimicking the electrode-contact pair similar to the existing chip design. The backside vias in the original chip design are built up during the fabrication process whereas here we are adding the backside vias during post-fabrication of a fully functional ISFET [*Baxter*, 1985]. This restricts the methods available for modifying the ISFET to backend processing techniques. THP was

thought to provide a more robust means to separate electrical contacts from the mechanical media seal or o-ring used to package the chip into the waterproof housing. Key steps in this method include the through-chip etching process and specialized techniques required for masking and etching.

2.1.2 Methods: The THP steps are shown schematically in Figure 2.2. The backside of the ISFET was cleaned by oxygen etching and patterned using photolithography to expose a 200 μm square on the backside of the chip. The surface oxide on the backside of the ISFET was etched as the first step in etching the through-hole. The photoresist was removed and then the topside surface of the ISFET was cleaned by oxygen etching, patterned using photolithography to expose a 100 μm square, and the surface oxide was etched on the topside of the chip. Both sides of the ISFET were then once again cleaned by oxygen etching and patterned using photolithography to expose a 200 μm square on the backside of the chip that is precisely aligned with the topside etched square and a 100 × 1000 μm rectangle on the topside of the chip overlapping the etched feature for depositing the actuator electrode. Ti was deposited on the topside of the ISFET as an adhesion layer followed by Au.

The through-hole was then etched from the backside of the ISFET using the Bosch process, a deep reactive ion etch, until reaching the gold electrode on the topside of the chip. The photoresist was removed from both sides of the chip and the backside was cleaned by oxygen etching and patterned using photolithography to expose a rectangular region for depositing the contact pad on the backside of the chip that overlapped with the through-hole. Ti was deposited as an adhesion layer followed

by Au. Excess material was deposited to ensure Au reached all the way down the through- hole to make electrical contact with the electrode on the topside of the ISFET. The final outcome of the THP approach is shown in Figure 2.3.

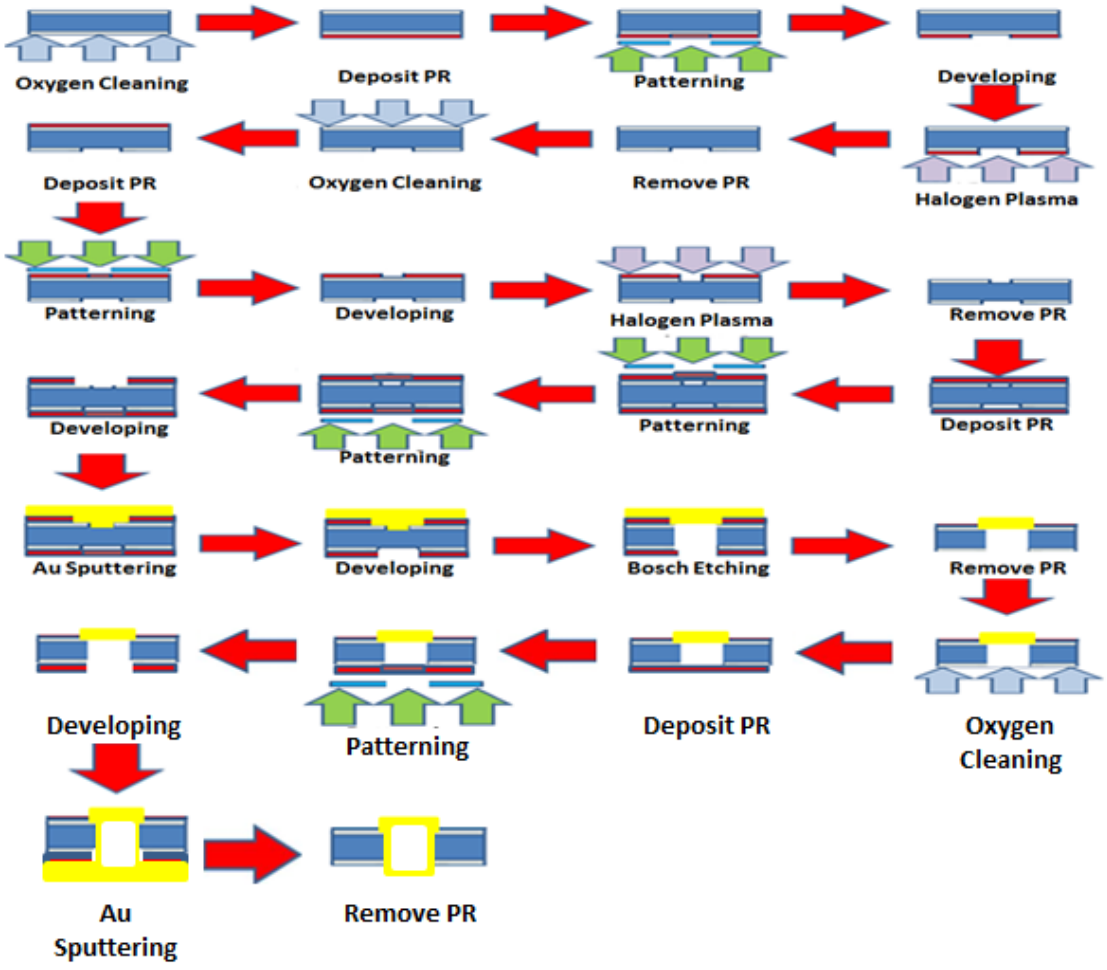

Figure 2.2. Simplified flow diagram of the steps involved in the THP approach. Halogen plasma refers to the oxide etch step. The PR (photoresist) is developed after patterning to expose the region for deposition of electrode material.

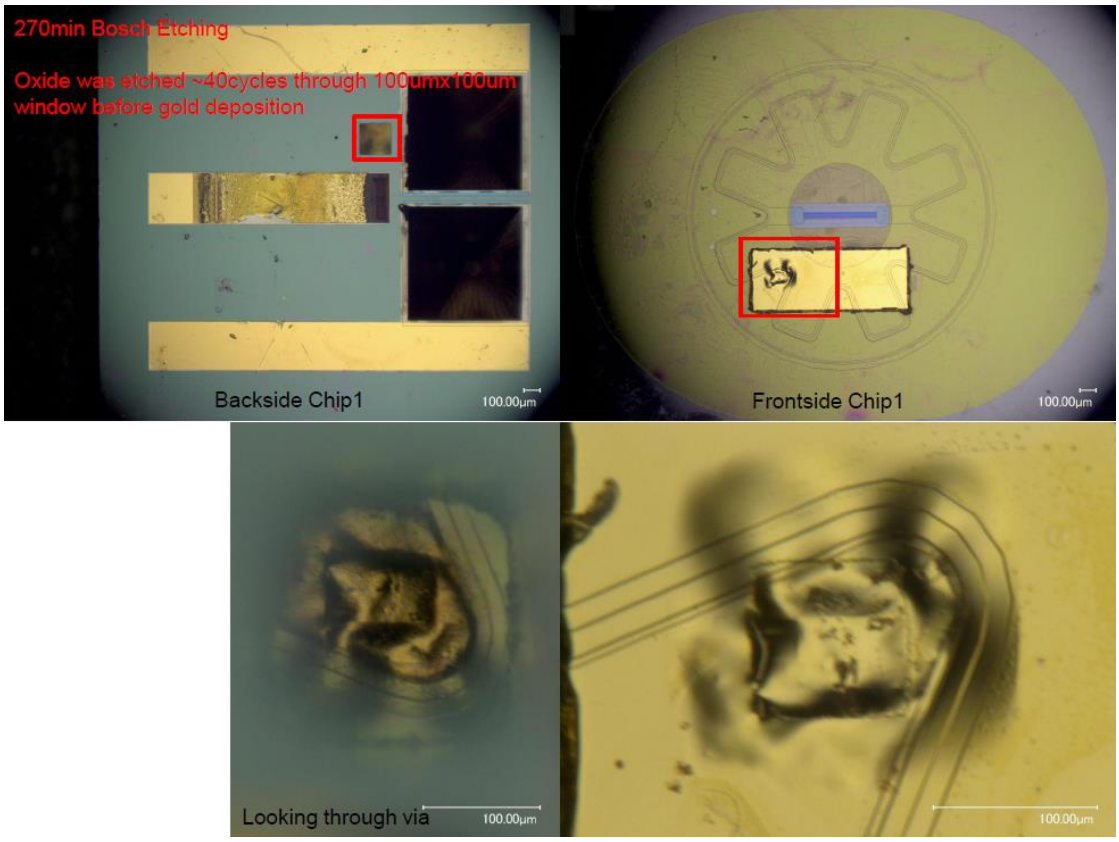

Figure 2.3. Backside of modified ISFET (top left) showing contact pad and through-hole making electrical contact to the electrode on the topside of the ISFET (top right). A zoomed in view through the via from the backside of the ISFET (bottom left) shows that the chip was completely etched to the topside electrode (bottom right).

2.1.3 Results & Discussion: THP was ultimately abandoned due to the complexity of steps required in using only backend processing techniques. The typical procedure for adding backside vias could not be applied to a fully processed ISFET. Patterning using traditional photolithographic techniques (i.e. spin coating) was challenging due to the rough topography of the backside of the chip which led to bubbles and inadequate coverage. Spin coated photoresists were replaced with a tape-like photoresist and led to the development of a specialized roll-on photoresist process.

The principle challenges of the Bosch process were to develop a small taper angle so the hole could later be coated with gold and to stop the etch process before etching the top surface gold contact. It was challenging to etch the hole all the way to the topside electrode and the photoresist was often damaged during the etching steps leading to destruction of the ISFET. The walls of the Bosch etched through-hole were steep which led to difficulty in depositing Au all the way down the hole to reach the topside electrode. The established geometry of the fully processed ISFET introduced restraints on dimensions and position of electrode and processing.

A combination of Bosch and KOH etching was attempted to taper the walls of the through-hole in order to make it feasible to deposit materials on the walls of the through-hole as shown in Figure 2.4. Unfortunately, the roll-on photoresist was insufficient at protecting the ISFET during the KOH etch and other masking techniques would have needed to been explored to make this process work.

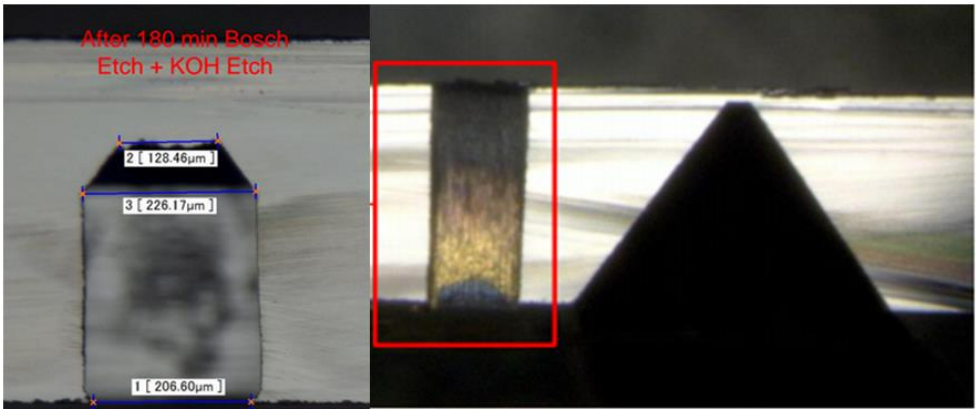

Figure 2.4. Cross section of an ISFET modified by the THP approach. The Bosch process (right, red rectangle) produced straight cavity walls whereas the KOH etch part way through the process tapered the walls (left) making it easier to deposit gold all the way down the through-hole to make electrical contact between the backside contact pad and the topside electrode.

The conditions required for etching also made it challenging to remove the photoresist. The atmosphere-produced oxide layer on the walls of the through-hole was insufficient at isolating the deposited Au from the substrate of the ISFET. This would have further required depositing an insulating oxide layer (i.e. SiO_2) on the etched walls of the through-hole while leaving the topside contact pad exposed. This would have been extremely challenging considering it was difficult just to coat the sidewalls entirely with Au to make initial connection to the topside electrode.

2.2. Wrap-Around Processing (WAP) approach for electrode contacts

2.2.1 Introduction: Due to the complexity of the THP method a secondary approach was explored where a trace was deposited over the edge of the ISFET to make electrical contact between the topside electrode and backside contact pad. The wrap-around processing (WAP) approach was at first very simplistic. However, isolating the ISFET substrate from the trace over the edge of the chip was not trivial and again multiple adjustments to the approach were attempted to try to achieve a successful sensor design. Figure 2.5 shows the comparison of the THP and WAP approaches.

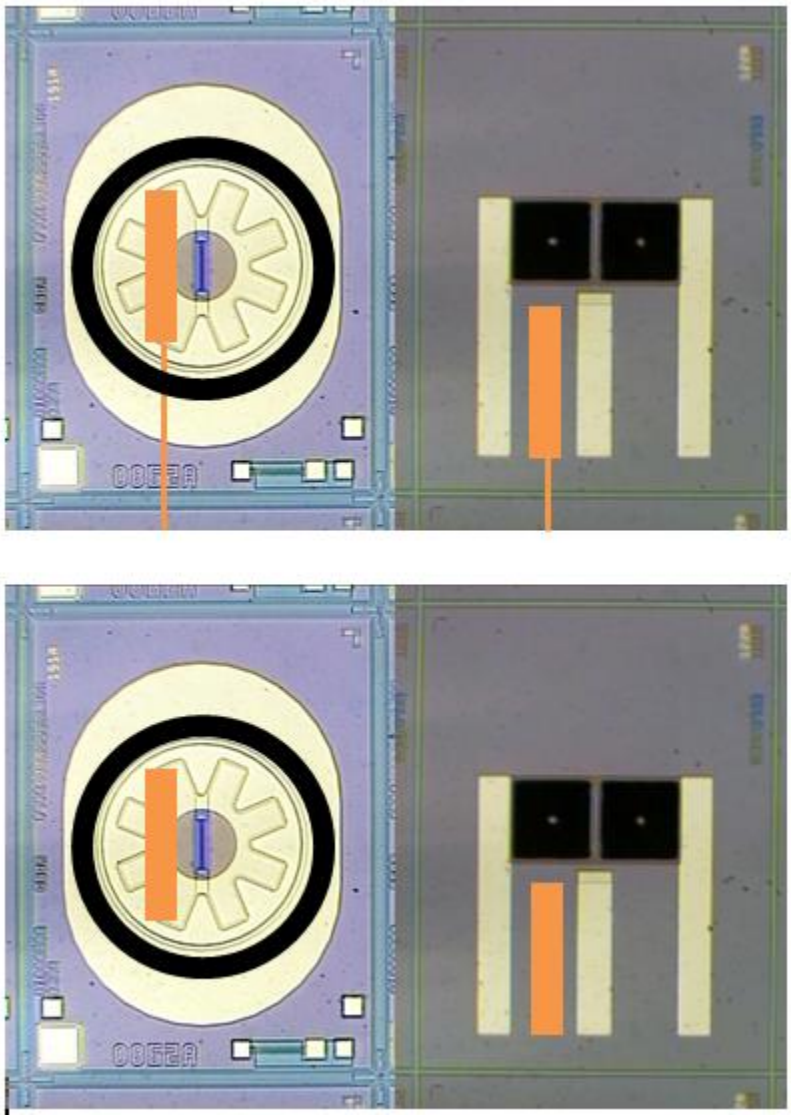

Figure 2.5. WAP (top) versus THP (bottom) approaches. Both methods allowed for use of a mechanical o-ring seal.

2.2.2 Methods: The WAP steps are shown schematically in the flow diagram in Figure 2.6. Figure 2.7 shows a photomicrograph of a typical chip following WAP. A photomask was designed that allowed an additional electrode to be deposited on the topside and operate as the cathode (Figure 2.7). Both sides of the ISFET were cleaned

by oxygen etching and both sides were patterned using photolithography. Tape was used to mask the edges of the chip while exposing a trace to connect the top and backside patterned regions. Samples were mounted onto a stand-up holder so that the deposition of the topside electrode, backside contact and over the edge trace could be accomplished simultaneously. SiO_2 was deposited by RF sputtering to isolate the trace along the edge of the chip from the substrate and then Ti was deposited as an adhesion layer followed by Au on all exposed surfaces. The photoresist was then removed leaving behind a topside electrode, over the edge trace, and backside contact pad.

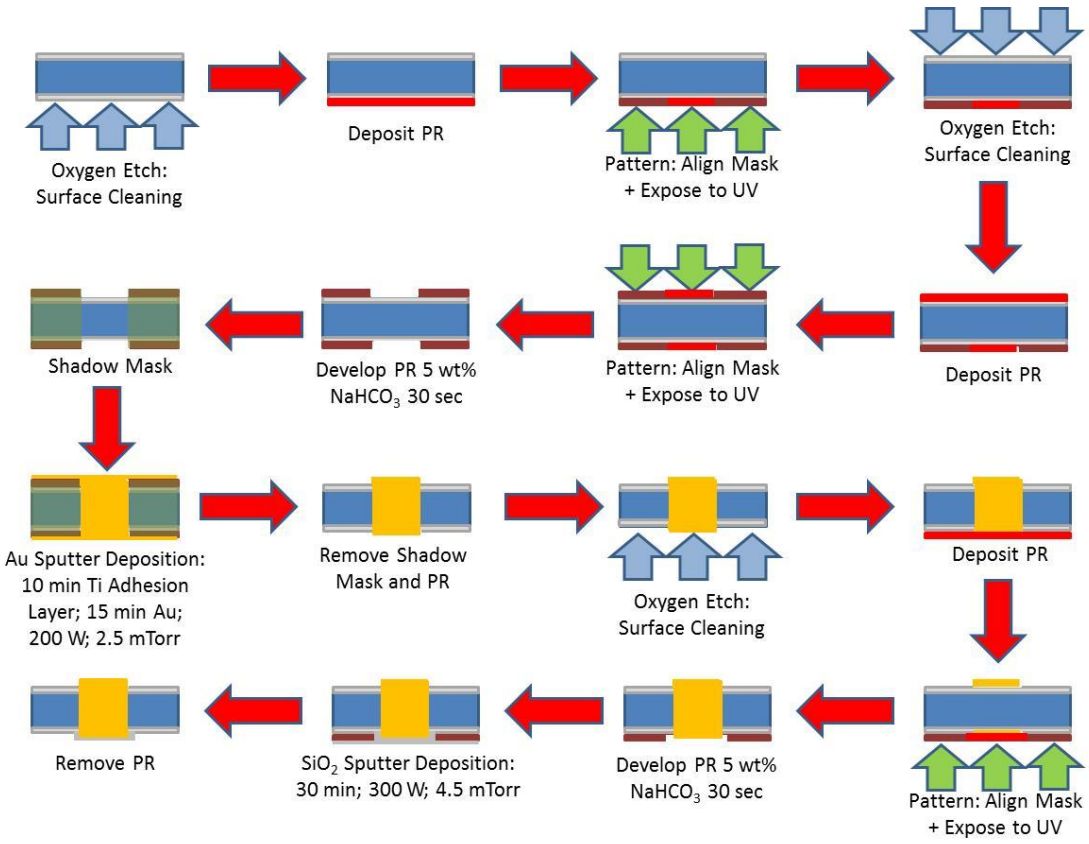

Figure 2.6. Flow diagram outlining the steps in the WAP approach.

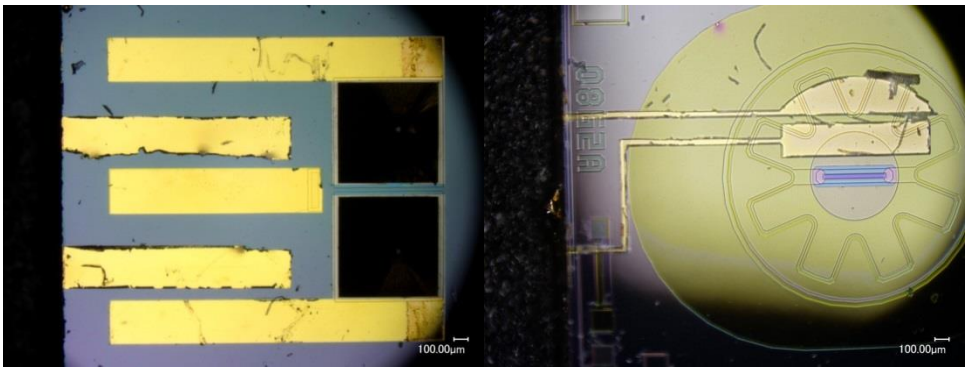

Figure 2.7. Photomicrograph of the end result of the WAP approach with both the anode and cathode deposited on the topside of the ISFET.

2.2.3 Results & Discussion: The main challenges with the WAP approach were preventing the electrodes from shorting to the body of the device and protecting the gold interconnect from erosion by the o-ring seal. RF-sputtered SiO_2 appeared to have insufficient electrical insulating properties for isolating the electrode from the substrate of the ISFET and in later iterations of the WAP approach SiO_2 was deposited by plasma enhanced chemical vapor deposition (PECVD) on the edge of the ISFET prior to patterning and electrode deposition. The high temperatures required for PECVD did not allow the use of photoresist. This created problems with damage to the SiO_2 film during the patterning process utilized prior to electrode deposition leading to shorting the trace to the substrate of the ISFET.

2.3 Thread-Through Processing (TTP) approach for electrode contacts

2.3.1 Introduction: Due to the complexity of steps and complications involved in both THP and WAP approaches, a new method was developed which alleviated the problem of shorting the electrode to the substrate of the ISFET. The thread-through

processing (TTP) approach involves deposition of the electrode on the topside of the ISFET followed by threading a wire gold-bonded to a contact pad on the topside of the ISFET into the interior of the sensor housing to the electronics. Two processing techniques were used to deposit the electrode on the ISFET surface.

2.3.2 Methods: The first technique used photolithography in a similar fashion to that described previously for THP and WAP. The ISFET topside surface was cleaned by oxygen etching followed by patterning using photolithography. Ti was first deposited as an adhesion layer followed by Pt. As explained in Chapter 1, it was determined that Au could not be used as an electrode material as it dissolves in the presence of certain ions including Cl^- (Figure 2.8) [*Cherevko et al.*, 2013]. Pt was determined to be a suitable electrode material. The photoresist was removed leaving behind a platinum electrode with bonding pad on the topside of the ISFET.

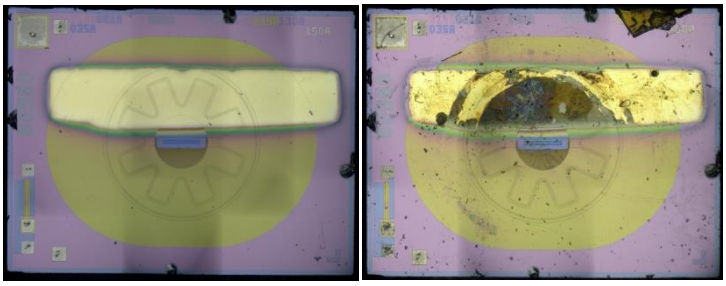

Figure 2.8. Modified ISFET with gold before any titrations (left) and after less than an hour of titrations (right). The gold visually disappeared.

The second processing technique, outlined in Chapter 1, uses a mechanical mask rather than photolithography and is outlined in the flow diagram in Figure 2.9. The ISFET was inserted into the mechanical mask device and aligned to expose a rectangular region 100-150 μm from the gate (see Figure 1.4 and Figure 2.10). The

exposed surface was then cleaned by oxygen etching. A 2.5 µm insulating layer of SiO_2 was deposited on the exposed region of the ISFET using PECVD. 100 nm of Ti was next deposited and exposed to atmosphere to form an insulating layer of TiO_2. An additional 100 nm of Ti was deposited as an adhesion layer followed by 200 nm of Pt. The ISFET was then removed from the mechanical mask and annealed at 350 ˚C for 3 minutes.

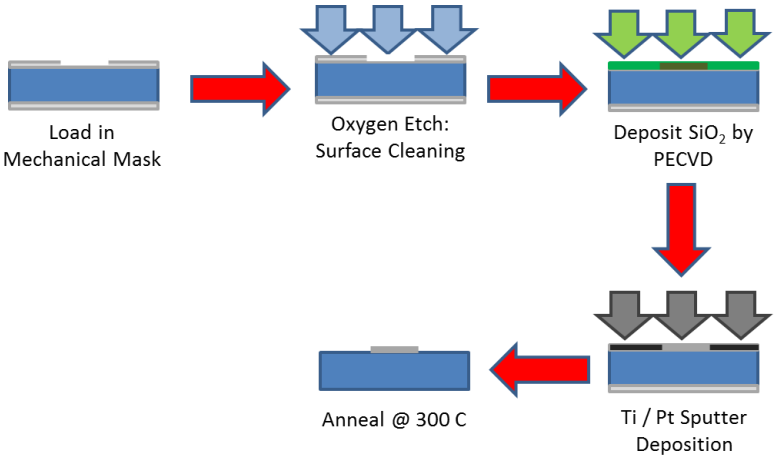

Figure 2.9. Flow diagram outlining the steps for modifying the ISFET used in the TTP approach.

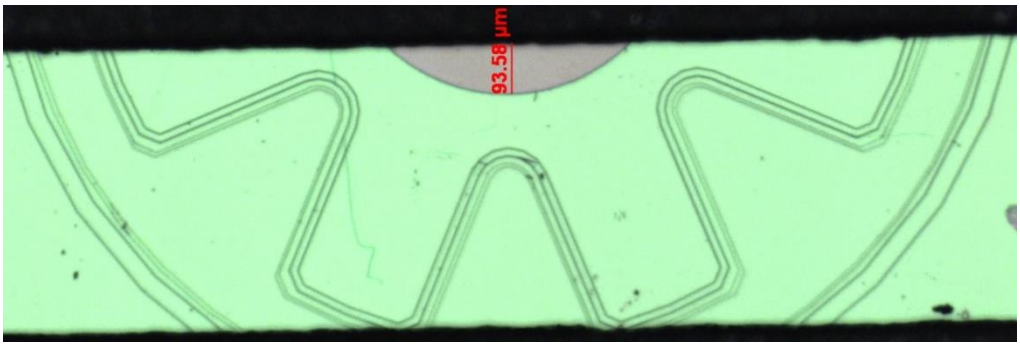

Figure 2.10. Alignment of the ISFET in the mechanical mask device. Exposing 80-90 µm of the purple region (half circle at top center) corresponds to approximately 100 µm distance between the deposited electrode and gate of the ISFET.

2.3.3 Results & Discussion: The primary difference in the TTP approach is that a method has been developed to make electrical contact to an electrode on the top side of the ISFET (Figure 2.11), without exposing the contacts to the test solution, and retaining the proven mechanical seal that has been demonstrated to provide a robust and long-lived sensor lifetime. Photolithography is the standard technique for depositing an electrode for achieving precise control over dimension and alignment of the electrode. Unfortunately, photolithography could not be used with PECVD due to high temperature requirements. The mechanical mask method has proven to yield operational sensors, however there is significantly less control over the shape of edges of the electrode and distance from the gate primarily due to "creep". This method is also not scalable to bulk production. Much effort was spent in determining the proper assembly of the ISFET in the mechanical stage in order to achieve ~100 um spacing +/-10 μm between the anode-gate. When using a mechanical mask, creep becomes a serious issue during deposition of the electrode materials so the mask needs to be offset and uniformly pressed down. As a result this process was found to generate functional sensors but remains difficult to reproduce identical sensors and is likely somewhat operator dependent.

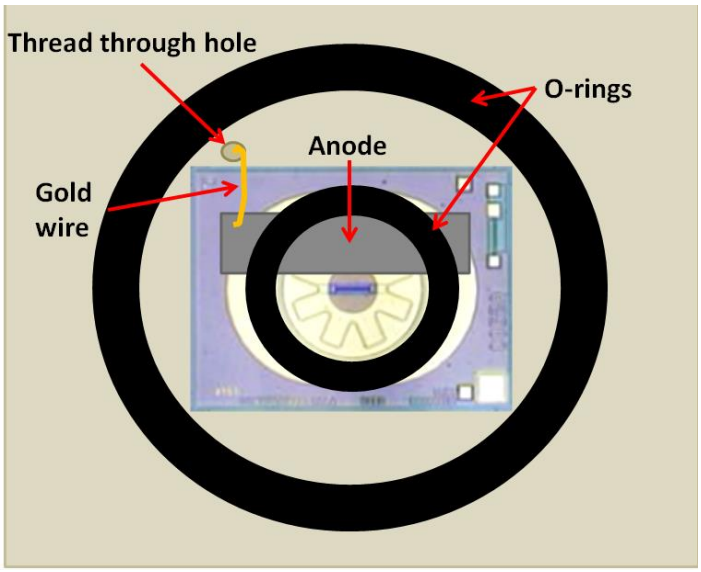

Figure 2.11. Depiction of the TTP method for making electrical connection between the anode on the topside of the ISFET to the internal circuitry. The background material containing the thread-through hole is the PEEK support of the sensor housing. Top sealing plate not shown.

3 Electrical isolation

Tests using the prototype sensor electronics indicated that a leakage current was interfering with the ISFET pH measurement (see Figure 2.27). There are several features on the topside of the ISFET that may provide a path of leakage current to the chip's substrate so much care was taken to avoid overlap when positioning the electrode. In order to test our ability to add an electrically isolated electrode to the ISFET, test electrodes were deposited on "dummy chips" as seen in Figure 2.12. The dummy chips are then tested on a standard probe station for resistance between the electrodes (Figure 2.12– left), on the same electrode (Figure 2.12– middle), and on the substrate (Figure 2.12– right). It has been confirmed that, with a sufficiently thick

(microns) layer of SiO_2 the electrodes can be effectively isolated from each other by tens to hundreds of giga-ohms.

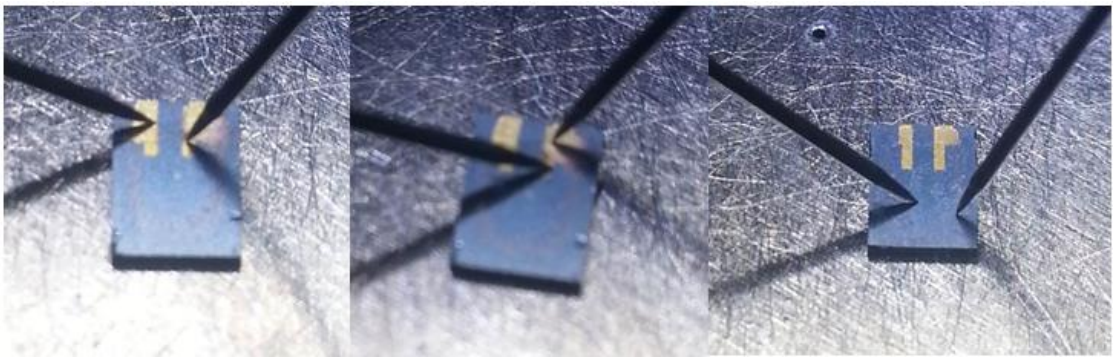

Figure 2.12. Electrical isolation testing with ‘dummy’ Si chips.

The deposition of electronically insulating SiO_2 was fine-tuned using PECVD. Figure 2.13 shows the voltammograms corresponding to the position of the probes in Figure 2.12 for the PECVD method of depositing SiO_2. The resistance remains in the 10’s to 100’s of giga-ohms over the range of 1-10 V between the two electrodes. In comparison, in Figure 2.14, approximately the same thickness of SiO_2 (2.5 μm) was deposited by RF sputtering and only 10’s of mega-ohm resistance between the two electrodes was achieved which was insufficient for isolating the anode from the substrate of the ISFET.

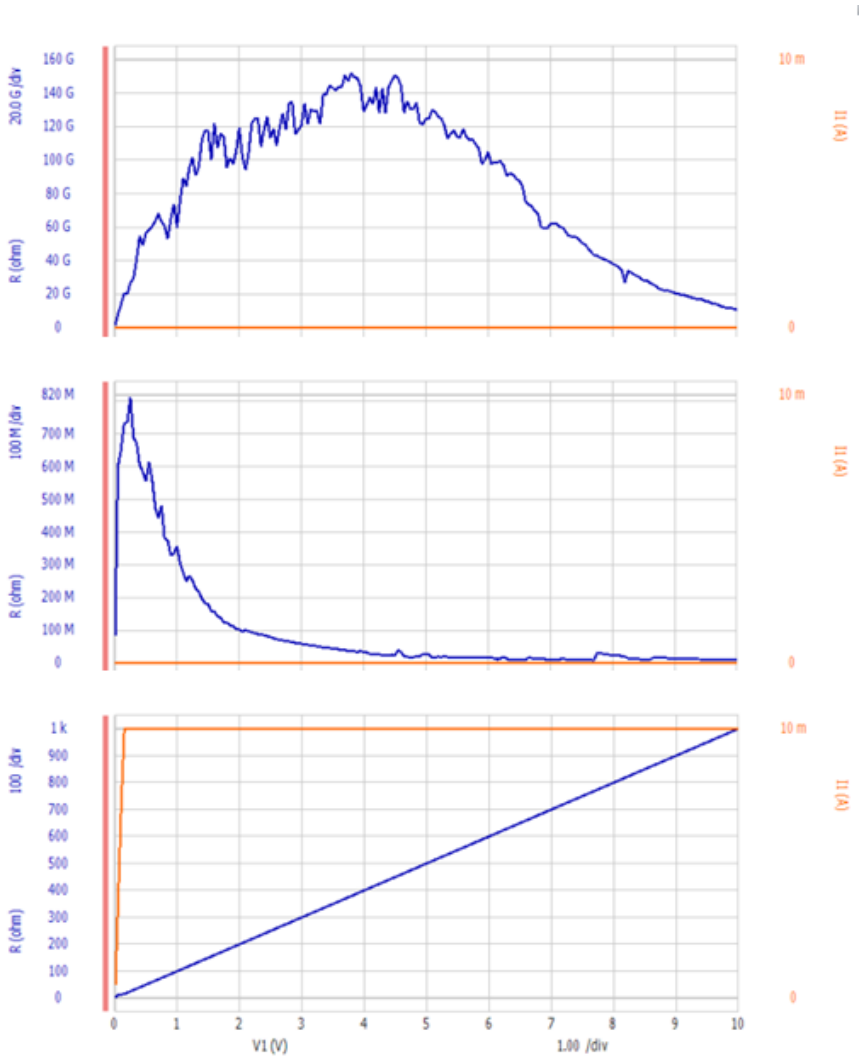

Figure 2.13. Voltammograms of Si chips with electrodes deposited with an insulating layer of PECVD SiO_2 for assessing the insulating properties of the SiO_2 film.

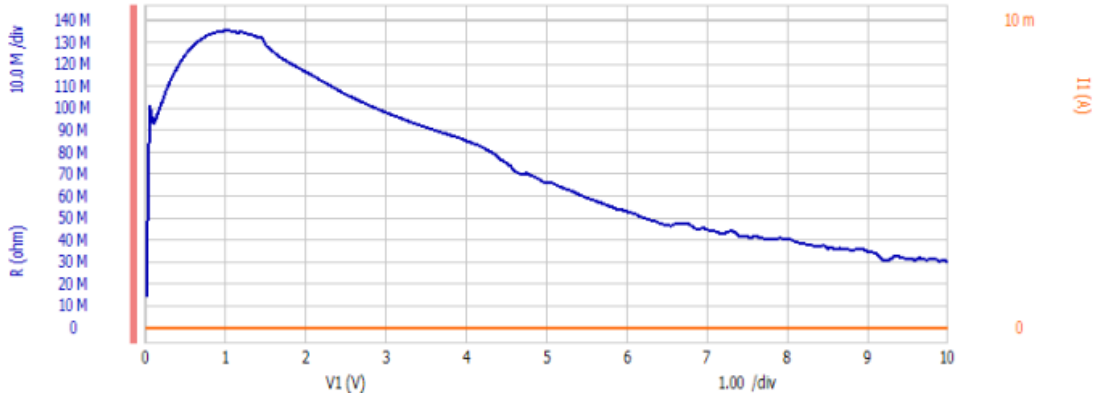

Figure 2.14. Greater than 2.5 μm of RF sputtered SiO_2 resulted in mega-ohm resistance compared to the giga-ohm resistance achieved by PECVD deposited SiO_2.

While the requirement for electrical isolation is clear, the minimum resistance required between electrode and ISFET substrate is likely a function of the titration anode voltage required to achieve the prescribed titration current. This realization is important because it demonstrates that careful control and monitoring of the titration circuit is essential in order to achieve good results and avoid damaging the sensor.

4 Encapsulation

4.1 Preliminary Housing

The housing used in the commercial Durafet sensor cannot be used to encapsulate modified chips due to the complexity of assembly and limited number of chip contact relays available. It was therefore necessary to design a simple PCB with additional relays and a compatible waterproof housing. The sensor housing designed to encapsulate the modified ISFET chips in the preliminary analysis is shown in Figure 2.15. Chip encapsulation is necessary in order to isolate the backside electrical

contacts of the ISFET while allowing topside exposure of the gate to the sample solution. In this design, electrical contacts are made from chip to PCB using gold wire bonding. These connections are passed through a PCB header to a waterproof bulkhead. The ISFET is located on top of the housing lid and sealed with an o-ring. The backside of the ISFET is accessible for bonding through a shallow well machined into the lid.

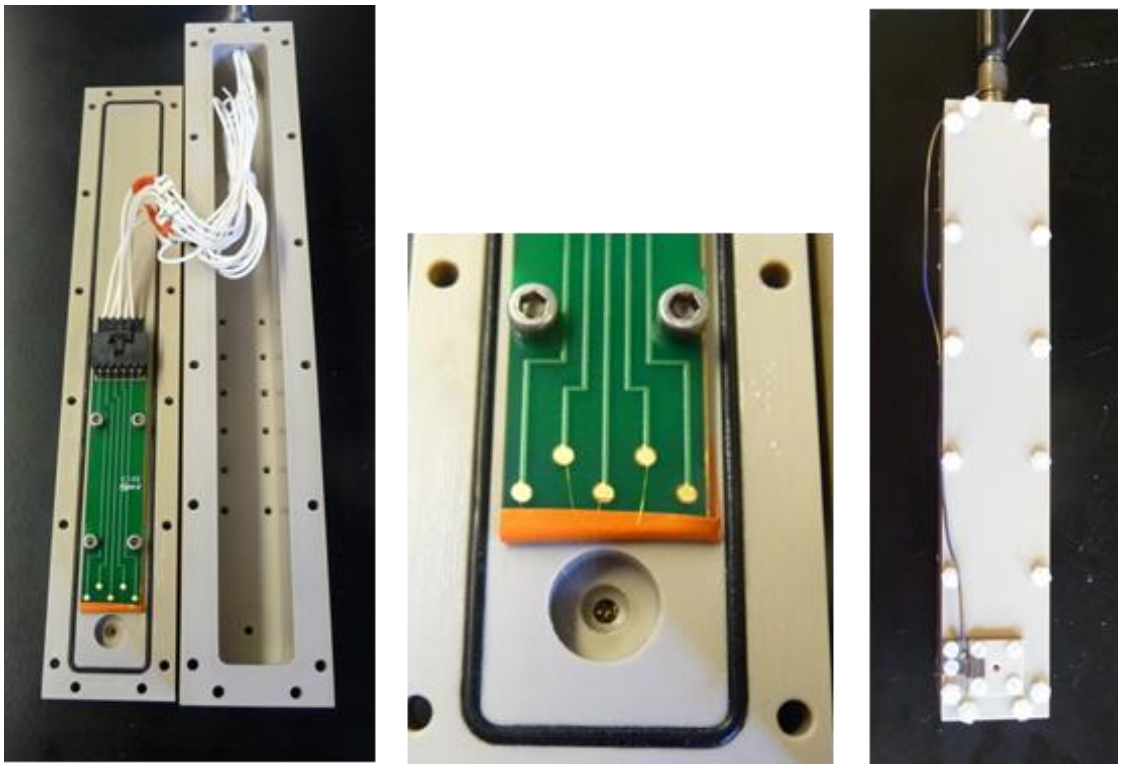

Figure 2.15. Initial housing design to encapsulate the modified ISFET and isolate the internal electronics from the test solution.

Initial testing of the modified housing was carried out using a standard Durafet to provide the pH reference electrode and counter electrode necessary to operate the pH circuitry (see Figure 2.19). The location of the cathode used to operate the titration

circuit is somewhat arbitrary. As a matter of convenience, a cathode integral to the housing was developed as an option for testing chips that do not have an integral topside cathode (Figure 2.15 right). The integral cathode was machined out of stainless steel and coated with Ti. The bulk of the cathode was then passivated by depositing SiO_2 around the base area where the wire is connected, exposing Ti only at the top plane of the ISFET hold down plate.

4.2 Custom Interconnect Housing

A new method of encapsulation was explored which used custom interconnects to make electrical contact between the source, drain, substrate, and topside actuator electrode as shown in Figure 2.16. This housing design resembled the Honeywell Durafet means of making electrical contact through compression. The key benefit of this housing design is that the modified ISFETs could be assembled into the housing without wire-bonding while still using a mechanical seal. A duo of ‘fuzz button’ custom interconnects made electrical connection between the actuator electrode and the internal electronics. Several iterations of lids that utilized the fuzz buttons were 3-D printed and machined. The full sensor housing was redesigned to integrate the reference and counter electrodes and cathode into one streamlined package and the initial iteration was 3-D printed (Figure 2.17). Assembly and design of parts small enough to accommodate the dimensions of the ISFET and actuator electrode proved to be challenging and, due to time constraints and greater simplicity the TTP approach became the primary focus.

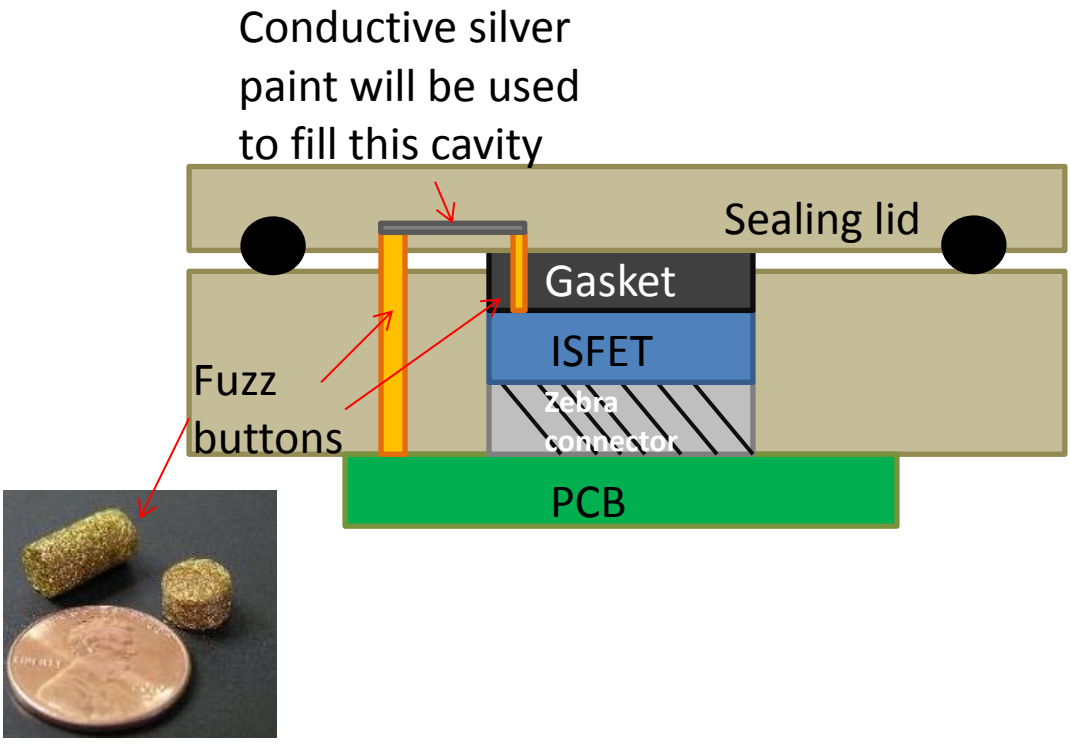

Figure 2.16. Depiction of the special interconnect approach of making electrical connection between the anode on the topside of the ISFET to the internal circuitry.

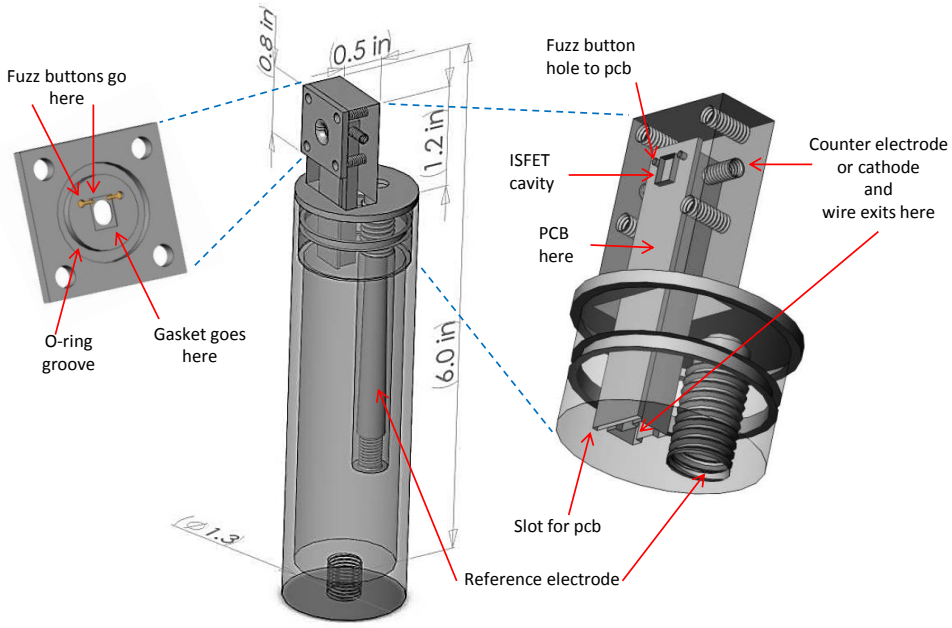

Figure 2.17. 3-D printed housing designed for the special interconnect means of making electrical connection between the anode on the topside of the ISFET to the internal circuitry.

4.3 TTP Simplified Housing

A new housing was designed (see Chapter 1 and Figure 1.5) to simplify assembly for the TTP approach as described in Chapter 1. This housing was modelled after the Honeywell Durafet dimensions to readily enable interface with existing oceanographic, autonomous packages (i.e. SeaFET and SeapHOx).

4.4 Close Proximity Electrode

As an alternative to ISFET back end processing, a radically new design was explored for encapsulating the ISFET which integrates the actuator electrode within the housing and requires no processing of the ISFET chip. The “close proximity electrode” or CPE involves locating an electrode (typically a fine Pt wire) within ~100

μm of the ISFET gate. CPE exhibits several tradeoffs that warrants continued refinement and testing. First, the CPE process is mechanically complex compared to the TTP, because it requires locating a very small wire at a well-defined yet very small distance from the ISFET. A micro-manipulator stage that mounts over the ISFET was developed allowing accurate positioning of the electrode wire (Figure 2.18). The tradeoff of this mechanical complexity is flexibility in the most critical dimension associated with the titration itself: the gate-anode distance.

The CPE device allows for sensor testing to be dramatically expanded to achieve the required resolution of combination of parameters for fine tuning the measurement. For example, examination of the effect of a 20 μm change in anode-gate distance on measurement precision using the TTP would require re-design and re-order of new masks followed by processing new chips in the clean room, in total a process that takes several weeks. In contrast, with the CPE device, this experiment can be carried out by simply turning a micrometer dial and repeating an initial set of measurements. If proven successful, the CPE method can be adapted to hold the Pt electrode at one fixed optimal distance from the gate, greatly simplifying the design and assembly for replicate sensors.

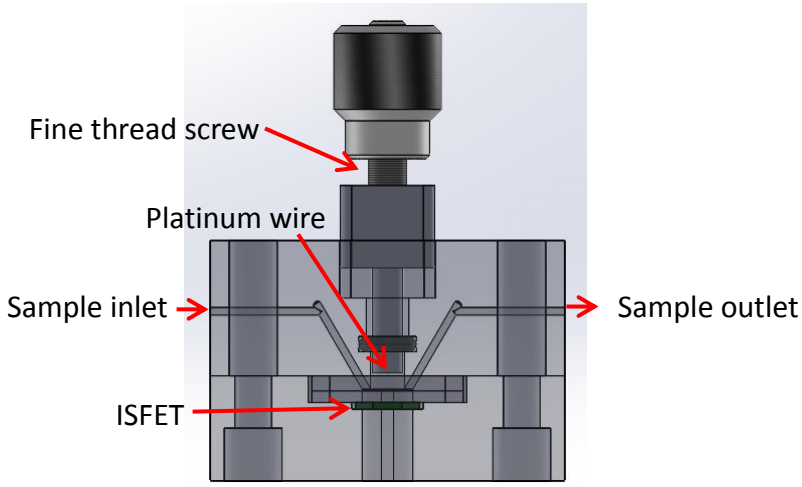

Figure 2.18. CPE device for manual adjustment of the anode distance from the gate of the ISFET.

6 Electronics and Software

The preliminary system setup is shown in Figure 2.19 compared to the revised electronics configuration using the custom ARM microcontroller (TI Cortex TM4C123G) board. As discussed in Chapter 1, a daughter board to the SeapHOx ARM board was developed to operate the actuator electrode, record diagnostic currents, and power and communicate with all the sensor components (Figure 2.20 - Figure 2.26). Standalone electronics and embedded software were developed to provide the groundwork for enabling field deployment and integration with autonomous platforms. Software was written in C/C++ using Code Composer Studio providing a familiar user interface to those already using the SeaFET and SeapHOx sensors. Titration data was processed in Matlab as described in Section 2.3 of Chapter 1. The diagnostic outputs are an additional feature to the circuitry that can also be applied to a standard Honeywell Durafet (Figure 2.25).

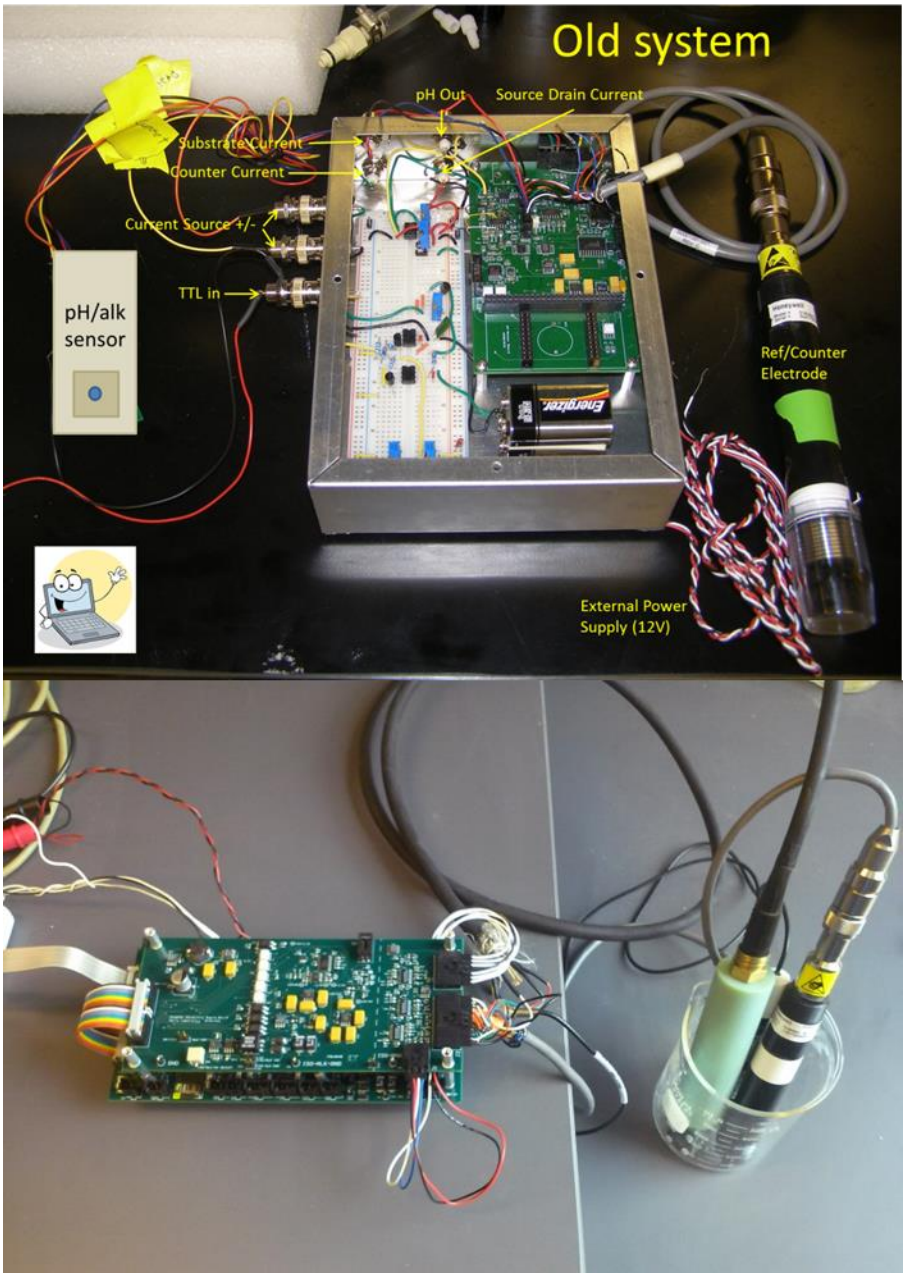

Figure 2.19. Initial prototype electronics utilizing a breadboard to deliver the actuating current (top) and the ARM board (bottom) which removes the computer interface and enables integration with autonomous platforms.

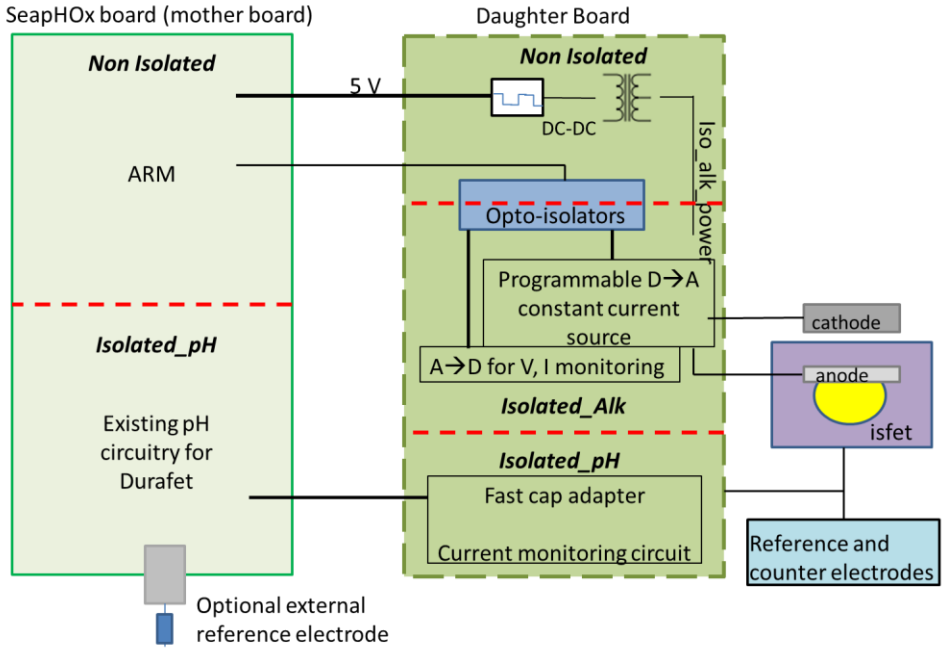

Figure 2.20. Schematic of the daughter board components that interfaces with the SeapHOx ARM board.

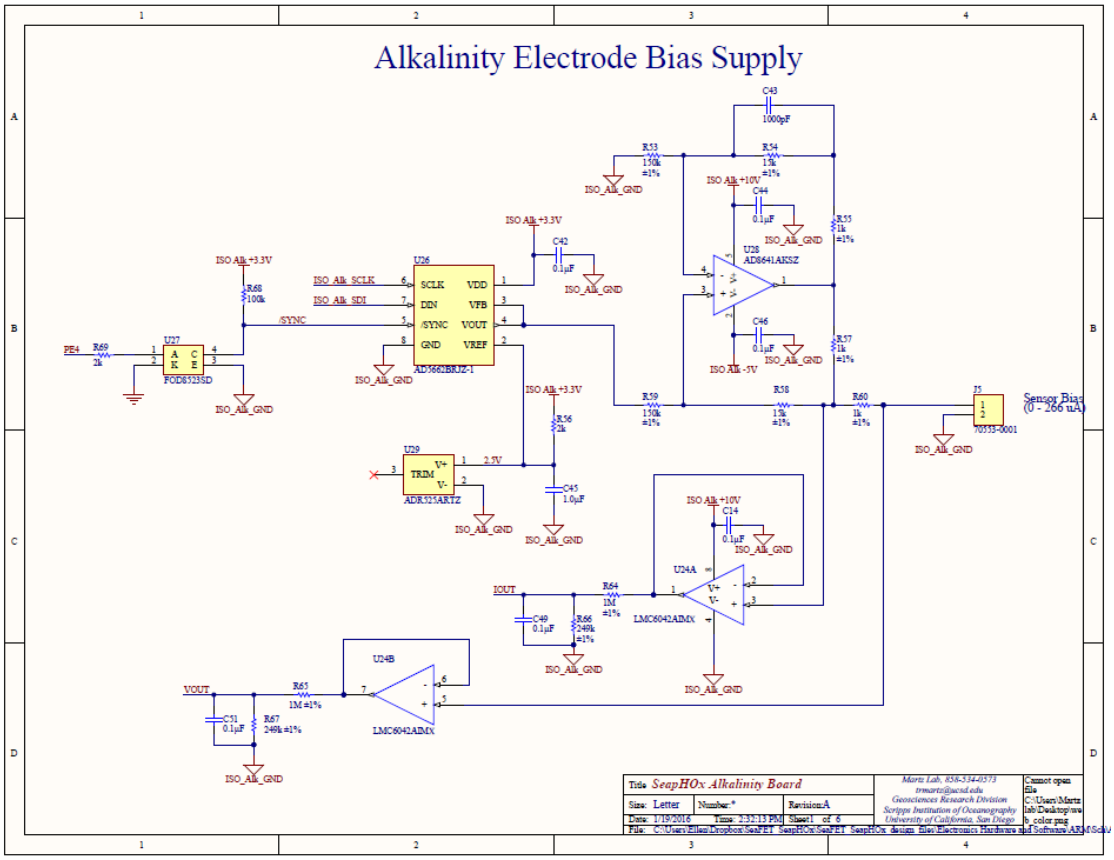

Figure 2.21. Circuitry for programmable control of the constant current for operating the actuator electrode.

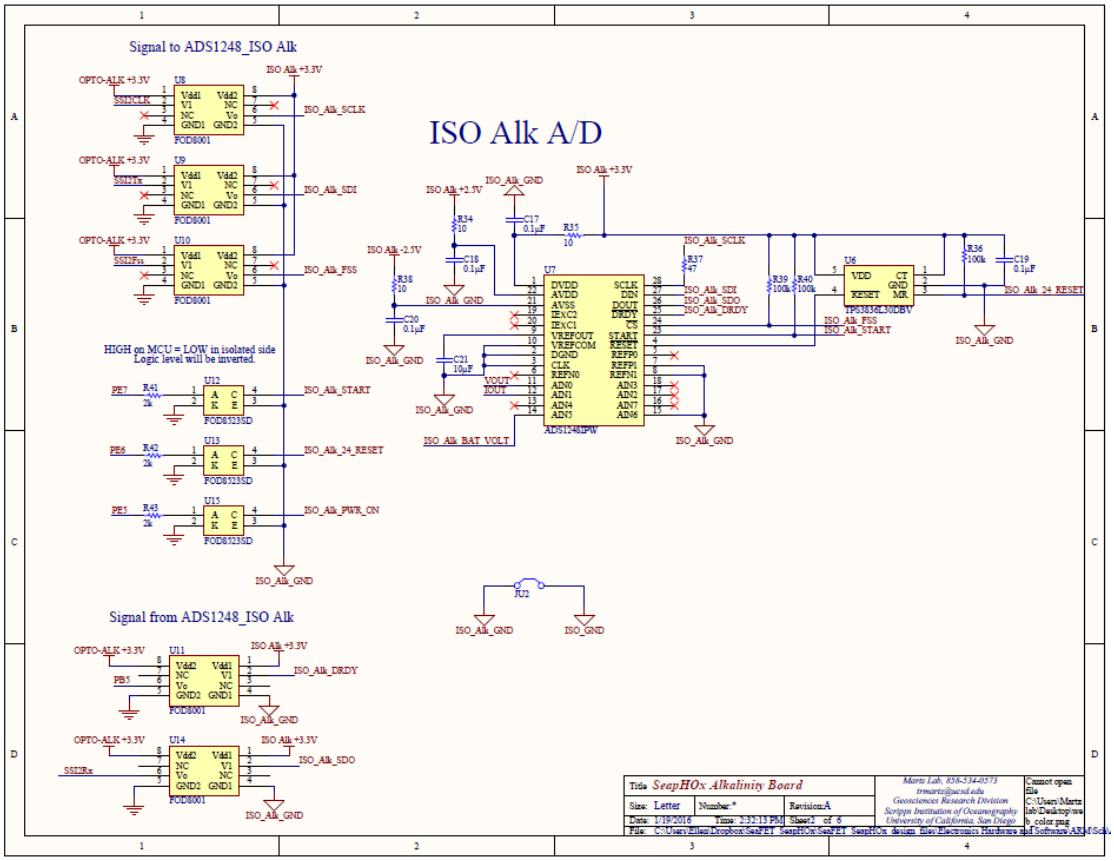

Figure 2.22. Isolated A/D for the daughter board.

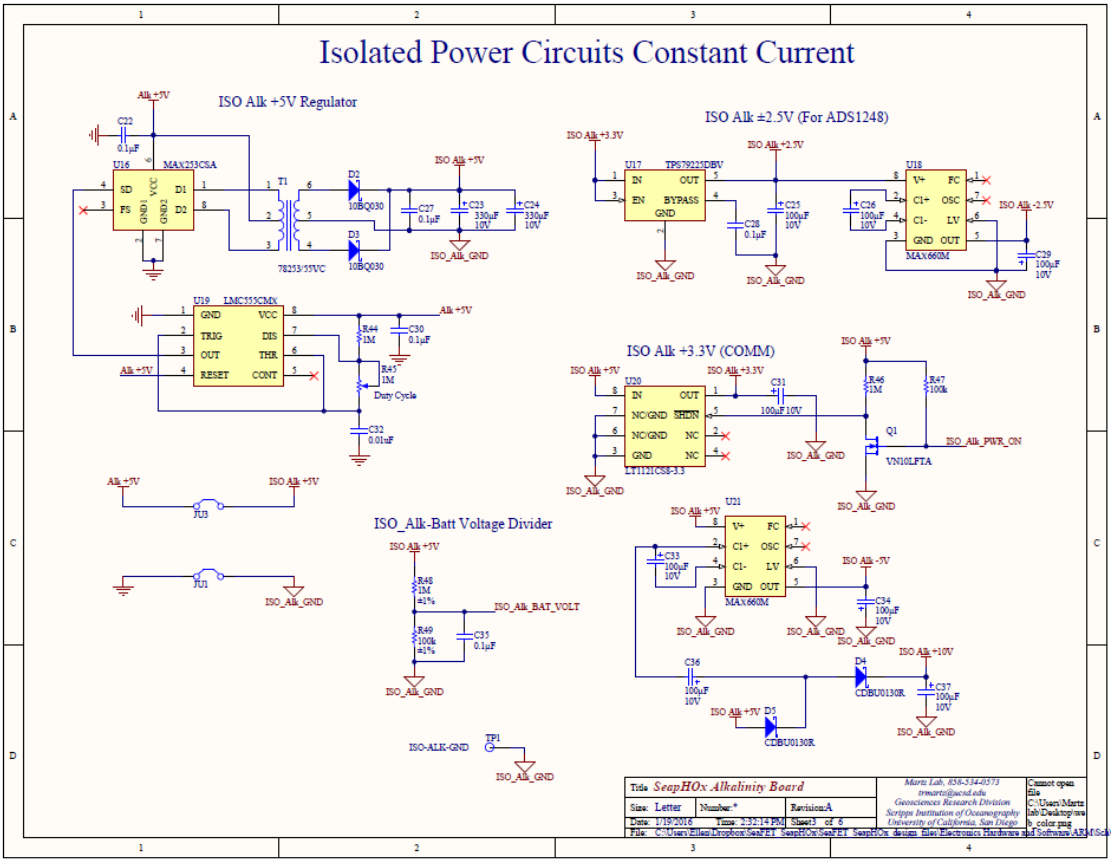

Figure 2.23. Circuitry for supplying isolated power to deliver the constant current to the actuator electrode.

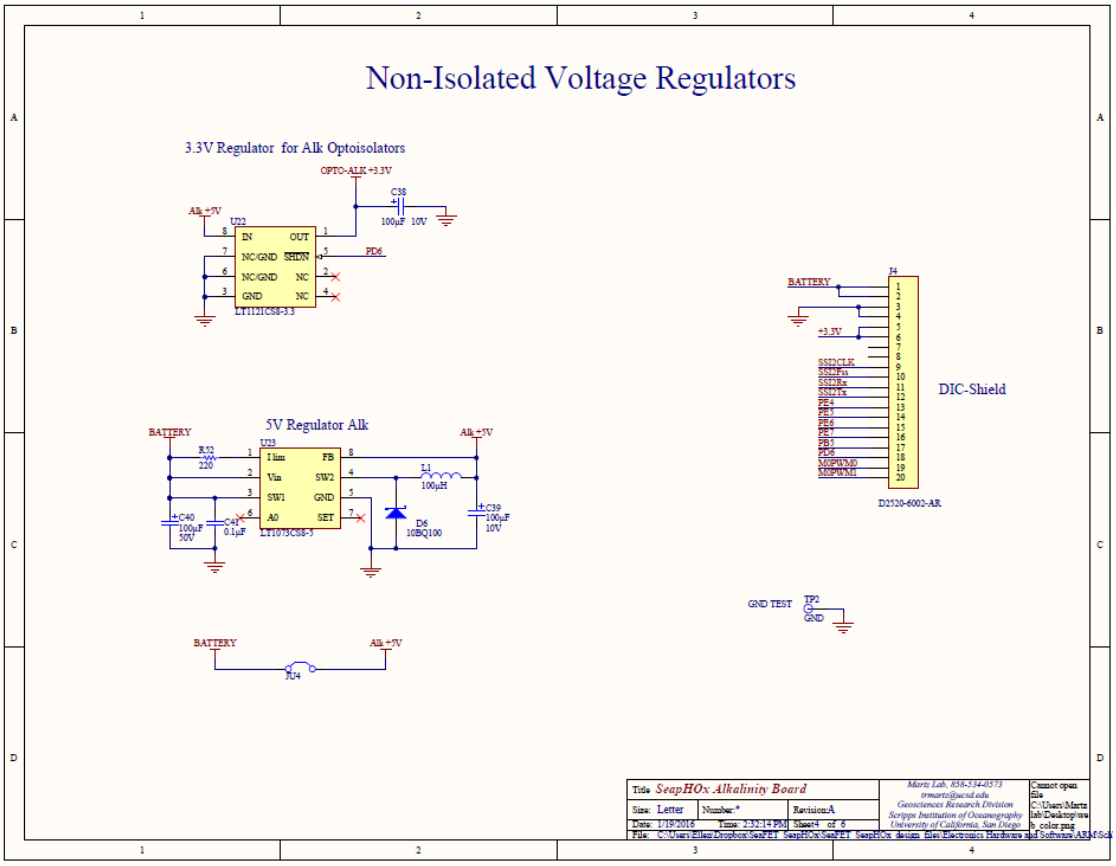

Figure 2.24. Voltage regulators for the daughter board.

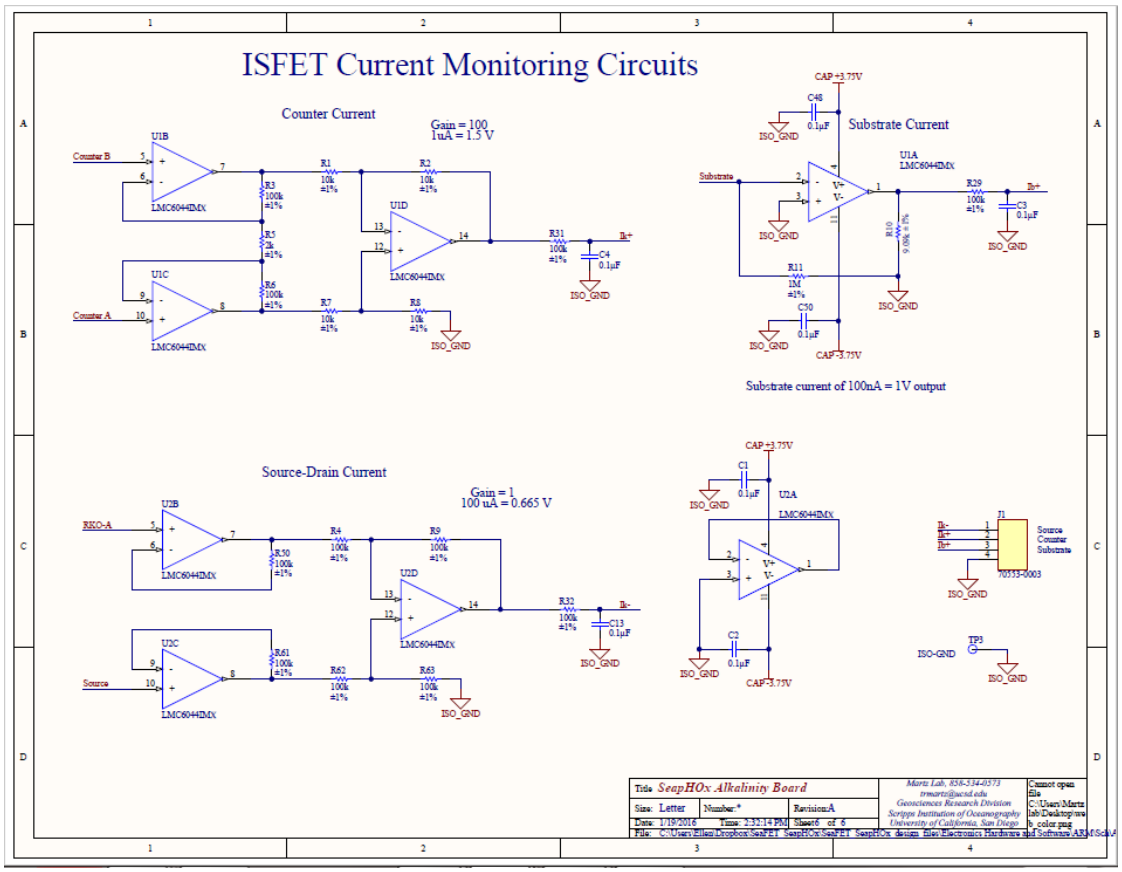

Figure 2.25. Monitoring circuitry for measuring leakage currents and ISFET operating point.

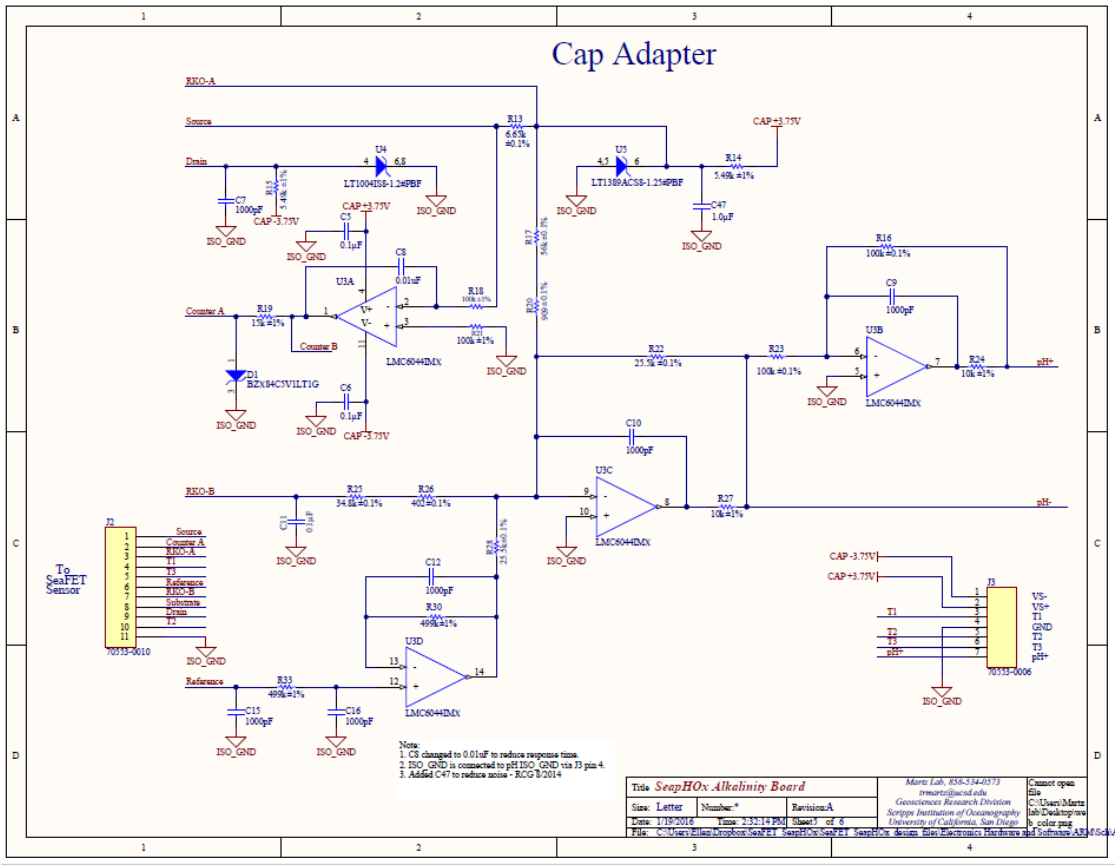

Figure 2.26. Proprietary Honeywell ISFET operating circuit, modified to increase response time of the ISFET for capturing the titration curve during the A_T measurement.

Recording diagnostic leakage currents and all operating voltages and corresponding currents became an important tool for assessing sensor performance. When observing the full set of diagnostics, it became clear when the sensor was malfunctioning as shown in Figure 2.27. All of the modification processes explored did not provide reproducible results so each modified ISFET came with new distinct problems. The current source is designed to be constant so V_A rises or falls to maintain this current and is somewhat unique to each modified ISFET. When V_A approaches

and exceeds 2.0 V, bubbles start to form on the anode surface. After subsequent titrations, V_A no longer approaches zero when the current is programmed to return to zero. Measured I_A does in fact reach zero so there is some capacitive effect where charge does not immediately discharge and V_A remains closer to 1 V (Figure 2.28). The max V_A continues to slowly rise with continuing titrations. Work is ongoing to integrate a relay into the actuating circuit to reset V_A to zero after each titration. Initial attempts at integrating relays resulted in severe spikes in V_{RS} in addition to diagnostic currents. Maximum V_A as well as side reactions and unwanted byproducts are ultimately a function of electrode material. Pt has served as a reliable electrode material during the prototype phase of sensor development; however, other electrode materials such as iridium oxide and other deposition techniques can be utilized to optimize sensor performance by reducing side reactions and expanding the acceptable range of $V_{A.}$

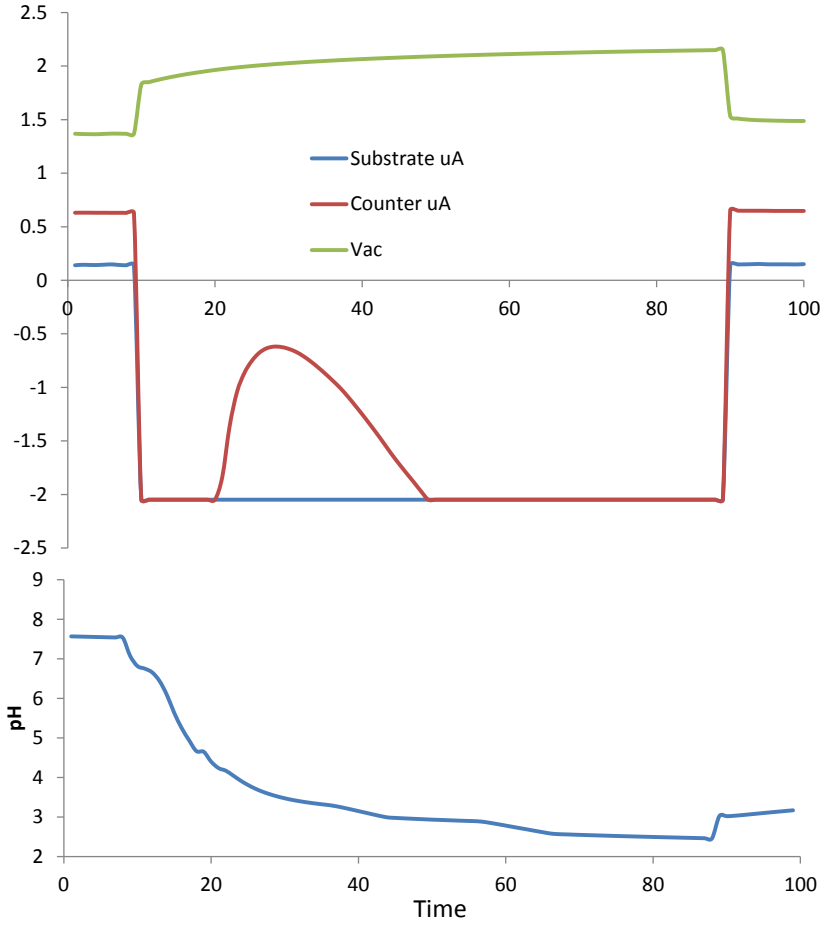

Figure 2.27. Example of diagnostic measurements when the anode interferes with ISFET integrity. The leakage currents (top) exceed the measureable range of the electronics.

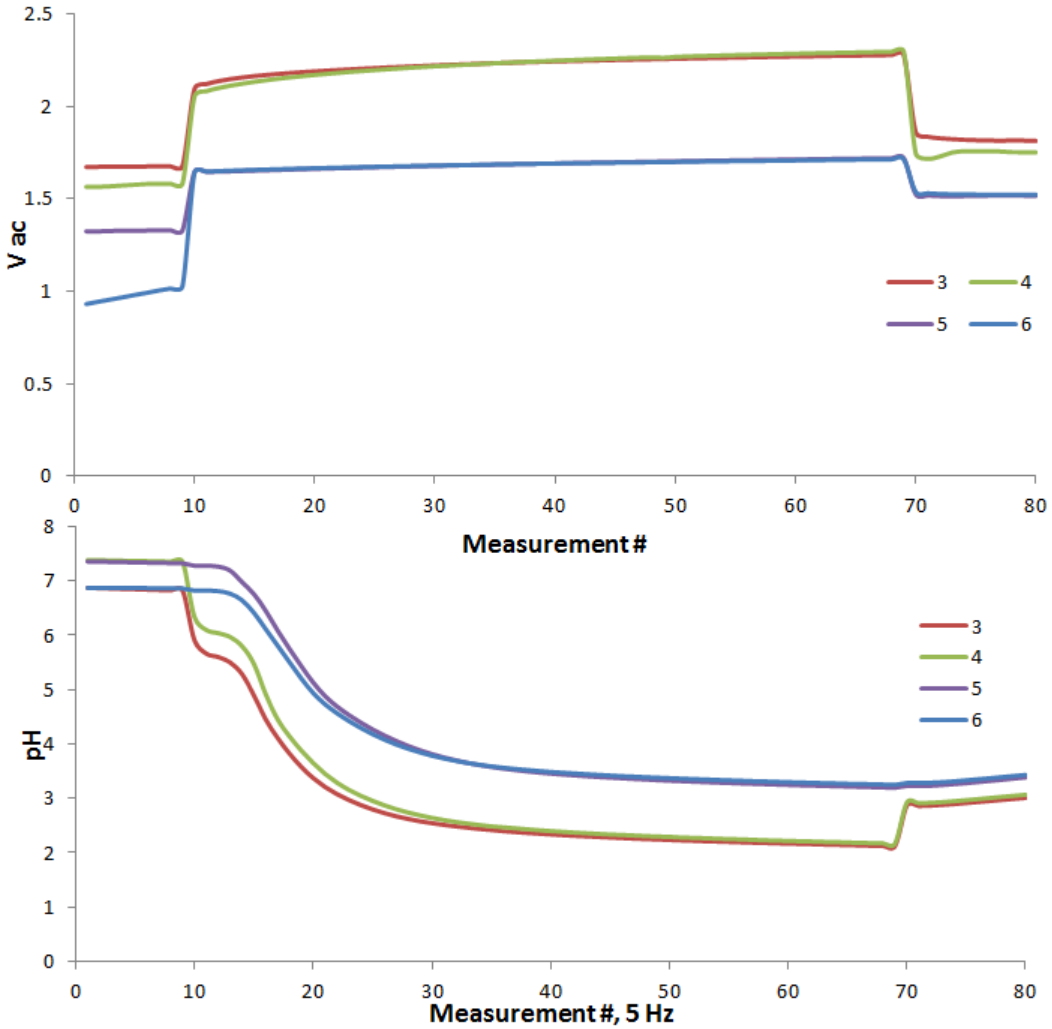

Figure 2.28. Example of when V_A exceeds 2V (top) and resulting shift in pH curve (bottom). Max V_A corresponds to the starting V_A prior to turning the actuating current on. Numbers correspond to successive titrations. The anode was shorted to ground for titrations 5 and 6 demonstrating how the reduced V_A impacts the resultant titration curve compared to titrations 3 and 4.

Another interesting phenomenon is that there is a jump in leakage currents when the modified ISFET is pulled out of solution while leaving all other electrodes untouched. By removing the counter electrode from the solution briefly, the leakage currents return to acceptable values upon return to solution. This is a very repeatable

exercise that does not yet have an explanation. However, sometimes when the leakage currents exceed accepted values, removing the sensor components and replacing them in this order resets the system to acceptable values.

7 Preliminary Field Testing

The prototype sensor described in Chapter 1 was integrated into a SeapHOx housing (Figure 2.29) in order to begin field testing the sensor. In some ways, in situ testing presents fewer challenges than bench top testing due to the logistics of sample introduction. For in situ testing, a simple pump refreshes the sample at the surface of the ISFET, whereas benchtop tests typically require rinsing and drying of the sensor components in between samples. The first in situ deployment was carried out in the test tank at Scripps Institution of Oceanography (Figure 2.30). The chemistry of the test tank was altered by first raising the A_T from approximately 2250 μmol kg^{-1} to 2450 μmol kg^{-1} by adding a concentrated solution of HCO_3^- and CO_3^{2-} over the course of roughly 4 hours. The A_T was then reduced by adding 1N HCl at the same time intervals to try to return to approximately the starting A_T.

As shown in Figure 2.31, the time it took to reach the endpoint of the titration increased with increasing A_T and decreased in decreasing A_T. The sensor was operated in continuous mode and at each point in Figure 2.31 10 points were averaged. There appeared to be a downward drift as time continued after perturbing the chemistry of the test tank. Unfortunately no bottle samples were measured so it is unclear if this is a real signal or drift. This particular modified ISFET had a non-Nernstian response and

this was more of a test run so the plan is to repeat this experiment with a better functioning ISFET. From a qualitative standpoint these results are promising.

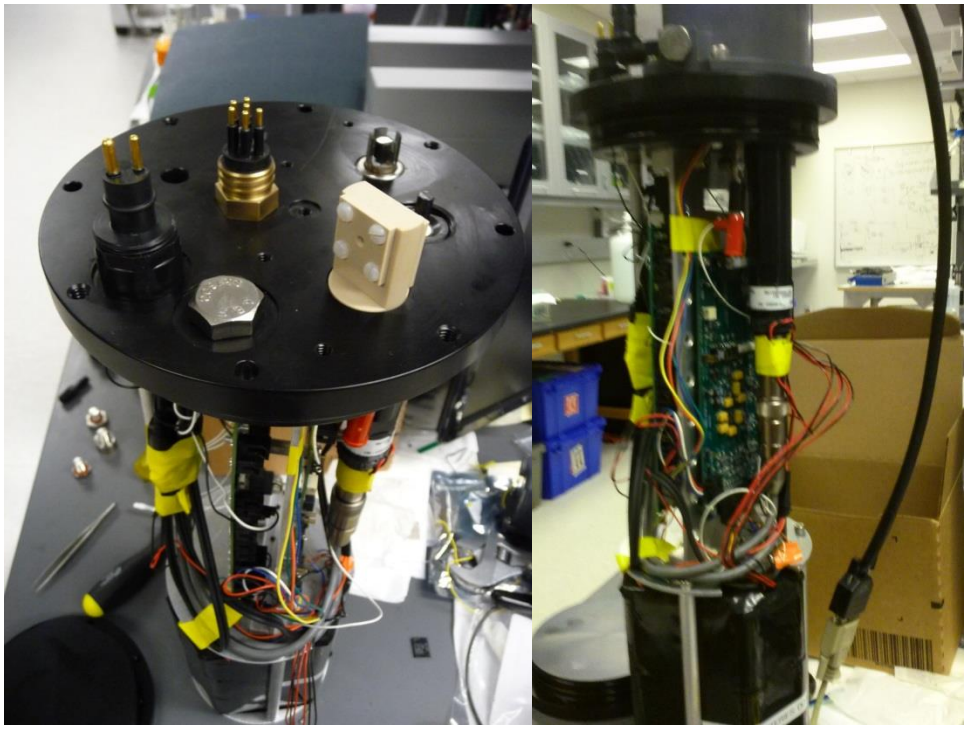

Figure 2.29. SeapHOx housing adapted to integrate the modified ISFET, reference and counter electrodes, cathode, and daughter board.

Figure 2.30. Preliminary test tank deployment with autonomous sensor package.

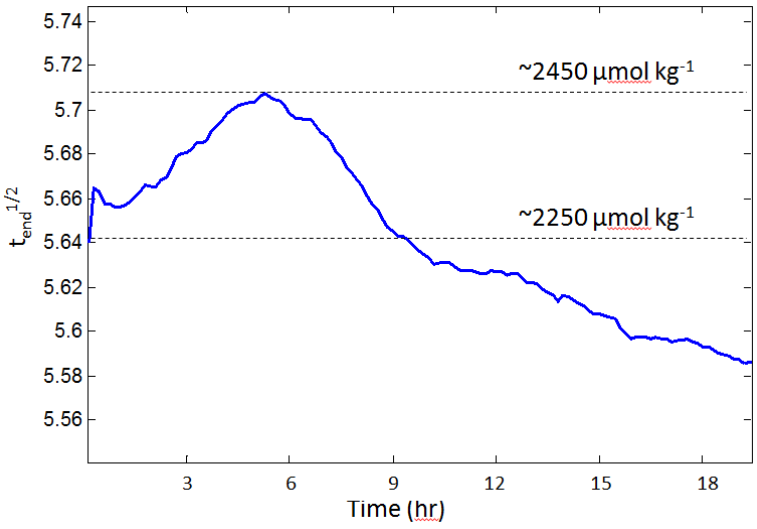

Figure 2.31. Sensor output for preliminary test tank experiment. The starting A_T was approximately 2250 µmol kg^{-1} and a concentrated solution of $NaCO_3$ was added at hourly intervals with a target A_T of 2450 µmol kg^{-1}. HCl was then added to reduce the A_T close to the starting value.

8 Summary and Conclusions

Several processes and designs were explored to modify a fully functional ISFET and encapsulate the sensor which ultimately led to the successful methods described in Chapter 1. A microscale, highly insulating coulometric actuator device was integrated with an ISFET, enabling a nL-scale acid-base titration on a single ISFET chip. Multiple photomask designs were developed for photolithography. Additional increases in stability and sensitivity can be achieved by optimizing the sensor, including: location of the actuator electrode with respect to the gate, current density, and electrode material. We confirmed, as did others before us, that robust ISFET encapsulation is not trivial and presents a major challenge in terms of both experimental reproducibility and production scalability [*Oelßner et al.*, 2005]. New methods are being explored to integrate the actuator electrode into the sensor housing rather than physically depositing the electrode on the surface of the ISFET which would remove the direct modification of the ISFET and simplify sensor assembly. Field testing of the current sensor configuration will be achievable after further assessment of sensor calibration and proton generation efficiency over a range of temperature and pressure.

Acknowledgements

This work was supported by grant NSF OCE Award 1155122. This material is also based upon work supported by the National Science Foundation Graduate Research Fellowship under Grant No. DGE-1144086. I would like to acknowledge

Bob Carlson and Jim Connery from Honeywell for providing a great deal of useful guidance during the development of this sensor.

References

Baxter, R. D. (1985). ISFET sensor and method of manufacture, in *U.S. Patent 4505799 A*, General Signal Corp.

Bergveld, P. (2003), Thirty years of ISFETOLOGY: What happened in the past 30 years and what may happen in the next 30 years, *Sensors and Actuators B: Chemical*, *88*(1), 1-20, doi:http://dx.doi.org/10.1016/S0925-4005(02)00301-5.

Cherevko, S., A. A. Topalov, A. R. Zeradjanin, I. Katsounaros, and K. J. J. Mayrhofer (2013), Gold dissolution: towards understanding of noble metal corrosion, *RSC Advances*, *3*(37), 16516, doi:10.1039/c3ra42684j.

Johnson, K. S., H. W. Jannasch, L. J. Coletti, V. A. Elrod, T. R. Martz, Y. Takeshita, R. J. Carlson, and J. G. Connery (2016), Deep-Sea DuraFET: A Pressure Tolerant pH Sensor Designed for Global Sensor Networks, *Analytical chemistry*, *88*(6), 3249-3256, doi:10.1021/acs.analchem.5b04653.

Oelßner, W., J. Zosel, U. Guth, T. Pechstein, W. Babel, J. G. Connery, C. Demuth, M. Grote Gansey, and J. B. Verburg (2005), Encapsulation of ISFET sensor chips, *Sensors and Actuators B: Chemical*, *105*(1), 104-117, doi:10.1016/j.snb.2004.05.009.

Olthuis, W., J. Luo, B. H. Van der Schoot, P. Bergveld, M. Bos, and W. E. Van der Linden (1990), Modelling of non-steady-state concentration profiles at ISFET-based coulometric sensor—actuator systems, *Analytica Chimica Acta*, *229*(0), 71-81, doi:http://dx.doi.org/10.1016/S0003-2670(00)85111-9.

Van der Schoot, B., P. Van der Wal, N. de Rooij, and S. West (2005), Titration-on-a-chip, chemical sensor–actuator systems from idea to commercial product, *Sensors and Actuators B: Chemical*, *105*(1), 88-95, doi:http://dx.doi.org/10.1016/j.snb.2004.02.058.

CHAPTER 3: PHYSICAL AND BIOLOGICAL DRIVERS OF BIOGEOCHEMICAL TRACERS WITHIN THE SEASONAL ICE ZONE OF THE SOUTHERN OCEAN FROM PROFILING FLOATS

Abstract

Here we present initial findings from nine profiling floats equipped with pH, O_2, NO_3^-, and other biogeochemical sensors that were deployed in the seasonal ice zone (SIZ) of the Southern Ocean in early 2014 and 2015 through the Southern Ocean Carbon and Climate Observations and Modelling (SOCCOM) project. During the period of ice cover, clear respiration signals were evident when gas exchange was inhibited. C:N:O elemental ratios were determined to be near Redfieldian for most of the floats when under ice in the SIZ. A large springtime phytoplankton bloom was observed that coincided with ice melt. For one of the floats, in the absence of ice edge dynamics in the second year (i.e. shoaling of the mixed layer depth, increased vertical stability, and timing of nutrient availability with light throughput as ice melts), a springtime phytoplankton bloom was not observed. A simple model of mixed layer physics was developed to separate the physical component from the biological component of the signal in pH and O_2 for float 5904184 in the SIZ. Net heterotrophy was observed for about half of the year in the SIZ from O_2 data as well as derived Dissolved Inorganic Carbon. Seasonal net community production depleted up to 5 mol C m^{-2} during the ice free period but was nearly balanced by the strong respiration signal during the under ice period of the year.

1 Introduction

Ice cover has strong influence over gas exchange, vertical stability, and biological production, which are critical to understanding the Southern Ocean's central role in oceanic biogeochemical cycling, heat, and carbon uptake under a changing climate [*Delille et al.*, 2014; *Majkut et al.*, 2014]. For example, the Southern Ocean is responsible for up to 50% of the ocean's uptake of human induced CO_2 emissions [*Khatiwala et al.*, 2009; *Majkut et al.*, 2014; *Sabine et al.*, 2004]. The upper ocean carbon cycle is governed by a combination of physical and biological processes. Additionally, in regions of sea ice cover, CO_2 uptake can also be driven by brine rejection during ice formation through the sinking of carbon rich brine, gas exchange can be inhibited during ice cover, CO_2 depleted ice melt enhances gas exchange, and ice enhanced biological production may increase CO_2 uptake [*Delille et al.*, 2014; *Rysgaard et al.*, 2011]. However, the relative influence of physical versus biological processes in this hard-to-study region is poorly understood due to limited observations particularly in the seasonal ice zone where substantial biological activity is known to occur [*Eveleth et al.*, 2016; *Z Li et al.*, 2016; *Shadwick et al.*, 2014; *Shadwick et al.*, 2015; *Smith and Nelson*, 1986; *Tortell et al.*, 2015].

Large phytoplankton blooms have been observed at ice edges in high latitude regions [*Arrigo and van Dijken*, 2003; 2004]. Ice melt stratifies the upper water column at the ice edge causing the depth of the surface mixed layer to shoal which in turn promotes conditions that trigger a phytoplankton bloom following Sverdrup's hypothesis [*Smith and Nelson*, 1986; *Sverdrup*, 1953]. Other factors affecting the

timing or magnitude of an ice edge phytoplankton bloom include release of iron and nutrients stored in ice upon ice melt [*Lannuzel et al.*, 2016] as well as wind forcing [*Fitch and Moore*, 2007] and thermal convection [*Ferrari et al.*, 2015].

Profiling floats equipped with oxygen and nitrate sensors have been valuable in quantifying marine biogeochemical processes over multi-year timescales [*Bushinsky and Emerson*, 2015; *Hennon et al.*, 2016; *Johnson et al.*, 2010; *Juranek et al.*, 2011; *Martz et al.*, 2008; *Plant et al.*, 2016]. As organic matter is broken down into inorganic matter (remineralization) or inorganic matter is transformed into organics (production), a constant stoichiometry is observed, known as the Redfield ratio, where C:N:O = 106:16:138-150 [*Anderson and Sarmiento*, 1994]. These ratios are derived from the average composition of organic matter and can vary depending on phytoplankton community structure [*Li and Peng*, 2002]. Estimates of Net Primary Production (NPP), Net Community Production (NCP), and Export Production (EP) from O_2 or NO_3^- data rely on these Redfield relationships to convert reported rates into carbon.

Through the Southern Ocean Carbon and Climate Observations and Modelling (SOCCOM) project, approximately 200 profiling floats equipped with O_2, pH, NO_3^-, and bio-optical sensors are being deployed in the Southern Ocean. These "Biogeochemical-Argo" floats provide biogeochemical observations during the austral winter and under sea ice, a region that has been inaccessible with traditional platforms. Here we present analyses from the first set of SOCCOM floats deployed within the seasonal ice zone (SIZ) in the Pacific and Atlantic sectors of the Southern Ocean. The

relative influence of physical (e.g. mixing and air-sea gas exchange) and biological (e.g. production and respiration) drivers of the carbonate system, O_2, and NO_3 within the upper ocean are explored during the phases of ice formation, ice cover, and ice melt over a seasonal cycle. In the first and second parts of the manuscript, profiling float observations are used directly to give a qualitative description of the physical and biological processes that occur through the annual cycle in the seasonal ice zone and to quantify remineralization during the period of full ice cover when biological processes dominate the signal over physical drivers. In the third part, a model is developed to separate the physical from the biological processes over the course of the annual cycle when physical processes cannot be assumed small or negligible.

2 Methods

2.1 BGC-Argo float information and locations

Nine SOCCOM profiling floats deployed in the sea ice zone (SIZ) between March, 2014 and April, 2016, observed at least one full annual cycle within the SIZ of the Southern Ocean (Figure 3.1 and Table 3.1). As shown in Table 3.1, most of these floats were equipped with a Deep-Sea DuraFET pH sensor [*Johnson et al.*, 2016;], Aanderaa oxygen optode [*Johnson et al.*, 2015; *Tengberg et al.*, 2006], ISUS nitrate sensor [*Johnson et al.*, 2013], and other bio-optical sensors including chlorophyll-a fluorescence and backscatter [*Boss et al.*, 2008]. The initial accuracy of the biogeochemical sensor suite is 2 μmol/kg for oxygen, 1 μmol/kg for nitrate, and 0.01 for pH. Quality-controlled float data were downloaded from the SOCCOMViz data portal (http://soccom.princeton.edu/soccomviz.php) and no additional adjustments

were applied to the data [*Williams et al.*, 2016]. Please refer to *Johnson et al.* [in press] for a detailed summary of sensor calibration and data quality.

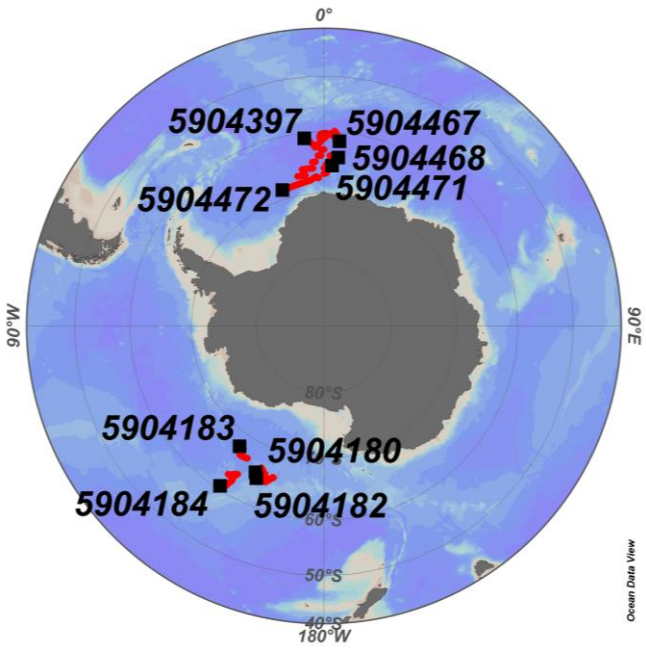

Figure 3.1. Location of SOCCOM floats deployed in the Pacific (2014) and Atlantic (2015) sectors of the Southern Ocean within the seasonal ice zone. Black dots indicate last position as of April 2016 and red dots indicate float trajectory.

Table 3.1. Float ID, deployment date, initial coordinates, and biogeochemical sensors on board with at least one full season under ice. Sensors marked (+) are onboard and fully operational, (-) not onboard, and (+/-) onboard but data have been flagged poor.

Float ID	Deployment date	Initial coordinates	O_2	pH	NO_3^-
5904180	3/31/2014	67° S, 156° W	+	-	+
5904183	4/1/2014	67° S, 150° W	+	-	+/-
5904184	4/3/2014	64° S, 150° W	+	+	+/-
5904182	4/10/2014	66° S, 162° W	+	-	-
5904467	12/14/2014	60° S, 0° E	+	-	+
5904471	12/21/2014	67° S, 0° E	+	+/-	+
5904472	1/18/2015	68° S, 2° W	+	+	+
5904468	1/19/2015	66° S, 0° E	+	+	+
5904397	1/22/2015	61° S, 0° E	+	+	+

Argo and Biogeochemical-Argo floats are programmed to profile from 2000 m to the surface once every ten days (from a nominal park depth of 1000 m). Temperature, salinity, pH, O_2, NO_3^-, and Chl-a fluorescence are directly measured. Total Alkalinity (TA) is estimated from float temperature, salinity, and O_2 using the Linearly Interpolated Alkalinity Regression (LIAR) algorithm [*Carter et al.*, 2016], and these estimated values are made available through the SOCCOM float data repository. Dissolved Inorganic Carbon (DIC) is then derived from pH and estimated TA. The estimated uncertainty in TA using the LIAR algorithm with inputs of T, S, and O_2 is ±6.5 μmol kg^{-1} for the global ocean, which translates to an uncertainty in DIC of approximately ±10 μmol kg^{-1} when computed with float pH with uncertainty of 0.01. The mixed layer depth (MLD) is defined here as the depth at which potential density (σ_θ) changes from the surface by 0.05 kg m^{-3}, chosen from inspecting

individual profiles (see Figure 2). Chl-a was derived from fluorescence data [*Boss and Haentjens,* 2016] and is used only qualitatively.

Floats deployed in the SIZ are equipped with ice avoidance software in order to protect the sensors from colliding with ice at the surface. When the float measures a temperature below a given threshold near the surface (~20 m) indicative of ice, the float immediately descends to the park depth and continues to cycle until two consecutive measurements are above the threshold temperature at which point the float surfaces and transmits its data via satellite. Because the float is not surfacing during the under-ice period, the coordinates of the float are unknown. The position of the float is then estimated by linearly interpolating between its last and first known positions. The temperature threshold criterion is only an indicator of ice and gives no information on the extent of cover or ice thickness. Satellite data were used to estimate the percent ice cover during the time when a float did not surface [*Meier et al.,* 2016].

Float 5904184, deployed April 2014 in the northern Ross Sea in the Pacific sector of the Southern Ocean (Table 3.1), is the central focus of this study because it displayed a very clean signal under ice and has pH and O_2 sensors. This float was in the SIZ for one annual cycle; the next year the float skirted the ice edge and never went under complete ice cover, which serves as a useful comparison for the significance of ice on physical and biogeochemical dynamics. Unfortunately, the NO_3^- sensor on this float became bio-fouled and the NO_3^- data are flagged poor.

2.2 Under ice remineralization rates

O_2, NO_3^-, and DIC inventories were calculated for the under-ice period of seven of the nine floats by integrating the surface to 300 m depth range (chosen based on the observation that seven of the floats in this analysis returned no significant temporal changes in density below 300 m). Integrating below the mixed layer depth to flat isopycnals was done to remove effects of vertical processes such as entrainment, detrainment, and advective transport in order to conserve the biogeochemical tracers. Floats 5904468 and 5904471 in the Atlantic sector, however, did not have constant isopycnals over time at depth and the inventories were calculated by integrating down to 70 m where a clear remineralization signal was observed for these two floats. It was assumed that ice cover acted as a cap between the ocean and atmosphere such that air-sea gas exchange was negligible for ice concentration greater than 70% [*Butterworth and Miller*, 2016]. Remineralization rates were then calculated from the slopes in O_2, NO_3^-, and DIC inventories during the period of ice cover and the ratio of C:N:O was computed. The first and last 2-3 under-ice profiles were removed from the fit because of the conservative nature of the ice avoidance software and hence likelihood of little to no ice cover.

In an effort to apply the same treatment across the floats, caution was taken to integrate to a depth greater than the deepest MLD of the suite of floats where flat isopycnals were observed with the exception of floats 5904468 and 5904471. When building the inventories, sensitivity to integration depth did not affect the resultant

remineralization rates between 200-300 m. Integrating down to the MLD seemed to provide a similar result but increased noise in the signal.

2.3 One-dimensional physical mixed layer model

In an attempt to separate the biological and physical changes captured in the observations, a simple one-dimensional bulk mixed layer model was used to simulate the physical component of the signal. The residual of the float observations minus the physical model output is then estimated to be the biological component assuming horizontal fluxes are small:

$$float\ data, f(physical, biological) - model\ output = biological\ component$$

Expanding upon work by *Plant et al.* [2016], the Price-Weller-Pinkel (PWP) model of mixed layer physics [*Price et al.*, 1986] was modified to include air-sea gas exchange of O_2 and CO_2, ice formation and melt, and biogeochemical tracers including O_2, NO_3^-, DIC, and TA [*Baehr and DeGrandpre*, 2004; *Glover et al.*, 2011; *Martz et al.*, 2008]. Biological processes were not incorporated into the model and the biogeochemical tracers were treated as biologically inert. *Plant et al.* [2016] was followed directly with the exception of using only *Liang et al.* [2013] for gas exchange parameterization, tuning the vertical eddy diffusivity coefficient, K_z, for the Southern Ocean, integrating a simplified ice production model, and adding other additional biogeochemical tracers (DIC, TA, and pCO_2). (Please refer to *Plant et al.* [2016] for a more detailed description of the model). This was an initial test to see if PWP can be applied to under-ice regions with profiling float observations; the model was specifically tuned for Ross Sea float 5904184 and only applied to this one float.

A simple thermodynamic ice production model was implemented by creating ice when the surface temperature fell below the freezing point of the surface seawater. Following *Hyatt et al.,* [2006], Equation 2 is used to calculate F_i, the rate at which ice is created in order to solve for the salt flux into the surface ocean in Equation 3, where c_p is the specific heat of seawater (4183.3 J/kg/C), L_f is the latent heat of fusion of sea ice (333 kJ/kg), T_{frz} is the freezing point of seawater, ρ_o and ρ_i refer to the density of seawater and ice respectively, and S_{ice} is set to 4.

$$\rho_i L_f F_i = \rho_o c_p \frac{T_{frz} - T_{surf}}{\Delta t} \Delta z \quad (2)$$

$$\frac{\Delta S}{\Delta t} = F_i \left(S_{surf} - S_{ice} \right) / \Delta z \quad (3)$$

More complex thermodynamic ice models exist, for example *Maykut and Untersteiner* [1971], however this simple ice production model is believed to capture the essential components of ice production and corresponding brine rejection on shorter timescales relevant to this study. To account for ice melt, an influx of fresh water was supplied to the surface to best fit the observations during the austral spring. During the period of ice cover, air-sea gas exchange was neglected for ice concentrations greater than 70% and the effective air-sea gas transfer velocity (k_{eff}) was scaled linearly to the open ocean value for ice cover from 0-70% [*Butterworth and Miller,* 2016]. Wind momentum was reduced to qualitatively best fit the data under the ice. During ice melt and ice formation, all tracers were diluted or concentrated correspondingly. A similar approach was taken by *Baehr and DeGrandpre* [2004] to evaluate under-ice CO_2 observations in a lake by adding ice to

the PWP model; however all gas exchange and wind momentum were turned off during ice cover in their approach.

The model was initialized with each profile and driven by 6-hr heat flux, winds, and net atmospheric freshwater flux data from the NCEP/NCAR Reanalysis [*Kalnay et al.*, 1996]. The model was then tuned by adjusting the background vertical eddy diffusivity, K_z, from $1 – 20 \times 10^{-5}$ m^2s^{-1}. Heat and salt offsets and a wind scaling factor were also optimized to minimize the residual between float and model temperature, salinity, and MLD. During near complete ice cover, a separate set of heat and salt offsets were optimized to best fit the data. The ability of the model to reproduce the physical processes was assessed by initializing the model with only the first profile and running the model out over one year. The NCP at each depth was calculated by subtracting the model output, reinitialized with each profile, from the float data using O_2 and DIC and the remineralization ratio determined during the under ice period to convert O_2 into carbon. Seasonal NCP was calculated by integrating the mean NCP rate during the under ice and ice free periods down to 75 m, based on the Chl-a signal (see Figure 3.3), to capture the euphotic zone and minimize contribution from error in the modelled MLD.

3 Results

3.1 Seasonal Ice Zone cycle

Physical and biogeochemical Hovmöller diagrams for Ross Sea float 5904184 are shown in Figures 3.2 and 3.3, demonstrating a typical seasonal cycle of float data in the SIZ. Note that the second winter shown in the record had only partial ice cover

and is thus not as cleanly representative of the full SIZ, but is instructive for observing the significance of sea ice influence on physical and biogeochemical processes. As austral winter approaches, the temperature drops and ice begins to form. Oxygen concentration increases to retain saturation as the water temperature drops, and salinity increases due to brine rejection. Increase in salinity could also be due to deepening of the MLD and mixing with higher saline deep water. Salt inventories during the onset of ice cover, however, suggest an increase of salinity due to brine rejection. During the period of ice cover, oxygen is drawn down and pH decreases due to biological respiration. As austral spring approaches, the surface temperature warms and the ice begins to melt. Freshening due to ice melt stratifies the upper water column at the ice edge causing the MLD to shoal from 100 to 50 m. At the ice melt edge, a phytoplankton bloom is observed in Chl-a data, with a corresponding increase in pH and O_2 supersaturation consistent with biological production.

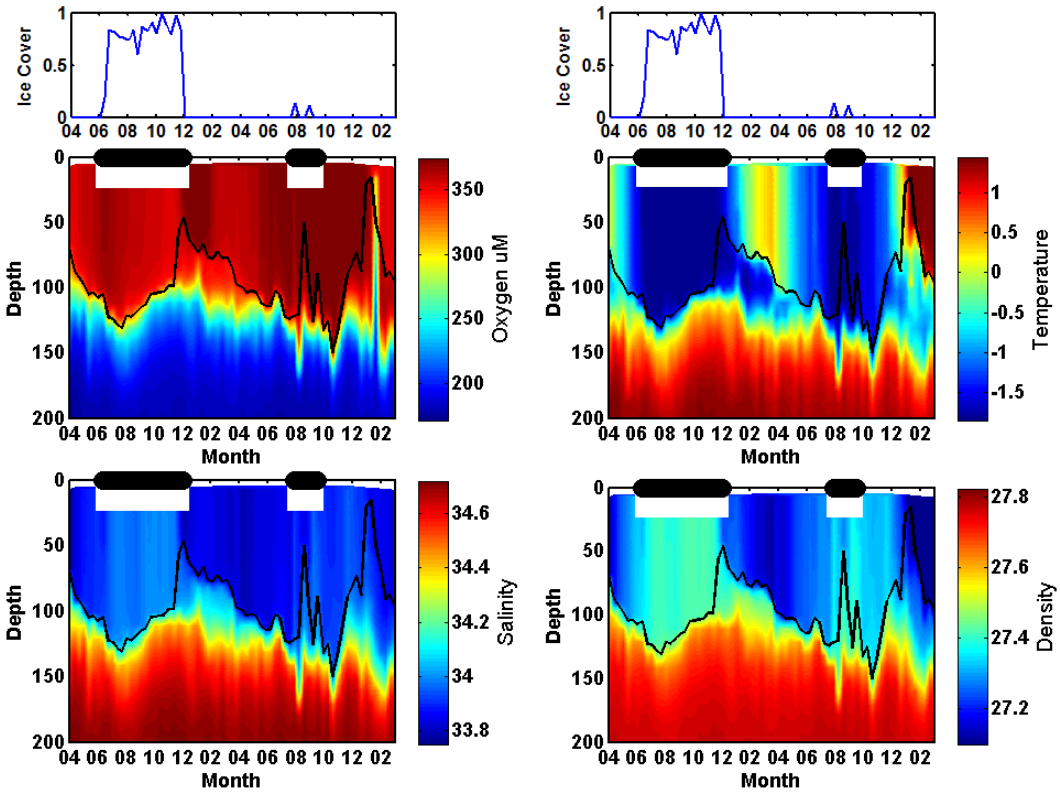

Figure 3.2. Hovmöller diagrams of in situ O_2, T, S, and σ_θ for Ross Sea float 5904184 deployed in April 2014, over a 22 month period showing one season under ice and one season with patchy to no ice cover. Black dots at the surface indicate when the float did not surface. The black line indicates the MLD. Fractional ice concentration, derived from satellite data, is shown in the top panels where 0 is no ice cover and 1 is complete cover.

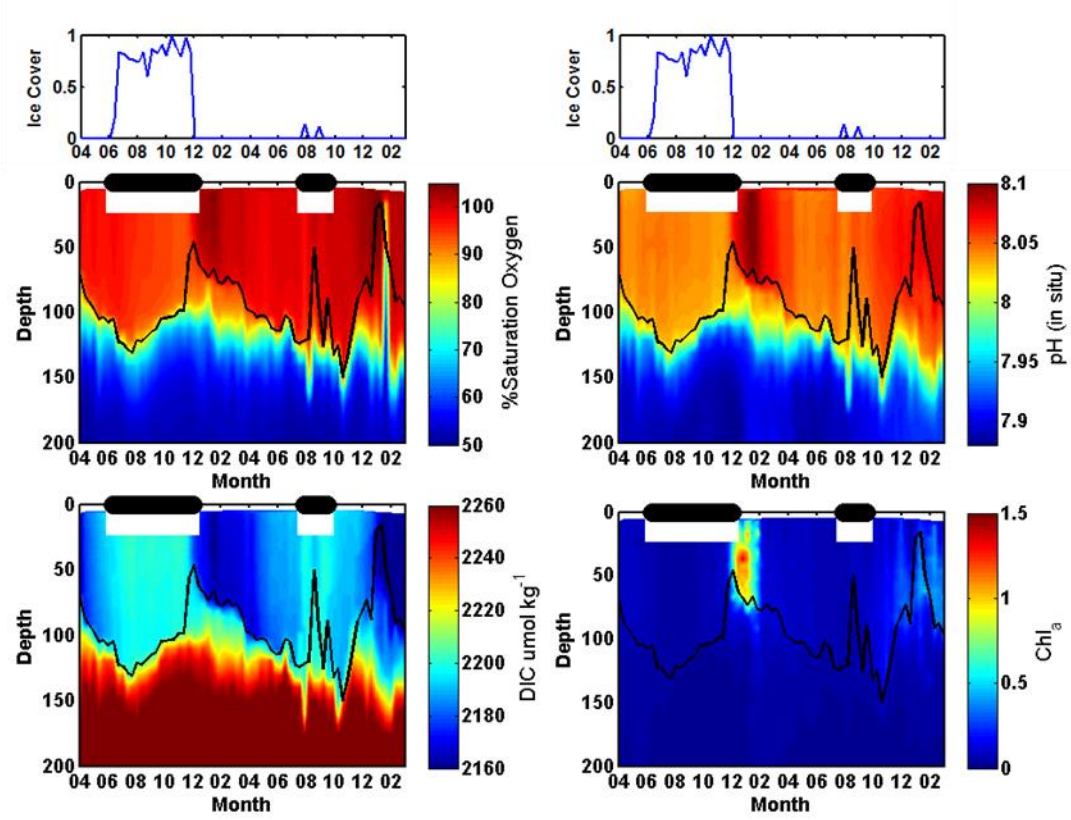

Figure 3.3. Hovmöller diagrams (as in Figure 2) of the biogeochemical float data for O_2 %sat, pH, DIC, and Chl-a as well as satellite derived ice cover.

3.2 Under ice remineralization

The O_2 and DIC inventories for the first annual cycle of float 5904184 one annual cycle are shown in Figure 3.4. There is a strong remineralization signal observed in the under-ice period as well as a strong production signal coinciding with ice melt. It is estimated from satellite data that all floats in this study experienced nearly complete ice cover over the duration of one austral winter. Figure 3.5 through Figure 3.7 show the inventories for the remaining floats in the SIZ. The remineralization rates calculated for all the floats in this study and goodness of fit (R^2) as well as the C:N:O ratios are listed in Table 3.2. In cases where no pH sensor was

available, ratios have been reported as *N*:O. Near-Redfieldian remineralization ratios (106:16:150) were observed for several of the floats; however, there was in all cases but one (float 5904180) greater consumption of oxygen relative to production of DIC and NO_3^- compared to Redfield. The mean ratio of *C*:N:O is 106:18(±2):285(±104) and *N*:O is 16:276(±95).

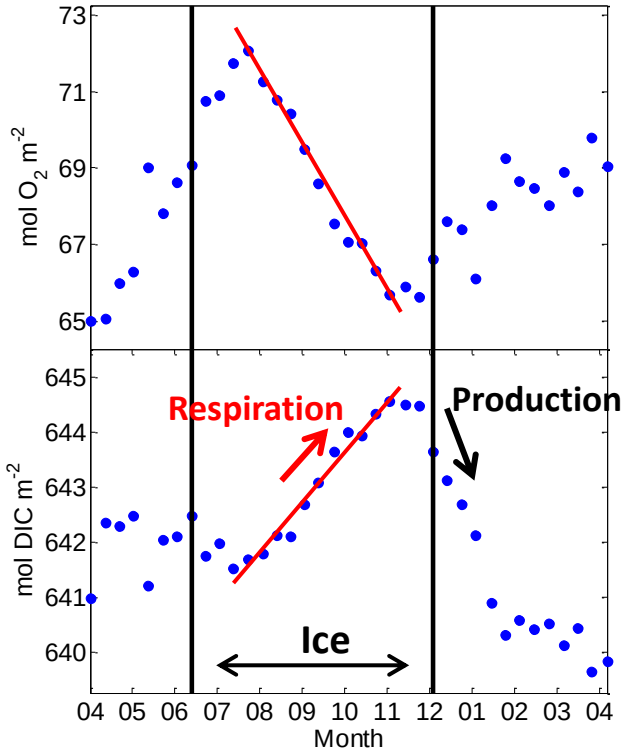

Figure 3.4. O_2 and DIC inventories for Ross Sea float 5904184. The float did not surface between early June and early December; however ice formation appears to have begun by early July and melt had begun by early November. The decrease in O_2 and corresponding increase in DIC during the under-ice period is attributed to remineralization. At the ice melt edge in December, the drawdown of DIC and increase in O_2 are due to a combination of biological production and physical processes such as gas exchange.

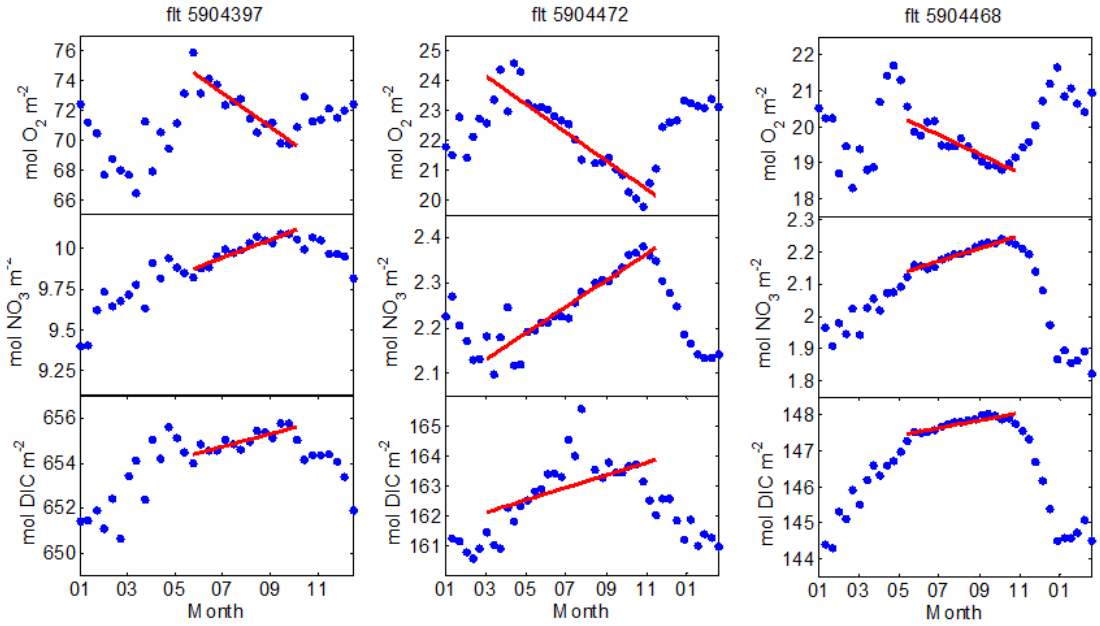

Figure 3.5. O_2, NO_3^-, and DIC inventories for floats 5904397, 5904472, and 5904468 used to compute under ice remineralization rates (red line).

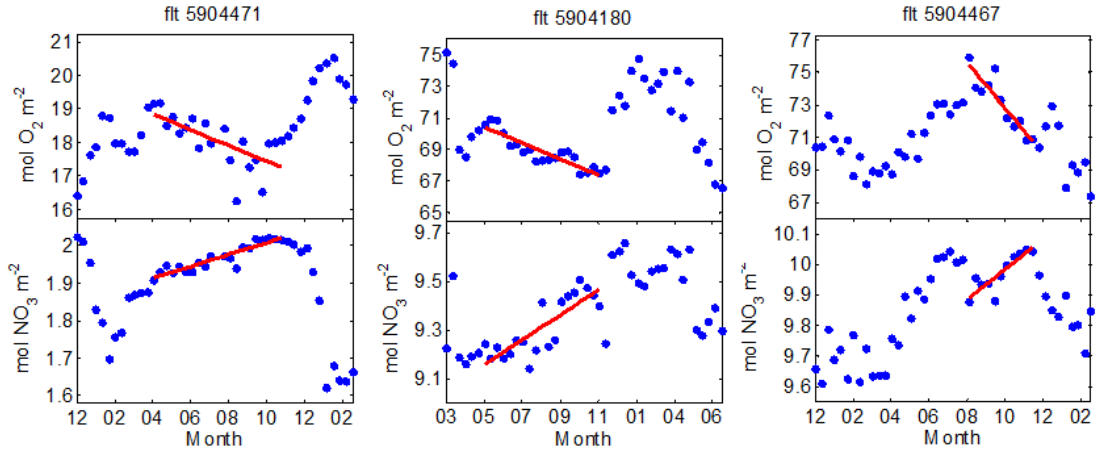

Figure 3.6. O2 and NO3- inventories for floats 5904471, 5904180, and 5904467 used to compute under ice remineralization rates (red line).

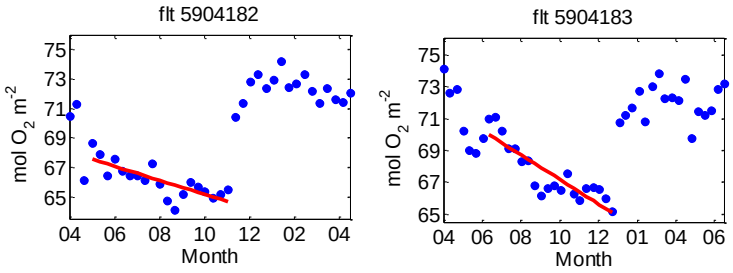

Figure 3.7. O_2, NO_3^-, and DIC inventories for floats 5904397, 5904472, and 5904468 used to compute under ice remineralization rates (red line).

Table 3.2. Remineralization rates of O_2, NO_3^-, and DIC in mmol m^{-2} d^{-1}, goodness of linear fit (R^2), and C:N:O ratios for the first set of SOCCOM floats deployed in the SIZ. Rates for floats 5904468 and 5904471 (marked *) were computed down to 70 m. s/f indicates the sensors flagged with poor data.

Float	DIC	NO_3^-	O_2	C:N:O
Pacific				
5904184	27.0 (0.94)	s/f	52.0 (0.98)	106:--:204
5904180	n/a	1.7 (0.66)	16.6 (0.80)	--:16:156
5904183	n/a	s/f	25.2 (0.77)	n/a
5904182	n/a	n/a	15.5 (0.61)	n/a
Atlantic				
5904468*	3.4 (0.71)	0.65 (0.91)	8.7 (0.79)	106:20:271
5904472	6.8 (0.26)	0.96 (0.86)	15.5 (0.81)	106:15:242
5904397	9.2 (0.63)	1.8 (0.85)	36.8 (0.82)	106:20:424
5904467	n/a	1.6 (0.76)	45.6 (0.82)	--:16:456
5904471*	s/f	0.5 (0.84)	7.7 (0.43)	--:16:246
Redfield				106:16:150

3.3 Model output and NCP

Surface T, S, σ_t, and MLD model output versus float data are shown in Figure 3.8 for the model initialized with only the first profile over one year beginning in April, 2014, for float 5904184. The model was then reinitialized with each profile using

similar tuning parameters. Table 3.3 lists the RMS error in the optimizing parameters (T, S, ρ, MLD) for values of K_z ranging from 1-20×10^{-5} m^2 s^{-1}. A costfunction,

$$J(K_z) = \sum (T_{model} - T_{obs})^2 E_T^{-2} + (S_{model} - S_{obs})^2 E_S^{-2} + (MLD_{model} - MLD_{obs})^2 E_M^{-2}$$

was used to determine an optimal K_z for float 5904184. E_T, E_S, and E_M were taken as 0.7 times the standard deviation of $T_{obs,}$ S_{obs}, and MLD_{obs} respectively, which assumes the model is able to fit 51% of the variance in observed T, S, and MLD. An ensemble of 5 model runs were used to determine an optimal value of K_z = 5×10^{-5} m^2 s^{-1}. The values of $J(K_z)$ imply the likelihood that K_z is optimal, and weighting the ensemble members by exp(-J) and taking the second moment gives an uncertainty for our estimate of K_z of 7×10^{-5} m^2 s^{-1}.

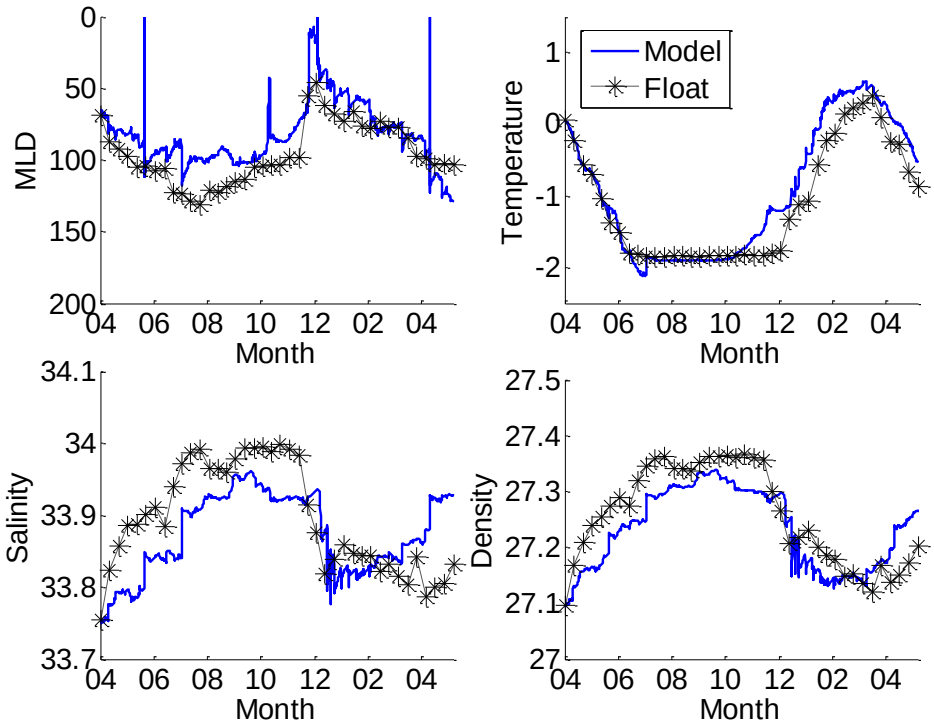

Figure 3.8. Model output (blue) compared to float data (black star) for surface T, S, and σ_t as well as MLD.

Table 3.3. RMS error of modelled T and S in the surface and full water column and RMS error in MLD for five different vertical eddy diffusivities.

Kz (10^{-5})	**T_{surf} RMS**	**T_{mean} RMS**	**S_{Surf} RMS**	**S_{mean} RMS**	**MLD RMS**
1	0.142	0.160	0.041	0.042	17.2
5	0.051	0.089	0.012	0.018	5.1
10	0.063	0.082	0.014	0.018	5.0
15	0.070	0.109	0.021	0.022	8.1
20	0.084	0.103	0.023	0.024	7.5

The seasonal cycle of NCP is shown in Figure 3.9 where net respiration is observed for half the year and the springtime bloom is the dominant production signal.

Table 3.4 lists the seasonal NCP computed during the austral winter (under ice) and austral summer (ice free) periods of the year by integrating the NCP rate profiles from the surface to various depths as well as from 100-300 m. The seasonal NCP during the ice free period is 1.5 and 3.6 mol C m^{-2} and the seasonal NCP during the under-ice period is -2.4 and -3.2 mol C m^{-2} derived from O_2 and DIC respectively where O_2 was translated to carbon using the remineralization ratio determined during the under-ice period of C:O = 106:204. The mean annual NCP (ANCP) derived from O_2 and DIC is shown in Figure 3.10. There is net respiration below 100 m that tapers to zero following particle attenuation with depth. The model generated values for gas exchange near zero with an influx of 8 mmol CO_2 m^{-2} yr^{-1} and 1.1 mmol O_2 m^{-2} yr^{-1} over the annual cycle. Gas flux was set to zero for a portion of the year due to near complete ice cover and gas flux estimates from profiling floats are the subject of ongoing work [*Williams et al.*, 2017].

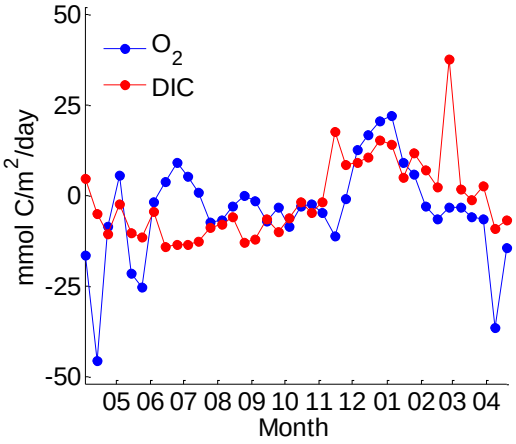

Figure 3.9. Seasonal cycle of NCP (float observations – model output) for the upper 75 m derived from O_2 (blue) and DIC (red) in mmol C m^{-2} day^{-1} for float 5904184 from April 2014 to April 2015. The ice edge bloom is evident beginning in November 2014.

Table 3.4. Seasonal NCP computed during the austral summer and austral winter from O_2 and derived DIC integrated from the surface to various depths.

Depth	Summer mol C m^{-2}	Summer mol O_2 m^{-2}	Winter mol C m^{-2}	Winter mol O_2 m^{-2}
50	0.6	0.7	-3.9	-0.8
75	3.6	0.8	-3.2	-1.2
100	5.0	2.7	0.2	-0.7
300	2.6	1.4	-3.9	-4.8
100-300	-2.4	-1.2	-3.9	-4.1

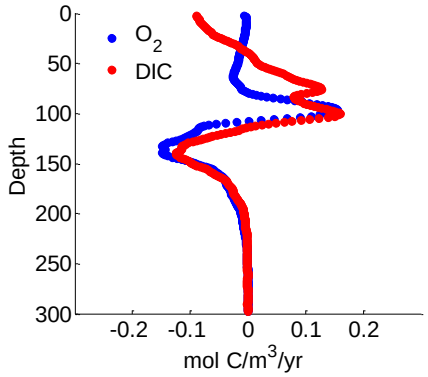

Figure 3.10. Mean ANCP for float 5904184 over the April 2014 to April 2015 year.

Multiple approaches were taken to estimate error in modelled NCP. An estimate of error was determined to be 14 mmol C m^{-2} day^{-1} by taking the RMS difference of the estimated upper 75 m NCP time series derived from DIC rather than O_2 (Figure 3.9) where the NCP error predominantly represents error in the gas exchange parameterization. The estimated error in DIC derived from pH data and the A_T algorithm is roughly 10 µmol kg^{-1}. By introducing an offset in DIC of 10 µmol kg^{-1},

the model output of ANCP ranges from ±7.6 mmol C m^{-2} yr^{-1}. Uncertainty in O_2, estimated to be 1%, translates to a range of ANCP of ±1.3 mmol O_2 m^{-2} yr^{-1}.

4 Discussion

4.1 Parsing the seasonal cycle

Float 5904184 appeared to go under complete ice cover during its first year (2014). However, even though the float did not surface for a few profiles the next year (2015), temperature, salinity, and O_2 as well as satellite data indicate patchy or negligible ice cover. This demonstrates the conservative nature of the ice avoidance software in predicting ice, which is essential for prolonging the life of the float in the SIZ. Without the support of the ice edge dynamics (i.e. shoaling of the MLD, increased vertical stability, and timing of nutrient availability with light throughput as ice melts), a springtime phytoplankton bloom was not observed the second year. There does appear to be a strong correlation between the timing of ice melt and initiation of the phytoplankton bloom in the SIZ. The vertical extent of the bloom observed from O_2, pH, and Chl-a data, as well as derived DIC and in NO_3^- where available, follows the MLD and is initiated concurrently with the shoaling of the MLD upon ice melt (Figure 3.3).

4.2 Under ice remineralization

A very clear remineralization signal ($R^2 > 0.7$) was observed for several of the floats, in particular for float 5904184. In the absence of ice cover, the oxygen concentration would have typically increased in order to maintain saturation near

100% as surface water temperature decreases. Due to the absence of air-sea interaction, the under-ice decrease in oxygen represents an exquisite and unambiguous observation of the organic matter remineralization rate. Similarly, the corresponding decrease in pH (increase in DIC) and increase in nitrate provide equally useful remineralization rates.

Even though a clear remineralization signal was observed for floats 5904397 and 5904467 deployed in the northern SIZ of the Atlantic sector, the computed ratio of C:N:O deviated substantially from Redfield. This deviation could be due to physical processes such as horizontal mixing, leads opening up in the ice, or migration of a float into a different water mass. It is important to note that it has been observed from profiling floats that processes with a small horizontal scale, like convection or ice edge processes will be susceptible to horizontal mixing [*Kortzinger et al.*, 2004]. Biogeochemical processes such as ikaite formation, phytoplankton community structure, preferential degradation of organic material, or influences from ice algae communities were also not accounted for and could affect the remineralization ratios. Error in the sensors or TA algorithm may also contribute to some of this deviation; the TA algorithm was likely poorly optimized in this region due to a lack of observations in the SIZ. Because there was a greater drawdown of O_2 relative to DIC and NO_3, opening of leads in the ice can be ruled out because the opposite trend would have been observed due to uptake of O_2 from the atmosphere by the undersaturated surface waters. At this time, the source(s) of the anomalous O_2 respiration rate relative to Redfield is an active research question. In spite of broad deviation from Redfield for a

couple floats and numerous sources of uncertainty, the mean C:N:O ratios for all the floats are within the error bars Redfieldian.

4.3 Net Community Production

The ANCP derived from both O_2 and DIC in the SIZ is near zero when integrated to the base of the euphotic zone, which differs from other studies at this latitude [*DeJong et al.*, 2017; *Ishii et al.*, 2002; *Lee*, 2001; *Z. Li et al.*, 2016; *Nevison et al.*, 2012; *Thomalla et al.*, 2015]. One obvious source of this apparent irregularity might simply be the large intra-annual variability. For example, if annual bloom intensity is linked to ice cover, then contiguous years may experience vastly different seasonally-integrated NCP values, skewing the ANCP that may be determined for any given 12 month period. Integrating to depths shallower than the base of the euphotic zone did not significantly change ANCP from zero (Table 3.4). This feature may be unique to the SIZ, as the under-ice period of the year is distinctly net-heterotrophic. During the ice free period and phytoplankton bloom, there was a positive NCP that nearly completely balanced with the negative NCP during the period of ice cover. The phytoplankton bloom was not as intense as observed for other floats in this region from Chl-a data, which could explain the lower than anticipated ANCP for Ross Sea float 5904184.

Most of the NCP signal derived as the difference between observations and the physical model was within the region of the MLD (Figure 3.10). When integrated down to 300 m, ANCP does not go to zero as anticipated which is likely due to model error in simulating the MLD (see figure 3.8) where strong vertical gradients are

present, hence mismatch between the model and observations rather than actual biological activity. To help remedy this mismatch, the water column above and below the modeled MLD was stretched or compressed to match the observed MLD from float data, following *Plant et al.* [2016]. However, this introduced more error in T and S around the MLD. Instead, NCP was integrated to the base of the euphotic zone in Figure 6 to remove errors resulting from the MLD region. The Chl-a signal during the springtime bloom does not exceed 75 m; thus most of the NCP signal below this depth in the model is believed to be primarily due to this mismatch of the model and float data within the MLD region.

From the seasonal cycle of NCP derived from *observations minus model*, four distinct regimes are observed in biological productivity and respiration. In the austral fall just prior to ice formation, there is little net production. Then in winter, during the under-ice period there is low production and respiration dominates (negative NCP). In the austral spring, ice melt gives way to an intense ice edge phytoplankton bloom and high productivity is captured by the *observations minus model* in both O_2 and DIC (positive NCP). After the bloom, productivity drops and the net biological activity (ANCP) balances to near zero.

The modelled NCP was not very sensitive to both uncertainty in DIC and O_2 as well as choice of optimization parameters. Through the range of uncertainty of DIC, the seasonal NCP cycle in the upper ocean varies from net heterotrophic during the under-ice period to net autotrophic during the ice free period. There are several sources of error in the model other than just in the estimated DIC and measured O_2

including error in physical input parameters (heat, wind, precipitation), ice formation/melt, gas parameterization, and horizontal advection; however, the upper and lower bounds on the estimated seasonal NCP fall within a reasonable range.

The modified PWP model used in this study requires significant float-specific tuning and is thus not easily applied in a bulk analysis of multiple floats and was therefore only applied to one float. There are also several sources of uncertainties; however, the model did help separate the biological and physical components of the pH and O_2 signal for Ross Sea float 5904184. Most noteworthy is that the model was able to capture the robust signal of seasonality in NCP that is apparent in the observations and unique to the ice zone (see Figure 3.9).

5 Conclusions

This was a preliminary analysis of a first of its kind dataset including a full annual cycle of pH in the SIZ. The significance of the ice edge in setting up favorable conditions for a phytoplankton bloom is evident in all nine floats included in this study. In particular, float 5904184 observed an ice edge bloom at the end of its first under ice season, but did not experience full ice cover in the subsequent year, with the consequence of no bloom. A clear under-ice remineralization signal is observed for most of the floats in this study. Most of the C:N:O ratios were reasonably close to Redfieldian, although O_2 appeared to have the greatest deviation from C and N and this discrepancy is not yet fully understood. The seasonal NCP for float 5904184 in the SIZ during the time of the phytoplankton bloom depleted up to 5 mol C m^{-2}, which is similar to other studies in this region but the under ice NCP nearly balances the

springtime NCP, drawing the ANCP to near zero. More complex models may be necessary to simulate the mixed layer physics and sea ice interactions in the SIZ; however a clear seasonal cycle in NCP was captured by the model and net heterotrophy was observed for about half of the year. As more floats are deployed that acquire a full annual cycle of data in the SIZ, this analysis of remineralization ratios and NCP can be expanded greatly.

Acknowledgements and data

Data were collected and made freely available by the Southern Ocean Carbon and Climate Observations and Modeling (SOCCOM) Project funded by the National Science Foundation, Division of Polar Programs (NSF PLR -1425989), supplemented by NASA, and by the International Argo Program and the NOAA programs that contribute to it. (http://www.argo.ucsd.edu, http://argo.jcommops.org). The Argo Program is part of the Global Ocean Observing System. There is no conflict of interest for any of the authors. I would like to thank Josh Plant with his help with developing the PWP model.

SOCCOM float data can be found at http://www3.mbari.org/soccom/SOCCOM_Data_Archive/. Ice concentration data can be found at http://nsidc.org/data/docs/noaa/g02202_ice_conc_cdr/index.html. NCEP Reanalysis data is provided by the NOAA/OAR/ESRL PSD, Boulder, Colorado, USA, from their Web site at http://www.esrl.noaa.gov/psd/.

Chapter 3, in full, is currently being prepared for submission for publication of the material. Ellen M. Briggs, Todd R. Martz, Lynne Talley, Matthew Mazloff,

Kenneth S. Johnson. The dissertation author was the primary investigator and author of this material.

References

Anderson, L. A., and J. L. Sarmiento (1994), Redfield ratios of remineralization determined by nutrient data analysis, *Global Biogeochemical Cycles*, *8*(1), 65-80.

Arrigo, K. R., and G. L. van Dijken (2003), Phytoplankton dynamics within 37 Antarctic coastal polynya systems, *Journal of Geophysical Research: Oceans*, *108*(C8), doi:10.1029/2002JC001739.

Arrigo, K. R., and G. L. van Dijken (2004), Annual changes in sea-ice, chlorophyll a, and primary production in the Ross Sea, Antarctica, *Deep Sea Research Part II: Topical Studies in Oceanography*, *51*(1-3), 117-138, doi:10.1016/j.dsr2.2003.04.003.

Baehr, M. M., and M. D. DeGrandpre (2004), In situ pCO2 and O2 measurements in a lake during turnover and stratification: Observations and modeling, *Limnology and Oceanography*, *49*(2), 330-340, doi:10.4319/lo.2004.49.2.0330.

Boss, E.B. and N. Haëntjens, 2016. Primer regarding measurements of chlorophyll fluorescence and the backscattering coefficient with WETLabs FLBB on profiling floats. SOCCOM Tech. Rep. 2016-1. http://soccom.princeton.edu/sites/default/files/files/SOCCOM_2016-1_Bio-opticsprimer.pdf.

Boss, E., D. Swift, L. Taylor, P. Brickley, R. Zaneveld, S. Riser, M. J. Perry, and P. G. Strutton (2008), Observations of pigment and particle distributions in the western North Atlantic from an autonomous float and ocean color satellite, *Limnology and Oceanography*, *53*(5part2), 2112-2122, doi:10.4319/lo.2008.53.5_part_2.2112.

Bushinsky, S. M., and S. Emerson (2015), Marine biological production from in situ oxygen measurements on a profiling float in the subarctic Pacific Ocean, *Global Biogeochemical Cycles*, *29*(12), 2050-2060, doi:10.1002/2015GB005251.

Butterworth, B. J., and S. D. Miller (2016), Air-sea exchange of carbon dioxide in the Southern Ocean and Antarctic marginal ice zone, *Geophysical Research Letters*, *43*(13), 7223-7230, doi:10.1002/2016GL069581.

Carter, B. R., N. L. Williams, A. R. Gray, and R. A. Feely (2016), Locally interpolated alkalinity regression for global alkalinity estimation, *Limnology and Oceanography: Methods*, *14*(4), 268-277, doi:10.1002/lom3.10087.

DeJong, H. B., R. B. Dunbar, D. A. Koweek, D. A. Mucciarone, S. K. Bercovici, and D. A. Hansell (2017), Net community production and carbon export during the late summer in the Ross Sea, Antarctica, *Global Biogeochemical Cycles*, doi:10.1002/2016gb005417.

Delille, B., M. Vancoppenolle, N.-X. Geilfus, B. Tilbrook, D. Lannuzel, V. Schoemann, S. Becquevort, G. Carnat, D. Delille, C. Lancelot, L. Chou, G. S. Dieckmann, and J.-L. Tison (2014), Southern Ocean CO2 sink: The contribution of the sea ice, *Journal of Geophysical Research: Oceans*, *119*(9), 6340-6355, doi:10.1002/2014JC009941.

Eveleth, R., N. Cassar, R. M. Sherrell, H. Ducklow, M. P. Meredith, H. J. Venables, Y. Lin, and Z. Li (2016), Ice melt influence on summertime net community production along the Western Antarctic Peninsula, *Deep Sea Research Part II: Topical Studies in Oceanography*, doi:http://dx.doi.org/10.1016/j.dsr2.2016.07.016.

Ferrari, R., S. T. Merrifield, and J. R. Taylor (2015), Shutdown of convection triggers increase of surface chlorophyll, *Journal of Marine Systems*, *147*, 116-122, doi:http://dx.doi.org/10.1016/j.jmarsys.2014.02.009.

Fitch, D. T., and J. K. Moore (2007), Wind speed influence on phytoplankton bloom dynamics in the Southern Ocean Marginal Ice Zone, *Journal of Geophysical Research: Oceans*, *112*(C8), doi:10.1029/2006JC004061.

Glover, D. M., W. J. Jenkins, and S. C. Doney (2011), *Modeling methods for marine science*, Cambridge University Press.

Hennon, T. D., S. C. Riser, and S. Mecking (2016), Profiling float-based observations of net respiration beneath the mixed layer, *Global Biogeochemical Cycles*, *30*(6), 920-932, doi:10.1002/2016GB005380.

Hyatt, J. (2006). Wind, sea ice, inertial oscillations and upper ocean mixing in Marguerite Bay, Western Antarctic Peninsula: observations and modeling (No. MIT/WHOI-2006-16). WOODS HOLE OCEANOGRAPHIC INSTITUTION MA.

Ishii, M., H. Y. Inoue, and H. Matsueda (2002), Net community production in the marginal ice zone and its importance for the variability of the oceanic pCO2 in the Southern Ocean south of Australia, *Deep Sea Research Part II: Topical Studies in Oceanography*, *49*(9–10), 1691-1706, doi:http://dx.doi.org/10.1016/S0967-0645(02)00007-3.

Johnson, K. S., L. J. Coletti, H. W. Jannasch, C. M. Sakamoto, D. D. Swift, and S. C. Riser (2013), Long-Term Nitrate Measurements in the Ocean Using the in situ Ultraviolet Spectrophotometer: Sensor Integration into the APEX Profiling Float, *Journal of Atmospheric and Oceanic Technology*, *30*(8), 1854-1866, doi:10.1175/jtech-d-12-00221.1.

Johnson, K. S., H. W. Jannasch, L. J. Coletti, V. A. Elrod, T. R. Martz, Y. Takeshita, R. J. Carlson, and J. G. Connery (2016), Deep-Sea DuraFET: A Pressure Tolerant pH Sensor Designed for Global Sensor Networks, *Analytical chemistry*, *88*(6), 3249-3256, doi:10.1021/acs.analchem.5b04653.

Johnson, K. S., J. N. Plant, S. C. Riser, and D. Gilbert (2015), Air Oxygen Calibration of Oxygen Optodes on a Profiling Float Array, *Journal of Atmospheric and Oceanic Technology*, *32*(11), 2160-2172, doi:10.1175/jtech-d-15-0101.1.

Johnson, K. S., S. C. Riser, and D. M. Karl (2010), Nitrate supply from deep to near-surface waters of the North Pacific subtropical gyre, *Nature*, *465*(7301), 1062-1065, doi:10.1038/nature09170.

Johnson, K. S., J. N. Plant, L. J. Coletti, H. W. Jannasch, C. M. Sakamoto, S. C. Riserm D. D. Swift, N. L. Williams, E. Boss, N. Haëntjens, L. D. Talley, J. L. Sarmiento (in press), Biogeochemical sensor performance in the SOCCOM profiling float array, *Journal of Geophysical Research: Oceans.*

Juranek, L. W., R. A. Feely, D. Gilbert, H. Freeland, and L. A. Miller (2011), Real-time estimation of pH and aragonite saturation state from Argo profiling floats: Prospects for an autonomous carbon observing strategy, *Geophysical Research Letters*, *38*(17), doi:10.1029/2011GL048580.

Kalnay, E., M. Kanamitsu, R. Kistler, W. Collins, D. Deaven, L. Gandin, M. Iredell, S. Saha, G. White, and J. Woollen (1996), The NCEP/NCAR 40-year reanalysis project, *Bulletin of the American meteorological Society*, *77*(3), 437-471.

Khatiwala, S., F. Primeau, and T. Hall (2009), Reconstruction of the history of anthropogenic CO2 concentrations in the ocean, *Nature*, *462*(7271), 346-349, doi:10.1038/nature08526.

Kortzinger, A., J. Schimanski, U. Send, and D. W. Wallace (2004), The ocean takes a deep breath, *Science*, *306*, 1337, doi:10.1126/science.1102557.

Lannuzel, D., M. Vancoppenolle, P. van der Merwe, J. de Jong, K. M. Meiners, M. Grotti, J. Nishioka, and V. Schoemann (2016), Iron in sea ice: Review and new insights, *Elementa: Science of the Anthropocene*, *4*, 000130, doi:10.12952/journal.elementa.000130.

Lee, K. (2001), Global net community production estimated from the annual cycle of surface water total dissolved inorganic carbon, *Limnology and Oceanography*, *46*(6), 1287-1297, doi:10.4319/lo.2001.46.6.1287.

Li, Y.-H., and T.-H. Peng (2002), Latitudinal change of remineralization ratios in the oceans and its implication for nutrient cycles, *Global Biogeochemical Cycles*, *16*(4), 77-71-77-16, doi:10.1029/2001GB001828.

Li, Z., N. Cassar, K. Huang, H. Ducklow, and O. Schofield (2016), Interannual variability in net community production at the Western Antarctic Peninsula region (1997–2014), *Journal of Geophysical Research: Oceans*, *121*(7), 4748-4762, doi:10.1002/2015JC011378.

Liang, J.-H., C. Deutsch, J. C. McWilliams, B. Baschek, P. P. Sullivan, and D. Chiba (2013), Parameterizing bubble-mediated air-sea gas exchange and its effect on ocean ventilation, *Global Biogeochemical Cycles*, *27*(3), 894-905, doi:10.1002/gbc.20080.

Majkut, J. D., B. R. Carter, T. L. Frolicher, C. O. Dufour, K. B. Rodgers, and J. L. Sarmiento (2014), An observing system simulation for Southern Ocean carbon dioxide uptake, *Philosophical transactions. Series A, Mathematical, physical, and engineering sciences*, *372*(2019), 20130046, doi:10.1098/rsta.2013.0046.

Martz, T. R., J. G. Connery, and K. S. Johnson (2010), Testing the Honeywell Durafet for seawater pH applications, *Limnology and Oceanography: Methods*, *8*, 172-184, doi:10.4319/lom.2010.8.172.

Martz, T. R., K. S. Johnson, and S. C. Riser (2008), Ocean metabolism observed with oxygen sensors on profiling floats in the South Pacific, *Limnology and Oceanography*, *53*(5part2), 2094-2111, doi:10.4319/lo.2008.53.5_part_2.2094.

Maykut, G. A., and N. Untersteiner (1971), Some results from a time-dependent thermodynamic model of sea ice, *Journal of Geophysical Research*, *76*(6), 1550-1575, doi:10.1029/JC076i006p01550.

Meier, W., R. Duerr, F. Fetterer, and J. Stroeve. 2016. NOAA:NSIDC Climate Data Record of Passive Microwave Sea Ice Concentration, Version 2. March 2014 to February 2016. Boulder, Colorado USA. NSIDC: National Snow and Ice Data Center. doi:http://nsidc.org/data/docs/noaa/g02202_ice_conc_cdr/index.html. Accessed March 1, 2016.

Nevison, C. D., R. F. Keeling, M. Kahru, M. Manizza, B. G. Mitchell, and N. Cassar (2012), Estimating net community production in the Southern Ocean based on atmospheric potential oxygen and satellite ocean color data, *Global Biogeochemical Cycles*, *26*(1), doi:10.1029/2011GB004040.

Plant, J. N., K. S. Johnson, C. M. Sakamoto, H. W. Jannasch, L. J. Coletti, S. C. Riser, and D. D. Swift (2016), Net community production at Ocean Station Papa observed with nitrate and oxygen sensors on profiling floats, *Global Biogeochemical Cycles*, *30*(6), 859-879, doi:10.1002/2015GB005349.

Price, J. F., R. A. Weller, and R. Pinkel (1986), Diurnal cycling: Observations and models of the upper ocean response to diurnal heating, cooling, and wind mixing, *Journal of Geophysical Research: Oceans*, *91*(C7), 8411-8427, doi:10.1029/JC091iC07p08411.

Rysgaard, S., J. Bendtsen, B. Delille, G. S. Dieckmann, R. N. Glud, H. Kennedy, J. Mortensen, S. Papadimitriou, D. N. Thomas, and J.-L. Tison (2011), Sea ice contribution to the air-sea CO2 exchange in the Arctic and Southern Oceans, *Tellus B*, *63*(5), 823-830, doi:10.1111/j.1600-0889.2011.00571.x.

Sabine, C. L., R. A. Feely, N. Gruber, R. M. Key, K. Lee, J. L. Bullister, R. Wanninkhof, C. S. Wong, D. W. Wallace, B. Tilbrook, F. J. Millero, T. H. Peng, A. Kozyr, T. Ono, and A. F. Rios (2004), The oceanic sink for anthropogenic CO2, *Science*, *305*(5682), 367-371, doi:10.1126/science.1097403.

Shadwick, E. H., B. Tilbrook, N. Cassar, T. W. Trull, and S. R. Rintoul (2014), Summertime physical and biological controls on O2 and CO2 in the Australian Sector of the Southern Ocean, *Journal of Marine Systems*, doi:10.1016/j.jmarsys.2013.12.008.

Shadwick, E. H., T. W. Trull, B. Tilbrook, A. J. Sutton, E. Schulz, and C. L. Sabine (2015), Seasonality of biological and physical controls on surface ocean CO2from hourly observations at the Southern Ocean Time Series site south of Australia, *Global Biogeochemical Cycles*, *29*(2), 223-238, doi:10.1002/2014gb004906.

Smith, W. O., Jr., and D. M. Nelson (1986), Importance of Ice Edge Phytoplankton Production in the Southern Ocean, *BioScience*, *36*(4), 251-257, doi:10.2307/1310215.

Sverdrup, H. (1953), On conditions for the vernal blooming of phytoplankton, *Journal du Conseil*, *18*(3), 287-295.

Tengberg, A., J. Hovdenes, H. J. Andersson, O. Brocandel, R. Diaz, D. Herbert, T. Americh, C. Huber, Kortzinger, A. A. Khripounoff, F. Rey, C. Ronning, J. Schimanski, S. Sommer, and A. Stangelmayer (2006), Evaluation of a lifetime-based optode to measure oxygen in aquatic systems, *Limnology and Oceanography: Methods*, *4*(2), 7-17, doi:10.4319/lom.2006.4.7.

Thomalla, S. J., M.-F. Racault, S. Swart, and P. M. S. Monteiro (2015), High-resolution view of the spring bloom initiation and net community production in

the Subantarctic Southern Ocean using glider data, *ICES Journal of Marine Science: Journal du Conseil*, doi:10.1093/icesjms/fsv105.

Tortell, P. D., H. C. Bittig, A. Körtzinger, E. M. Jones, and M. Hoppema (2015), Biological and physical controls on N2, O2, and CO2 distributions in contrasting Southern Ocean surface waters, *Global Biogeochemical Cycles*, *29*(7), 994-1013, doi:10.1002/2014GB004975.

Williams, N. L., L. W. Juranek, K. S. Johnson, R. A. Feely, S. C. Riser, L. D. Talley, J. L. Russell, J. L. Sarmiento, and R. Wanninkhof (2016), Empirical algorithms to estimate water column pH in the Southern Ocean, *Geophysical Research Letters*, *43*(7), 3415-3422, doi:10.1002/2016GL068539.

Williams, N. L., L. W. Juranek, R. A. Feely, K. S. Johnson, J. L. Sarmiento, L. D. Talley, A. G. Dickson, A. R. Gray, R. Wanninkhof, J. L. Russell, S. C. Riser, and Y. Takeshita (2017), Calculating surface ocean pCO2 from biogeochemical Argo floats equipped with pH: An uncertainty analysis, *Global Biogeochemical Cycles*, 591-604, doi:10.1002/2016GB005541.

CHAPTER 4: THE ROLE OF $CACO_3$ IN THE MARINE CARBON CYCLE IN THE SOUTHERN OCEAN FROM PROFILING FLOATS

Abstract

There is evidence for a 'great calcite belt' where enhanced production of calcifying coccolithophores is exhibited annually during the austral summer that encircles the entire Southern Ocean. However, the role of the $CaCO_3$ system in the global marine carbon system is not well constrained, especially in the Southern Ocean. When $CaCO_3$ is precipitated, CO_2 is produced and vice versa in a ratio that is scaled by a factor of Ψ due to the buffering effect of the carbonate system. Globally, Ψ ranges from 0.66 near the surface and increases to 0.85 at depths greater than 1000 m. The vertical variation of Ψ has implications for the balance between the $CaCO_3$-mediated influx of CO_2 due to greater uptake of CO_2 during dissolution of $CaCO_3$ at depth relative to CO_2 released during $CaCO_3$ production in the upper ocean. Here we use biogeochemical data from profiling floats deployed as part of the Southern Ocean Carbon and Climate Modeling and Observations (SOCCOM) project, to calculate Ψ and explore the implications of the variability in Ψ in space and time under future projections of changing oceanic pCO_2. The mean surface and deep Ψ for the Southern Ocean were calculated to be 0.76 ±0.04 and 0.83 ±0.02 respectively from profiling float data. There is significant variability in Ψ in the different frontal zones as well as seasonal variability in the surface. Under elevated pCO_2 conditions, here we estimate that the role of the pelagic $CaCO_3$ pump in the Southern Ocean will transition from a net sink to a net source of CO_2 to the atmosphere.

1 Introduction

The Southern Ocean plays an intrinsic role in the global carbon cycle. Physical dynamics of the Southern Ocean are the principal driving force of meridional overturning circulation and provide the primary window by which intermediate, deep, and bottom waters reach the surface and interact with the atmosphere [*Marshall and Speer*, 2012]. It is estimated that the Southern Ocean south of 44°S accounts for 25-30% of the annual oceanic uptake of anthropogenic CO_2 [*Mikaloff Fletcher et al.*, 2006]. The Southern Ocean may have been a net source of CO_2 to the atmosphere in preindustrial times due to upwelling of C_T (total dissolved inorganic carbon) rich deep water; however, under elevated atmospheric pCO_2 the Southern Ocean presently serves as a net sink [*Morrison et al.*, 2015; *Takahashi et al.*, 2012]. There are two primary biogeochemical carbon pumps: the soft biological pump (production and respiration) and the $CaCO_3$ pump (precipitation and dissolution). There is a significantly large pelagic component to the $CaCO_3$ pump in the open ocean, and even though this pump cycles carbon at a slower rate than the soft biological pump, the $CaCO_3$ pump is responsible for a greater net transfer of carbon to the interior of the ocean and burial in sediments [*Smith and Mackenzie*, 2016]. The role of the $CaCO_3$ system in the global marine carbon system, however, is not well constrained, especially in the Southern Ocean due to limited observations.

In the open ocean, autotrophic coccolithophore blooms comprise the majority of pelagic $CaCO_3$ production; however, there are also heterotrophic calcifiers

including foraminfera and pteropods [*Iglesias-Rodriguez et al.*, 2002]. There is evidence from satellite data for a 'great calcite belt' (GCB) where enhanced production of calcifying coccolithophores is exhibited annually during the austral summer that encircles the entire Southern Ocean across the Subantarctic and Suptropical frontal zones [*Balch et al.*, 2016; *Balch et al.*, 2011; *Rosengard et al.*, 2015]. The standing stock of PIC (particulate inorganic carbon) in the GBC region accounts for 26% of the global satellite signal, even though this region encompasses only 18% of the open ocean. There is direct evidence of enhanced coccolithopore production within this region, and it could be considered the most concentrated coccolithophore assemblage in the global open ocean [*Balch et al.*, 2016; *Painter et al.*, 2010; *Rosengard et al.*, 2015]. There is no tropical benthic production and very little shelf or benthic production of $CaCO_3$ in the open Southern Ocean so this region serves a unique role as a planktonic endmember of $CaCO_3$ reactions to the global ocean.

When $CaCO_3$ is precipitated, CO_2 is produced and vice versa in a ratio that is scaled by a factor of Ψ due to the buffering effect of the carbonate system:

$$Ca^{2+} + (1 + \Psi)HCO_3^- + (1 - \Psi)OH^- = CaCO_3 + \Psi CO_2 + H_2O.$$

Ψ is a buffering capacity indicator of the ocean's ability to hold CO_2 similar to the Revelle factor [*Broecker et al.*, 1979; *Egleston et al.*, 2010; *Frankignoulle et al.*, 1994; *Revelle and Suess*, 1957; *Sundquist et al.*, 1979], and though these two factors are related, they are not interchangeable. Ψ specifically addresses the relative contribution to changes in C_T due to $CaCO_3$ reactions. Globally, Ψ ranges from 0.66 near the surface and increases to 0.85 at depths greater than 1000 m [*Smith and Mackenzie*,

2016]. Because Ψ is lower in the surface ocean where pelagic $CaCO_3$ production occurs and Ψ is greater at depth where dissolution primarily occurs, the net CO_2 flux associated with the pelagic $CaCO_3$ cycle is a sink for CO_2.

In the contemporary global ocean it has been demonstrated that the net flux of CO_2 associated with the organic carbon and $CaCO_3$ reaction couplets is nearly balanced when integrated over the global ocean water column [*Smith and Mackenzie*, 2016]. Ψ has varied substantially over time, primarily due to variation in atmospheric pCO_2. Here biogeochemical data from profiling floats deployed as part of the Southern Ocean Carbon and Climate Modeling and Observations (SOCCOM) project are used to calculate Ψ and explore the implications of the variability in Ψ in space and time under future projections of changing atmospheric pCO_2.

2 Methods

Ψ is calculated as outlined in *Smith and Gattuso* [2011], by first starting with a known C_T and A_T (total alkalinity). Then 100 μmol kg^{-1} of $CaCO_3$ is precipitated, though the actual value is not significant, which reduces A_T by 200 μmol kg^{-1}. The pCO_2 rises with the precipitation of $CaCO_3$ but eventually returns to a state of equilibrium. The gas equilibrated C_T is computed from the original pCO_2 and new A_T and Ψ is calculated as the relative change in C_T due to gas evasion and equilibration to the change in C_T due to $CaCO_3$ precipitation (100 μmol kg^{-1}):

$$\Psi = \frac{\Delta C_{\mathrm{T(gas)}}}{\Delta C_{T(CaCO3)}}.$$

QC profiling float data was downloaded from the soccomviz website (http://www3.mbari.org/SOCCOM/). Three algorithms were used in estimating A_T used in conjunction with float pH data for calculating C_T, pCO_2, and Ψ. The LIAR (linear interpolated alkalinity algorithm) was developed for the global ocean [Carter et al., 2016] whereas the MLR (multiple linear regression) algorithm is focused on the Southern Ocean [Williams et al., 2017] but both were developed following the same principle of regression. The CANYON (CArbonate system and Nutrients concentration from 22 hYdrological properties and Oxygen using a Neural-network) algorithm is based on a neural networks approach for the global ocean [Sauzède et al., submitted]. In addition to computing the mean Ψ for the entire Southern Ocean, the profiles were divided into 6 distinct frontal zones: Boundary, South Antarctic Circumpolar Front (SACCF), Polar Front (PF), Subantarctic Front (SAF), Subtropical Front (STF), and North of the STF (N. STF) defined by Orsi et al. [1995] as shown in Figure 4.1.

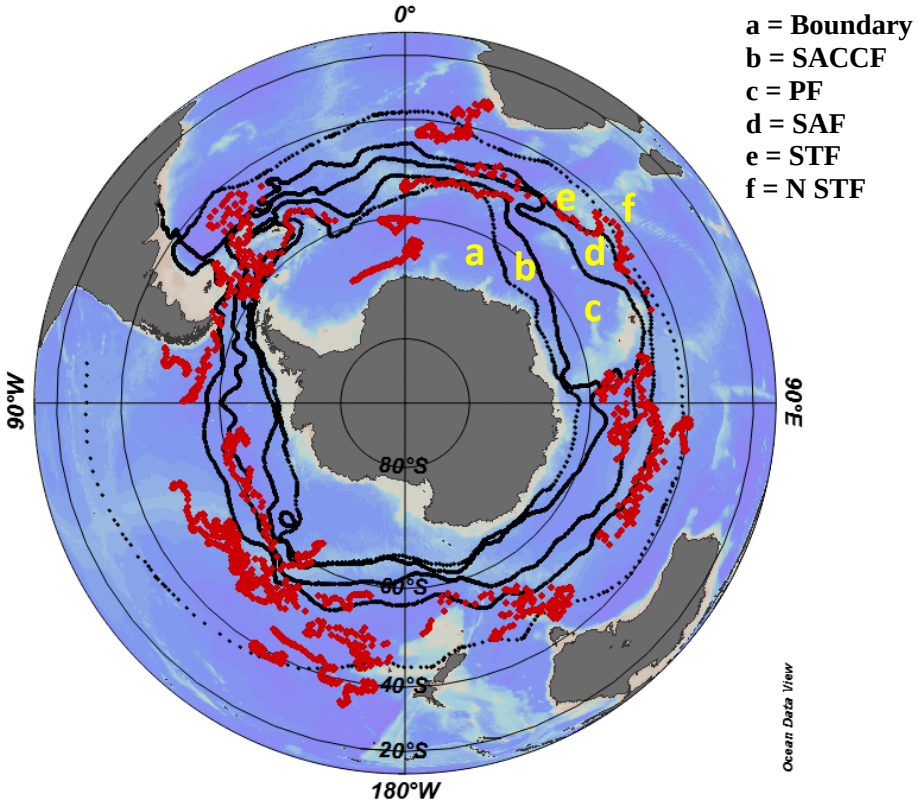

Figure 4.1. Position of biogeochemical Argo floats (red) within the frontal zones (black).

A simple 3 layer box model comprised of a shallow, deep, and sediments box was designed to simulate the impact of the carbonate cycle on CO_2 gas exchange with the atmosphere in the Southern Ocean under the present and future climate scenarios. $CaCO_3$ production rates in the shallow box were estimated based on satellite data used by *Freeman and Lovenduski* [2015] with the satellite PIC algorithm developed by *Balch et al.* [2007] for the very surface and integrating down to the estimated depth of the euphotic zone (~50 m). It was assumed that most of the $CaCO_3$ production occurs during the austral summer as indicated by satellite data so annual rates were calculated

assuming near negligible wintertime production. Sedimentation rates were estimated by taking the fraction of the global value that would correspond to the area of the GBC. Dissolution rates were then calculated as the difference between the production and sedimentation rates. For the sake of simplification, dissolution was assumed not to occur in the shallow box. The mean surface and deep Ψ values for the Southern Ocean were used in the calculation of CO_2 fluxes associated with calcification and dissolution.

Using the estimated mean change in surface pCO_2 for the Southern Ocean of 23.9 μatm decade^{-1} from *Takahashi et al.,* [2012], Ψ in the shallow box was recalculated for the year 2100. C_T was calculated from the elevated pCO_2 and original A_T assuming that A_T will stay relatively constant with oceanic uptake of anthropogenic CO_2 [*Orr et al.,* 2005]. The same 3 box calculation was performed as outlined above under the elevated pCO_2 conditions. The production, dissolution, and sedimentation rates were unchanged which is likely inaccurate but the key focus was to assess the relative effect of changes in Ψ due to elevated pCO_2.

3 Results

A_T derived from the LIAR algorithm and C_T computed from the derived A_T and pH measured from profiling floats are compared to historical bottle data in Figure 4.2 and Figure 4.3. There is good qualitative agreement between the float derived carbon parameters and bottle data. Calculation of the mean Ψ for the whole Southern Ocean from profiling floats agrees well between the three algorithms used to estimate A_T and is similar to historical data as shown in Table 4.1. The deep value for the basin

wide Ψ is marginally lower from the float data but the surface value is within the standard deviation. Ψ computed from profiling float data is shown at four different depths in Figure 4.4. The winter and summer surface Ψ are shown separately in Figure 4.5. There is a clear seasonal cycle in Ψ that is not accounted for in historical data.

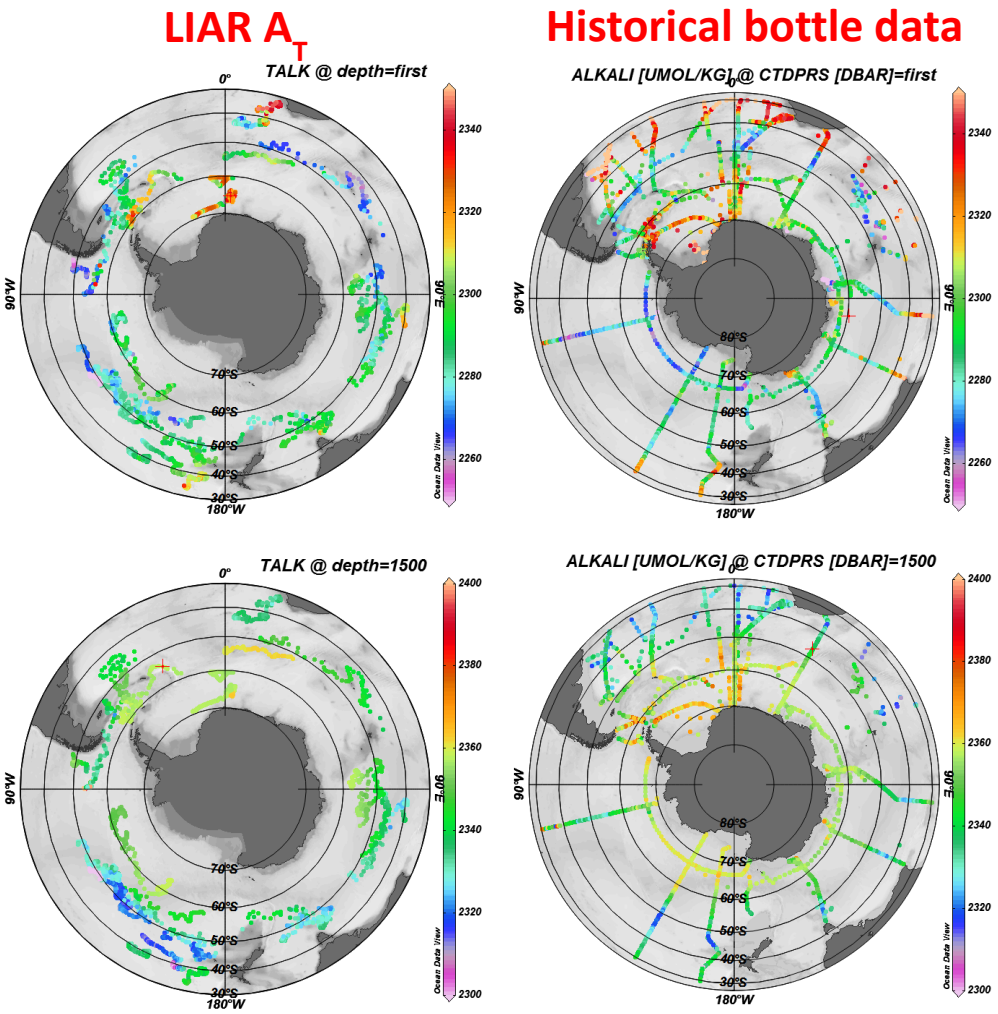

Figure 4.2. A_T estimated from the LIAR algorithm at the surface (top left) and at 1500 m (bottom left) compared to historical bottle data at the surface (top right) and at 1500 m (bottom right). There is qualitative good agreement between the algorithm and bottle data.

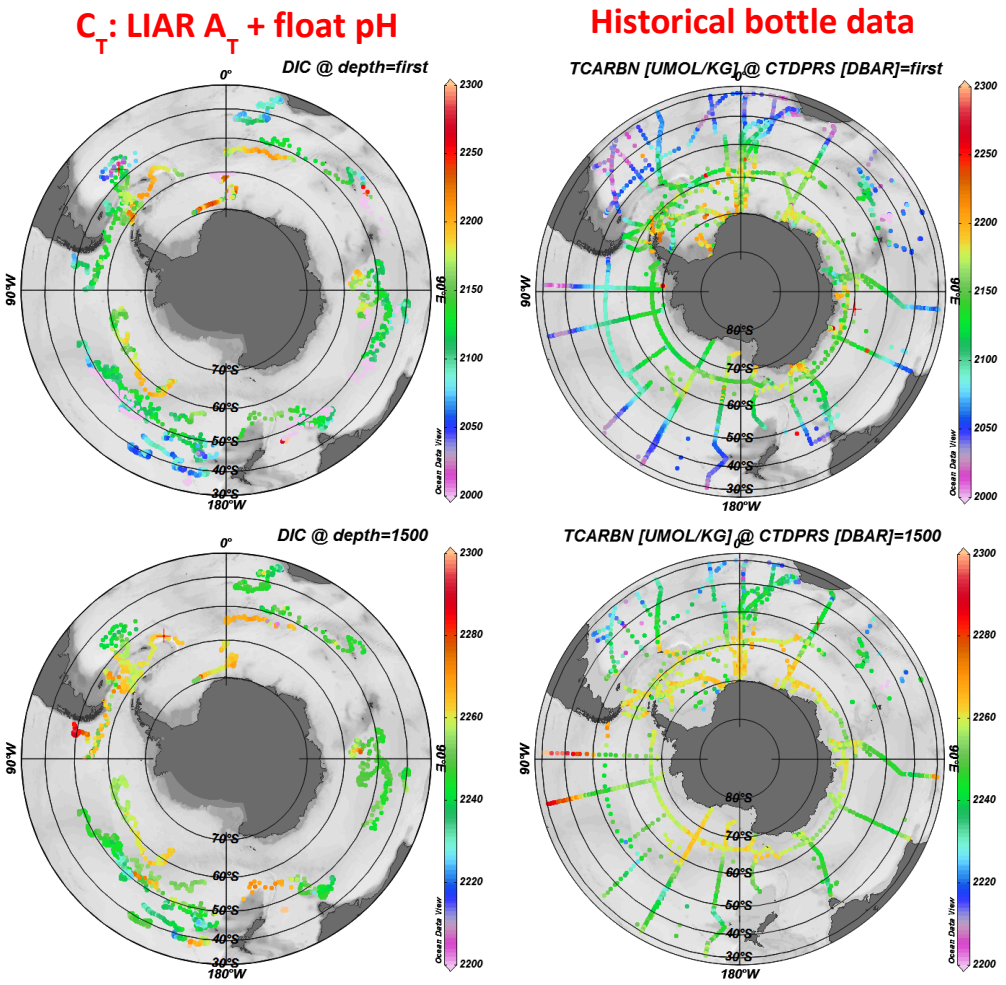

Figure 4.3 C_T computed from measured pH data from profiling floats and A_T estimated from the LIAR algorithm at the surface (top left) and at 1500 m (bottom left) compared to historical bottle data at the surface (top right) and at 1500 m (bottom right). There is qualitative good agreement between the algorithm and bottle data.

Table 4.1. Mean surface and deep (1500 m) Ψ computed using the three A_T algorithms and as reported by *Smith et al.*, [2013] for the Southern Ocean.

	LIAR	CANYON	MLR	Smith
Surface (~5m)	0.7584 ±0.0389	0.7569 ±0.0362	0.7692 ±0.0300	0.77 ±0.009
Deep (1500m)	0.8263 ±0.0201	0.8259 ±0.0176	0.8240 ±0.0172	0.85 ±0.001

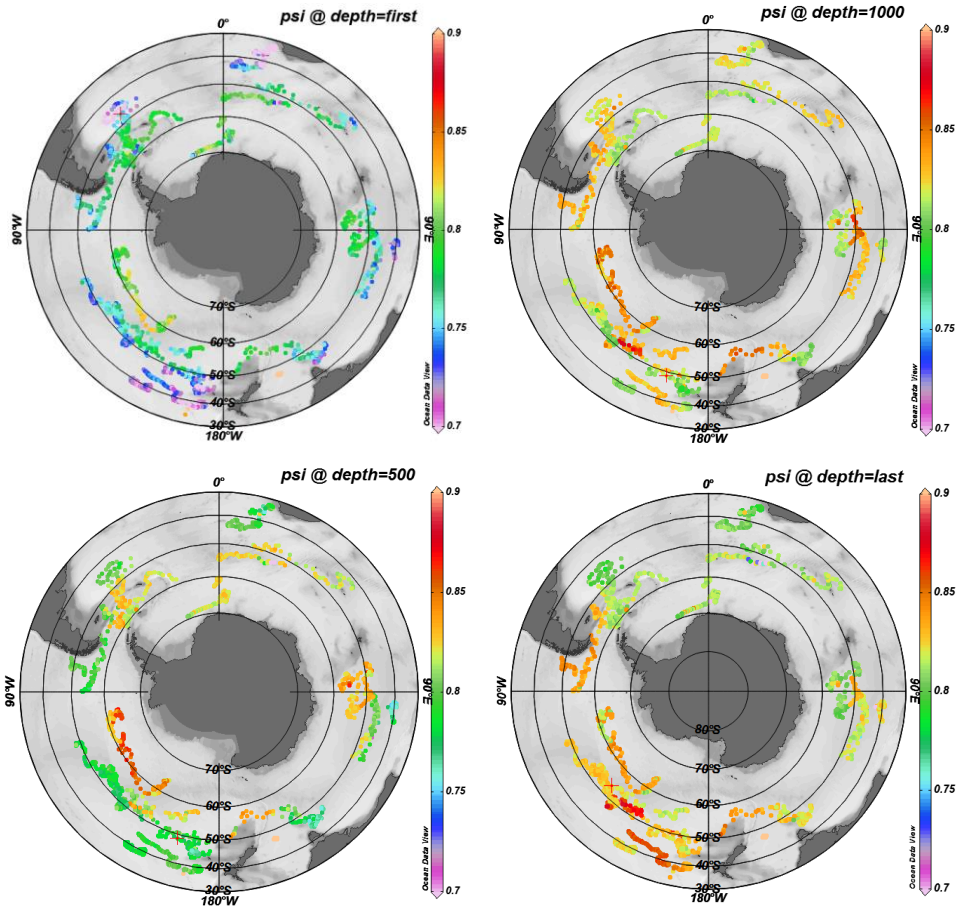

Figure 4.4. Ψ computed from profiling float data and the LIAR A_T algorithm at the surface (top left), 500 m (bottom left), 1000 m (top right), and 1500 m (bottom right). Ψ is lower in the surface and increases with depth as anticipated.

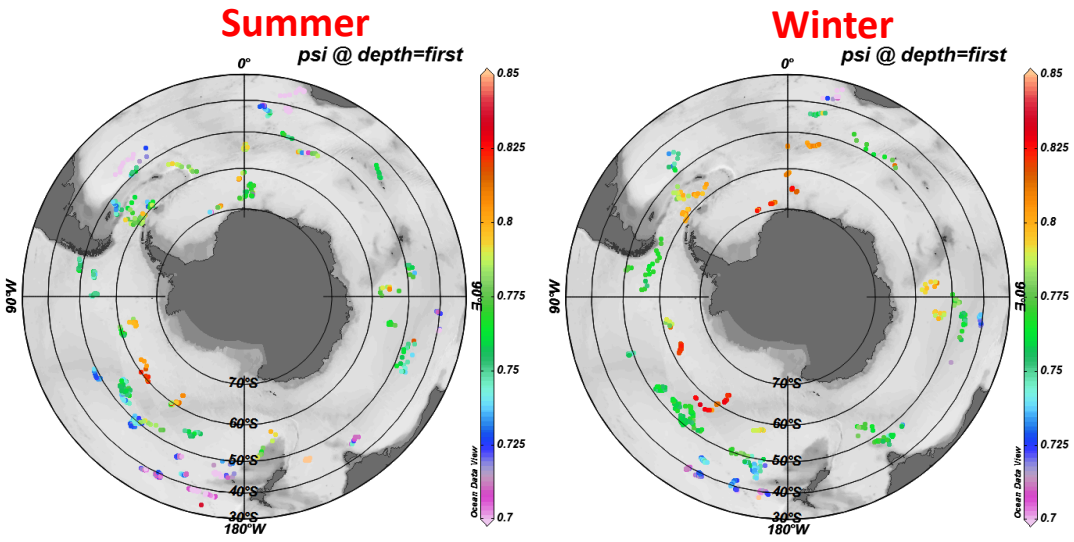

Figure 4.5. Surface Ψ calculated from profiling floats during the summer compared to the winter. There is a decrease in surface Ψ as anticipated due to warming of the surface ocean in the austral summer.

Profiles of Ψ calculated using the LIAR algorithm in the different frontal zones are shown in Figure 4.6. The surface and deep values of Ψ computed from all three A_T algorithms are listed in Table 4.2 for each of the frontal zones. There is very good agreement between the three A_T algorithms in all of the zones except for north of the STF where there weren't as many profiles used in the MLR calculation. Both the LIAR and CANYON algorithms agreed well in this zone however.

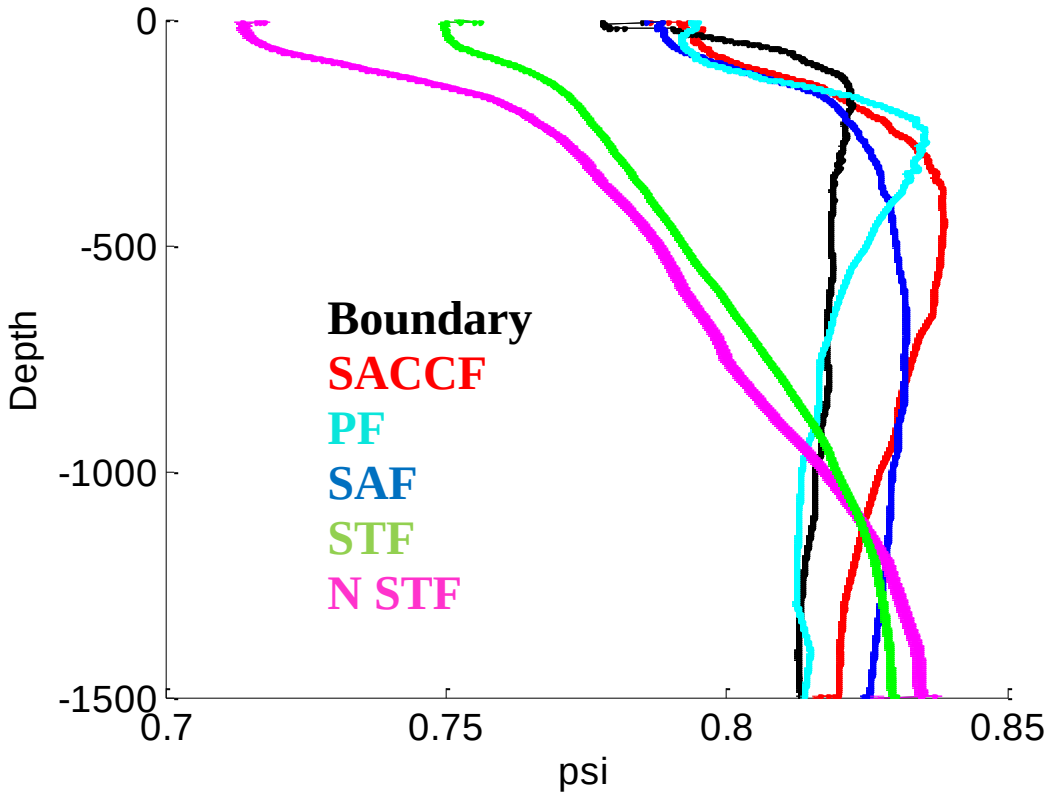

Figure 4.6. Vertical profiles of Ψ in the 6 frontal zones derived from the LIAR A_T algorithm.

Table 4.2. Surface (top 20 m) and deep (>=1500 m) Ψ computed from the three A_T algorithms and profiling float data for profiles divided into frontal zones.

LIAR	**Boundary**	**SACCF**	**PF**	**SAF**	**STF**	**N STF**
Surface (top 20 m)	0.7789 ±0.0274	0.7940 ±0.0087	0.7925 ±0.0186	0.7877 ±0.0210	0.7501 ±0.0240	0.7144 0.0162
Deep (>=1500m)	0.8117 ±0.0054	0.8112 ±0.0055	0.8107 ±0.0121	0.8204 ±0.0128	0.8277 ±0.0157	0.8281 ±0.0213
Profiles	181	52	157	353	949	434
CANYON	**Boundary**	**SACCF**	**PF**	**SAF**	**STF**	**N STF**
Surface (top 20 m)	0.7790 ±0.0085	0.7940 ±0.0085	0.7926 ±0.0180	0.7878 ±0.0212	0.7503 ±0.0239	0.7138 0.0158
Deep (>=1500m)	0.8118 ±0.0059	0.8113 ±0.0053	0.8109 ±0.0121	0.8202 ±0.0127	0.8277 ±0.0158	0.8281 ±0.0213
Profiles	184	50	154	346	930	429
MLR	**Boundary**	**SACCF**	**PF**	**SAF**	**STF**	**N STF**
Surface (top 20 m)	0.7789 ±0.0275	0.7940 ±0.0087	0.7931 ±0.0185	0.7877 ±0.0218	0.7519 ±0.0222	0.7241 0.0149
Deep (>=1500m)	0.8120 ±0.0061	0.8118 ±0.0053	0.8109 ±0.0129	0.8204 ±0.0137	0.8298 ±0.0152	0.8217 ±0.0032
Profiles	180	58	152	314	790	20

The box calculation of net CO_2 fluxes corresponding to the $CaCO_3$ pump is shown in Figure 4.7. The $CaCO_3$ production and sedimentation rates were estimated to be approximately 22×10^{12} mol PIC yr^{-1} and 1.6×10^{12} mol PIC yr^{-1} respectively. The rate of dissolution, calculated as the difference of production and sedimentation, was estimated to be 20.4×10^{12} mol PIC yr^{-1}. The net CO_2 gas flux was calculated to be $+0.2\times10^{12}$ mol yr^{-1} going into the ocean.

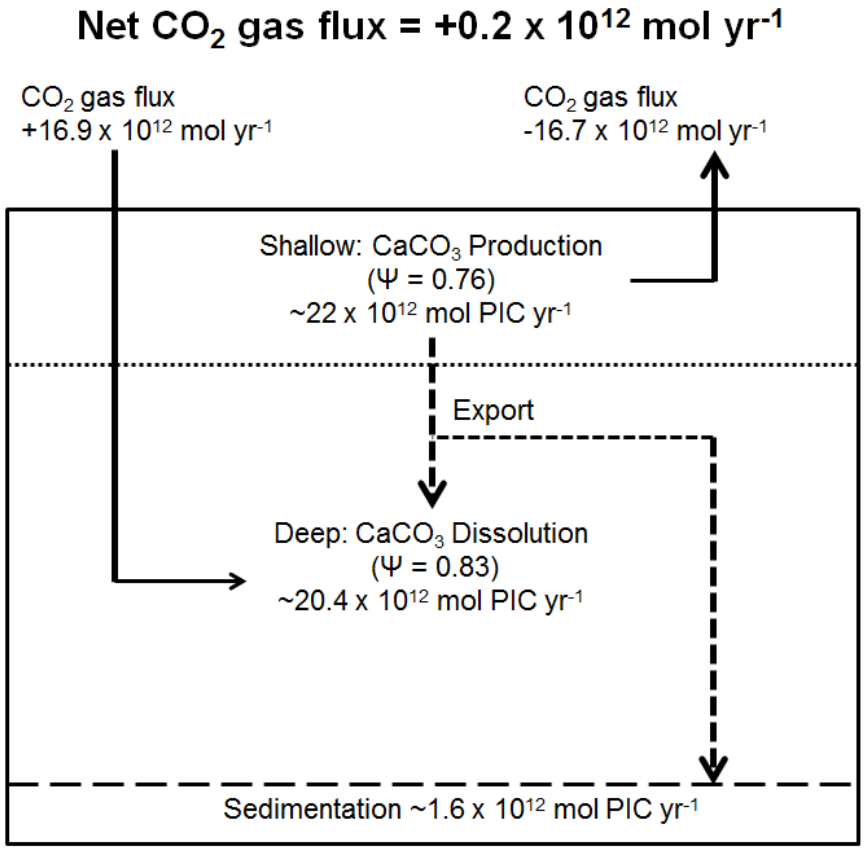

Figure 4.7. Box model showing the net CO_2 gas fluxes corresponding to the estimated production of $CaCO_3$ in the upper ocean and dissolution deeper in the water column. Due to the vertical variance in Ψ and burial of a portion of the PIC, there is a net influx of CO_2 into the ocean due to the $CaCO_3$ pump under current conditions.

The box calculation of net CO_2 fluxes corresponding to the $CaCO_3$ pump is shown in Figure 4.8. The $CaCO_3$ production, dissolution, sedimentation rates were approximated to be the same as in the contemporary configuration for simplification. The surface value for Ψ increased to 0.81 under elevated pCO_2 in the year 2100. The net CO_2 gas flux was calculated to be -0.9×10^{12} mol yr^{-1} going out of the ocean. Under elevated pCO_2, there is a transition from the pelagic $CaCO_3$ pump acting as a net sink of CO_2 to a net source of CO_2.

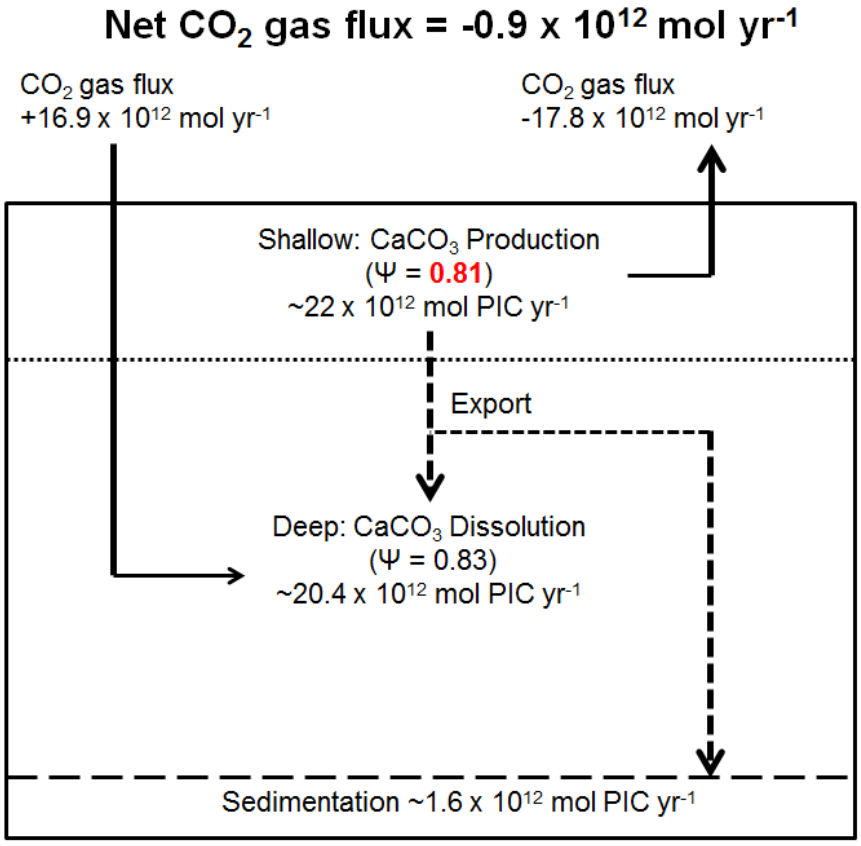

Figure 4.8. Under elevated atmospheric pCO_2, the upper ocean value of Ψ will increase. The resultant net flux due to the $CaCO_3$ pump becomes negative or a source of CO_2 to the atmosphere.

4 Discussion & Future Direction

It is significant to point out that 13,061 bottle samples corresponding to 751 hydrographic stations from 1990-2010 were used in the *Smith et al.* [2013] calculation of Ψ for the Southern Ocean compared to over 132,000 data points corresponding to 2126 profiles collected by BGC-Argo profiling floats from 2014 to present that were used in this study. It is important to consider the bias towards the austral summer in the historical data. There is a notable seasonal cycle in Ψ from profiling floats in the

surface ocean which is primarily due to the seasonal variation in surface temperature. There are different numbers of profiles computed for the different frontal zones for each of the A_T algorithms due to availability of required input data. The boundary for MLR is south of 45 ˚S so any profiles north of this latitude are not included in the A_T estimate resulting in less agreement with the other two algorithms in the N. STF region.

$CaCO_3$ production rates estimated from satellite data agreed fairly well with global estimates when considering the size fraction of the Southern Ocean [*Milliman*, 1993; *Smith et al.*, 2013; *Smith and Mackenzie*, 2016]. The mean global $CaCO_3$ production rate is 60×10^{12} mol PIC yr^{-1} and the GBC region accounts for 16% of the global ocean which would yield ~10×10^{12} mol PIC yr^{-1} if all production was homogenously distributed. Using the portion of suspended PIC based on satellite data (26%) as an estimate of the Southern Ocean's portion of the global rate would yield 16×10^{12} mol PIC yr^{-1}. A smaller regional study in the Drake Passage showed calcification rates up to 20 μmol C m^{-3} d^{-1}; however, this is representative of summertime productivity rather than representative of the annual rate over the whole Southern Ocean [*Charalampopoulou et al.*, 2016]. The satellite algorithm only takes into account coccolithophore production and there is evidence for abundance of other calcifiers in the Southern Ocean including pteropods which would suggest underestimation of production relying on satellite data alone [*Honjo et al.*, 2000]. However, a portion of the satellite signal could also be due to storm induced injection

of bubbles that enhance the reflectance in this region so it is difficult to constrain $CaCO_3$ production rates from satellite estimates alone [*Balch et al.*, 2011].

Ultimately the ratio of production:sedimentation:dissolution of $CaCO_3$ determines the magnitude and direction of CO_2 flux associated with the pelagic $CaCO_3$ pump. If more $CaCO_3$ is buried in the sediments, less CO_2 will be absorbed due to the dissolution of $CaCO_3$ at depth under greater Ψ relative to when it was produced because the size of the $CaCO_3$ reservoirs are unequal. Under elevated pCO_2 the surface Ψ approaches the same value as at depth and the pelagic $CaCO_3$ pump no longer functions as a net sink for CO_2 from the atmosphere and more similarly resembles the benthic $CaCO_3$ pump.

There are several estimates of future atmospheric CO_2 concentrations and predictions of the Southern Ocean becoming a weakening sink for atmospheric CO_2. Winds, freshening, changes in ice cover, and changes in biological activity are estimated to have a net weakening effect on atmospheric CO_2 uptake by the year 2100 [*Takahashi et al.*, 2012]. This simple box calculation doesn't take into account these other potential physical changes or changes in $CaCO_3$ production, dissolution, and sedimentation rates; however, this demonstrates the significance of the vertical variability of Ψ on the $CaCO_3$ pump and marine carbon cycle.

The next step is to use the Southern Ocean State Estimate [*Mazloff et al.*, 2010] with integrated biogeochemistry utilizing BLING (Biogeochemistry with Light, Iron, Nutrients, and Gases model) [*Galbraith et al.*, 2009] to assess the spatial variability of $CaCO_3$ production and dissolution under contemporary and elevated pCO_2 scenarios.

The state estimate can be used to quantify the relative magnitude and direction of change that the vertical variability in Ψ imparts on the $CaCO_3$ pump under varied atmospheric pCO_2. In addition, the relationship between the organic carbon and $CaCO_3$ reaction couplets can be compared in the Southern Ocean. In the contemporary global ocean there is a balance between these process couplets and SOSE can be used to demonstrate if this finding is valid for the model and how the relationship evolves under increasing atmospheric pCO_2.

5 Conclusions

Here the role of the pelagic $CaCO_3$ pump in the Southern Ocean was explored using profiling float data. The significant message here is that the carbonate system is complicated and it is important to understand that the ratio of CO_2 flux to $CaCO_3$ formation is not 1:1. This ratio of CO_2:$CaCO_3$ (i.e. evolution:production) denoted as Ψ, shows seasonal variability in the surface ocean as well as spatial variability when divided by frontal zones. The value of Ψ ranges from 0.76 in the surface to 0.83 at depth in the Southern Ocean. This vertical variability in Ψ has been demonstrated to serve as a net sink of CO_2 in the Southern Ocean due to greater uptake of CO_2 at depth during dissolution compared to CO_2 released during production in the surface water. Under elevated pCO_2, surface Ψ approaches the value at depth and the pelagic $CaCO_3$ pump becomes a net source of CO_2 to the atmosphere.

Acknowledgements & Data

Data were collected and made freely available by the Southern Ocean Carbon and Climate Observations and Modeling (SOCCOM) Project funded by the National Science Foundation, Division of Polar Programs (NSF PLR -1425989), supplemented by NASA, and by the International Argo Program and the NOAA programs that contribute to it. (http://www.argo.ucsd.edu, http://argo.jcommops.org). The Argo Program is part of the Global Ocean Observing System. SOCCOM float data can be found at http://www3.mbari.org/soccom/SOCCOM_Data_Archive/.

Chapter 4, in full, is currently being prepared for publication of the material. Ellen M. Briggs, Todd R. Martz, Stephen V. Smith. The dissertation author was the primary investigator and author of this material.

References

Balch, W. M., N. R. Bates, P. J. Lam, B. S. Twining, S. Z. Rosengard, B. C. Bowler, D. T. Drapeau, R. Garley, L. C. Lubelczyk, C. Mitchell, and S. Rauschenberg (2016), Factors regulating the Great Calcite Belt in the Southern Ocean and its biogeochemical significance, *Global Biogeochemical Cycles*, *30*(8), 1124-1144, doi:10.1002/2016GB005414.

Balch, W. M., D. Drapeau, B. Bowler, and E. Booth (2007), Prediction of pelagic calcification rates using satellite measurements, *Deep Sea Research Part II: Topical Studies in Oceanography*, *54*(5–7), 478-495, doi:http://doi.org/10.1016/j.dsr2.2006.12.006.

Balch, W. M., D. T. Drapeau, B. C. Bowler, E. Lyczskowski, E. S. Booth, and D. Alley (2011), The contribution of coccolithophores to the optical and inorganic carbon budgets during the Southern Ocean Gas Exchange Experiment: New evidence in support of the "Great Calcite Belt" hypothesis, *Journal of Geophysical Research: Oceans*, *116*(C4), 2156-2202, doi:10.1029/2011JC006941.

Bates, N.R., Y.M. Astor, M.J. Church, K. Currie, J.E. Dore, M. González-Dávila, L. Lorenzoni, F. Muller-Karger, J. Olafsson, and J.M. Santana-Casiano. 2014. A

time-series view of changing ocean chemistry due to ocean uptake of anthropogenic CO2 and ocean acidification. *Oceanography* 27(1):126–141, http://dx.doi.org/10.5670/oceanog.2014.16.

Broecker, W. S., T. Takahashi, H. J. Simpson, and T.-H. Peng (1979), Fate of Fossil Fuel Carbon Dioxide and the Global Carbon Budget, *Science*, *206*(4417), 409-418, doi:10.1126/science.206.4417.409.

Carter, B. R., N. L. Williams, A. R. Gray, and R. A. Feely (2016), Locally interpolated alkalinity regression for global alkalinity estimation, *Limnology and Oceanography: Methods*, *14*(4), 268-277, doi:10.1002/lom3.10087.

Charalampopoulou, Anastasia, Poulton, Alex J., Bakker, Dorothee C. E., Lucas, MIke I., Stinchcombe, Mark C. and Tyrrell, Toby (2016) *Environmental drivers of coccolithophore abundance and calcification across Drake Passage (Southern Ocean).* Biogeosciences, 13. pp. 5917-5935. ISSN 1726-4189

Egleston, E. S., C. L. Sabine, and F. M. M. Morel (2010), Revelle revisited: Buffer factors that quantify the response of ocean chemistry to changes in DIC and alkalinity, *Global Biogeochemical Cycles*, *24*(1), n/a-n/a, doi:10.1029/2008GB003407.

Frankignoulle, M., C. Canon, and J.-P. Gattuso (1994), Marine calcification as a source of carbon dioxide: Positive feedback of increasing atmospheric CO2, *Limnology and Oceanography*, *39*(2), 458-462, doi:10.4319/lo.1994.39.2.0458.

Freeman, N. M., and N. S. Lovenduski (2015), Decreased calcification in the Southern Ocean over the satellite record, *Geophysical Research Letters*, *42*(6), 1834-1840, doi:10.1002/2014GL062769.

Galbraith, E. D., A. Gnanadesikan, J. P. Dunne, and M. R. Hiscock (2009), Regional impacts of iron-light colimitation in a global biogeochemical model, *Biogeosciences Discuss.*, *6*(4), 7517-7564, doi:10.5194/bgd-6-7517-2009.

Honjo, S., R. Francois, S. Manganini, J. Dymond, and R. Collier (2000), Particle fluxes to the interior of the Southern Ocean in the Western Pacific sector along 170°W, *Deep Sea Research Part II: Topical Studies in Oceanography*, *47*(15–16), 3521-3548, doi:https://doi.org/10.1016/S0967-0645(00)00077-1.

Iglesias-Rodriguez, M. D., R. Armstrong, R. Feely, R. Hood, J. Kleypas, J. D. Milliman, C. Sabine, and J. Sarmiento (2002), Progress made in study of ocean's calcium carbonate budget, *Eos, Transactions American Geophysical Union*, *83*(34), 365-375, doi:10.1029/2002EO000267.

Marshall, J., and K. Speer (2012), Closure of the meridional overturning circulation through Southern Ocean upwelling, *Nature Geoscience*, *5*(3), 171-180, doi:10.1038/ngeo1391.

Mazloff, M. R., P. Heimbach, and C. Wunsch (2010), An Eddy-Permitting Southern Ocean State Estimate, *Journal of Physical Oceanography*, *40*(5), 880-899, doi:10.1175/2009jpo4236.1.

Mikaloff Fletcher, S. E., N. Gruber, A. R. Jacobson, S. C. Doney, S. Dutkiewicz, M. Gerber, M. Follows, F. Joos, K. Lindsay, and D. Menemenlis (2006), Inverse estimates of anthropogenic CO2 uptake, transport, and storage by the ocean, *Global Biogeochemical Cycles*, *20*(2), doi:10.1029/2005GB002530.

Milliman, J. D. (1993), Production and accumulation of calcium carbonate in the ocean: Budget of a nonsteady state, *Global Biogeochemical Cycles*, *7*(4), 927-957, doi:10.1029/93GB02524.

Morrison, A., Frolicher, T. & Sarmiento, J. (2015), Upwelling in the Southern Ocean. *Phys. Today* 68, 27–29.

Orr, J. C., V. J. Fabry, O. Aumont, L. Bopp, S. C. Doney, R. A. Feely, A. Gnanadesikan, N. Gruber, A. Ishida, F. Joos, R. M. Key, K. Lindsay, E. Maier-Reimer, R. Matear, P. Monfray, A. Mouchet, R. G. Najjar, G.-K. Plattner, K. B. Rodgers, C. L. Sabine, J. L. Sarmiento, R. Schlitzer, R. D. Slater, I. J. Totterdell, M.-F. Weirig, Y. Yamanaka, and A. Yool (2005), Anthropogenic ocean acidification over the twenty-first century and its impact on calcifying organisms, *Nature*, *437*(7059), 681-686, doi:http://www.nature.com/nature/journal/v437/n7059/suppinfo/nature04095_S1.html.

Orsi, A. H., T. Whitworth Iii, and W. D. Nowlin Jr (1995), On the meridional extent and fronts of the Antarctic Circumpolar Current, *Deep Sea Research Part I: Oceanographic Research Papers*, *42*(5), 641-673, doi:http://dx.doi.org/10.1016/0967-0637(95)00021-W.

Painter, S. C., A. J. Poulton, J. T. Allen, R. Pidcock, and W. M. Balch (2010), The COPAS'08 expedition to the Patagonian Shelf: Physical and environmental conditions during the 2008 coccolithophore bloom, *Continental Shelf Research*, *30*(18), 1907-1923, doi:https://doi.org/10.1016/j.csr.2010.08.013.

Revelle, R., and H. E. Suess (1957), Carbon Dioxide Exchange Between Atmosphere and Ocean and the Question of an Increase of Atmospheric CO2 during the Past Decades, *Tellus*, *9*(1), 18-27, doi:10.1111/j.2153-3490.1957.tb01849.x.

Rosengard, S. Z., P. J. Lam, W. M. Balch, M. E. Auro, S. Pike, D. Drapeau, and B. Bowler (2015), Carbon export and transfer to depth across the Southern Ocean Great Calcite Belt, *Biogeosciences*, *12*(13), 3953-3971, doi:10.5194/bg-12-3953-2015.

Sauzède;, R., Claustre, H., Pasqueron de Fommervault, O., Bittig, H., Gattuso, J.-P., Legendre, L. and K. Johnson, Estimates of water-column nutrients concentration and carbonate system parameters in the global ocean: A novel approach based on neural networks. Frontiers in Marine Science-Ocean Observation, in revision

Smith, S. V., and J.-P. Gattuso (2011), Balancing the Oceanic Calcium Carbonate Cycle: Consequences of Variable Water Column Ψ, *Aquatic Geochemistry*, *17*(4), 327-337, doi:10.1007/s10498-010-9109-9.

Smith, S. V., A. f. t. S. o. Limnology, and Oceanography (2013), *Parsing the Oceanic Calcium Carbonate Cycle: A Net Atmospheric Carbon Dioxide Source Or a Sink?*, Association for the Sciences of Limnology and Oceanography.

Smith, S. V., and F. T. Mackenzie (2016), The Role of CaCO3 Reactions in the Contemporary Oceanic CO2 Cycle, *Aquatic Geochemistry*, *22*(2), 153-175, doi:10.1007/s10498-015-9282-y.

Sundquist, E. T., L. N. Plummer, and T. M. L. Wigley (1979), Carbon Dioxide in the Ocean Surface: The Homogeneous Buffer Factor, *Science*, *204*(4398), 1203-1205, doi:10.1126/science.204.4398.1203.

Takahashi, T., C. Sweeney, B. Hales, D.W. Chipman, T. Newberger, J.G. Goddard, R.A. Iannuzzi, and S.C. Sutherland. 2012. The changing carbon cycle in the Southern Ocean. Oceanography 25(3):26–37, http://dx.doi.org/10.5670/oceanog.2012.71.

Williams, N. L., L. W. Juranek, R. A. Feely, K. S. Johnson, J. L. Sarmiento, L. D. Talley, A. G. Dickson, A. R. Gray, R. Wanninkhof, J. L. Russell, S. C. Riser, and Y. Takeshita (2017), Calculating surface ocean pCO2 from biogeochemical Argo floats equipped with pH: An uncertainty analysis, *Global Biogeochemical Cycles*, 591-604, doi:10.1002/2016GB005541.